

Wei Yu

Modeling, Testing and Application of  
Tuned Liquid Multi-Column Dampers  
for Floating Offshore Wind Turbines

for Floating Offshore Wind Turbines  
Tuned Liquid Multi-Column Dampers  
Modeling, Testing and Application of





# Modeling, Testing and Application of Tuned Liquid Multi-Column Dampers for Floating Offshore Wind Turbines

A thesis accepted by the Faculty of Aerospace Engineering and Geodesy of the  
University of Stuttgart in partial fulfillment of the requirements for the degree of  
Doctor of Engineering Sciences (Dr.-Ing.)

by

Wei Yu

born in Zhejiang, China

Main referee: Prof. Dr. Po Wen Cheng

Co-referees: Prof. Dr. Matthew Lackner

Date of defense: 15.09.2023

Stuttgart Wind Energy at the Institute of Aircraft Design  
University of Stuttgart  
2024



# Acknowledgments

I extend my heartfelt gratitude to the following individuals and entities whose support and inspiration have been essential in my academic journey:

My deepest appreciation goes to the entire SWE, where I have found continuous support and inspiration. Specifically, sincere thanks to Prof. Po Wen Cheng for providing me with invaluable opportunities and fostering an environment to grow. I am also indebted to the incredible "floating wind office", where I have worked with Frank Lemmer, Kolja Müller, Ricardo Faerron Guzmán, Shengtao Zhou, Umut Özinan over the past six years. People come and go, but the spirit and passion for floating wind, the collaboration and support always remain.

The wind research community has been an incredible source of support, and a role model of equality and diversity. As a female Chinese researcher - a true minority within the community - I have found immense kindness and encouragement. My heartfelt thanks to everyone who has engaged with me and offered warmth and support in projects, at conferences and meetings. Special thanks to Prof. Matthew Lackner for his invaluable guidance during the final stages.

I am deeply grateful to Prof. Liang Zhang, my fluid dynamics professor during my undergraduate studies. His encouragement for students to explore the world inspired me to pursue further studies in Germany. I'm also grateful for the accessibility of affordable education in Germany, which has greatly contributed to my academic growth and achievements. The educational equality, made possible by the German taxpayer and government, has a profound impact on young people like me.

Lastly, my heartfelt appreciation extends to my family. I have learned the magic of perseverance and resilience from my parents, always guiding me through moments of fragility and reminding me to never give up. And to my husband, Steven Weidgang, whose invaluable support, partnership, and friendship have been an anchor throughout this journey.



# Contents

<b>Abbreviations</b>	<b>ix</b>
<b>List of Symbols</b>	<b>xi</b>
<b>Abstract</b>	<b>xv</b>
<b>Kurzfassung</b>	<b>xvii</b>
<b>1 Introduction</b>	<b>1</b>
1.1 Motivation . . . . .	1
1.2 Objective . . . . .	2
1.3 Structure of the Thesis . . . . .	3
1.4 Notation . . . . .	3
<b>2 Background and State-of-the-Art</b>	<b>5</b>
2.1 Mathematical Formalisms of Mechanics . . . . .	5
2.1.1 General description . . . . .	5
2.1.2 Newton-Euler equations . . . . .	6
2.1.3 Lagrangian mechanics . . . . .	7
2.2 Modeling Techniques of Floating Offshore Wind Turbines . . . . .	8
2.2.1 Structural dynamics . . . . .	8
2.2.2 Aerodynamics . . . . .	10
2.2.3 Hydrodynamics . . . . .	12
2.2.4 Engineering tools . . . . .	13
2.3 Research on Structural Damper . . . . .	15
2.4 Different Control Approaches . . . . .	17
2.4.1 The non-minimum phase behavior . . . . .	17
2.4.2 Control approaches . . . . .	18
2.5 Control Co-Design . . . . .	20
2.6 Reference Models . . . . .	21
<b>3 Numerical Tool: Modelling, Coupling and Verification</b>	<b>25</b>
3.1 Reference Coordinates and Transformation . . . . .	25
3.2 Simplified Low Order FOWT Model . . . . .	27
3.3 Two-column Tuned Liquid Damper Model . . . . .	30

3.4	Tuned Liquid Multi-Column Damper Model . . . . .	34
3.4.1	Coordinates and notation . . . . .	35
3.4.2	Kinematics . . . . .	38
3.4.3	Potential and kinetic energy . . . . .	39
3.4.4	Non-conservative forces . . . . .	43
3.4.5	Equation of motion . . . . .	45
3.5	Equations of Motion of a TLMCD with Uniform Cross Sections . . . . .	50
3.5.1	Simplified expression . . . . .	50
3.5.2	Linearization . . . . .	51
3.6	Coupling with FOWT Numerical Model . . . . .	53
3.6.1	Explicit coupling . . . . .	54
3.6.2	Implicit coupling . . . . .	56
3.6.3	Comparison between different models . . . . .	58
3.6.4	Code-to-code verification . . . . .	59
<b>4</b>	<b>Experimental Validation</b>	<b>69</b>
4.1	Calibration of the TLMCD Stand-alone Model . . . . .	69
4.1.1	Laboratory setup . . . . .	69
4.1.2	Free decay test . . . . .	71
4.1.3	Forced harmonic oscillation . . . . .	74
4.2	Full System Wave Tank Test . . . . .	76
4.2.1	The physical model, sensors and test matrix . . . . .	77
4.2.2	System identification . . . . .	80
4.2.3	Wave-only load cases . . . . .	84
4.2.4	Irregular Wave and turbulent wind dynamic response . . . . .	87
<b>5</b>	<b>Synergism between the TLMCD and the Blade Pitch Controller</b>	<b>95</b>
5.1	Engineering Design Solutions . . . . .	96
5.2	Quantification of Design Criteria . . . . .	97
5.2.1	Closed loop SISO control system . . . . .	97
5.2.2	Quantification of stability . . . . .	98
5.2.3	Quantification of control performance . . . . .	100
5.3	Control Design Procedure . . . . .	105
5.4	Evaluation of the Control Design Method . . . . .	106
5.4.1	System Parameters and Load cases . . . . .	106
5.4.2	Brute force optimization of control design criteria . . . . .	108
5.4.3	The resulting control design . . . . .	112
5.4.4	Simulation results of design load cases . . . . .	114
5.5	Influence of the FOWT Substructure Design . . . . .	117



---

<b>6</b>	<b>TLMCD-aided Control Co-Design Optimization</b>	<b>121</b>
6.1	Optimizer, Design Space and Cost Model . . . . .	121
6.1.1	Design space . . . . .	121
6.1.2	Cost model . . . . .	124
6.1.3	Constraints . . . . .	125
6.1.4	Multi-objective optimizer . . . . .	126
6.2	Workflow for Objective Evaluation . . . . .	128
6.2.1	Inputs preparation of the dynamic model . . . . .	129
6.2.2	Model linearization and controller design . . . . .	130
6.2.3	Coupled design load case simulation and cost evaluation . . .	130
6.3	Optimization Result . . . . .	130
6.3.1	Initialization and convergence . . . . .	131
6.3.2	Optimized objective space . . . . .	132
6.3.3	Optimized decision space . . . . .	136
6.4	Comparison of Dynamic Responses . . . . .	139
<b>7</b>	<b>Conclusions and Outlook</b>	<b>143</b>
7.1	Main Contributions . . . . .	143
7.2	Findings and Lessons Learned . . . . .	144
7.3	Recommendations for Future Work . . . . .	146
<b>A</b>	<b>Damping coefficients from experiments</b>	<b>149</b>
<b>B</b>	<b>Influences of model fidelity on control design</b>	<b>151</b>
	<b>Bibliography</b>	<b>155</b>



# Abbreviations

2D	two-dimensional
3D	three-dimensional
3P	three-per-revolution
AHBS	Anti-Heeling Ballast System
BEM	Boundary Element Method
BEMT	Blade Element Momentum Theory
CCD	Control Co-Design
CFD	Computational Fluid Dynamics
CL	Closed Loop
CPC	Collective Pitch Controller
CROWN	Concrete Reduced-draft Offshore Wind turbine for iNdustry
DEL	Damage Equivalent Load
DLC	Design Load Case
DLL	Dynamic Link Library
DOF	Degree Of Freedom
DTU	Tichnical University of Denmark
EOG	Extreme Operating Gust
EQM	Equation of Motion
FAST	Fatigue, Aerodynamics, Structures, and Turbulence
FEM	Finite Element Method
FFT	Fast Fourier Transform
FOWT	Floating Offshore Wind Turbine
FVW	Free Vortex Wake
GDW	Generalized Dynamic Wake
IEC	International Electrotechnical Commission
IHC	Environmental Hydraulics Institute of Cantabria

LC	Load Case
LCOE	Levelized Cost Of Electricity
LTI	Linear Time-Invariant
MBS	Multibody System
MDAO	Multidisciplinary Design Optimizatio
MDR	Mutual Domination Rate
MIMO	Multiple-Input Multiple-Output
MPC	Model Predictive Controller
NREL	National Renewable Energy Laboratory
NSGA	Non-dominated Sorting Genetic Algorithm
ODE	Ordinary Differential Equation
OL	Open Loop
PF	Potential Flow
PI	Proportional-Integral
PSD	Power Spectral Density
RAO	Response Amplitude Operator
RDS	Reduced Draft Spar
RHPZ	Right-Half-Plane Zero
RMSE	Root Mean Square Error
RNA	Rotor Nacelle Assembly
SISO	Single-Input Single-Output
SLOW	Simplified Low Order Wind turbine
STD	Standard Deviation
SWE	Stuttgart Wind Energy
SWL	Sea Water Level
TLCD	Tuned Liquid Column Damper
TLMCD	Tuned Liquid Multi-Column Damper
TMD	Tuned Mass Damper
TSR	Tip Speed Ratio

# List of Symbols

## Greek letters

$\alpha_i$	rotation angle of $i^{\text{th}}$ element of the TLMCD
$\boldsymbol{\alpha}_i$	angular acceleration of a rigid body $i$ , $\boldsymbol{\alpha}_i \in \mathbb{R}^{3 \times 1}$
$\eta$	head loss coefficient of the TLMCD
$\gamma$	cross sectional area ratio of the TLMCD, $\gamma = \frac{A_v}{A_h}$
$\omega$	angular velocity of wind turbine
$\boldsymbol{\omega}^b$	angular velocity of a rigid body in body-fixed frame, $\boldsymbol{\omega}^b \in \mathbb{R}^{3 \times 1}$
$\beta_p$	platform pitch angle
$\boldsymbol{\omega}_p$	platform angular velocity in the body frame, $\boldsymbol{\omega}_p \in \mathbb{R}^{3 \times 1}$
$\sigma_i$	curvilinear abscissa along the $i^{\text{th}}$ streamline of the TLMCD
$\boldsymbol{\tau}$	external forces exerted on the FOWT, $\boldsymbol{\tau} \in \mathbb{R}^{f \times 1}$
$\tau_c$	the time constant of the closed loop control system of the wind turbine
$\zeta$	damping ratio of a second order system
$\boldsymbol{\Theta}$	Euler angle of a rigid body, $\boldsymbol{\Theta} = [\varphi, \beta, \psi]^T \in \mathbb{R}^{3 \times 1}$
$\boldsymbol{\Theta}_p$	Euler angle of the platform, $\boldsymbol{\Theta}_p = [\varphi_p, \beta_p, \psi_p]^T \in \mathbb{R}^{3 \times 1}$

## Roman letters

$\mathbf{a}_i$	linear acceleration of a body $i$ , $\mathbf{a}_i \in \mathbb{R}^{3 \times 1}$
$A(\sigma_i)$	cross sectional area of the TLMCD, which is a function of $\sigma_i$
$A_h$	cross sectional area of the horizontal duct of the TLMCD
$A_v$	cross sectional area of the vertical column of the TLMCD
$f$	number of DOFs of the MBS
$\mathbf{G}$	transfer matrix relating the time derivative of the Euler angle to the body angular velocity $\boldsymbol{\omega} = \mathbf{G}\dot{\boldsymbol{\Theta}}$ , $\mathbf{G} \in \mathbb{R}^3$
$\mathbf{H}$	matrix transferring the forces defined at the origin of the body frame to an arbitrary point, $\mathbf{H} \in \mathbb{R}^6$
$H_s$	significant wave height
$k_i$	integral gain of the turbine blade pitch PI controller
$\mathbf{K}_{\text{ns}}$	vector of restoring forces exerted on the platform due to the existence of TLMCD, $\mathbf{K}_{\text{ns}} \in \mathbb{R}^{6 \times 1}$
$\mathbf{K}_{\text{ns},l}$	additional stiffness matrix of the equations of motion for the platform due to the existence of TLMCD, $\mathbf{K}_{\text{ns},l} \in \mathbb{R}^{6 \times (6+nc)}$

$s$	Laplace variable, $s = j\omega$
$k_p$	proportional gain of the turbine blade pitch PI controller
$\mathbf{K}_t$	vector of restoring forces exerted on the TLMCD, $\mathbf{K}_t \in \mathbb{R}^{nc \times 1}$
$\mathbf{K}_{t,l}$	stiffness matrix of the equations of motion for the TLMCD, $\mathbf{K}_{t,l} \in \mathbb{R}^{nc \times (6+nc)}$
$\mathcal{L}$	the Lagrangian of the TLMCD system which is moving together with the FOWT
$m_t$	fluid mass of the TLMCD
$\mathbf{M}$	global mass matrix of the equations of motion for the FOWT, $\mathbf{M} \in \mathbb{R}^f$
$\mathbf{M}_{NS}$	mass matrix of the equations of motion for the TLMCD, $\mathbf{M}_{ns} \in \mathbb{R}^{6+nc}$
$M_{pt}$	step response peak value of a closed loop control system
$\mathbf{M}_q$	mass matrix of the TLMCD, $\mathbf{M}_q \in \mathbb{R}^{nc}$
$\mathbf{M}_s$	mass matrix of the equations of motion for the floating substructure with five DOFs, $\mathbf{M} \in \mathbb{R}^5$
$M_s$	sensitivity margin of an open loop transfer function
$\mathbf{M}_{vq}$	mass matrix representing the coupling between the FOWT translational motion and the TLMCD motion, $\mathbf{M}_{vq} \in \mathbb{R}^{3 \times nc}$
$\mathbf{M}_{\omega q}$	mass matrix representing the coupling between the FOWT rotational motion and the TLMCD motion, $\mathbf{M}_{\omega q} \in \mathbb{R}^{3 \times nc}$
$N$	number of vertical columns of the TLMCD
$nc$	number of DOFs of the TLMCD
$\mathbf{P}$	transfer matrix relating the time derivative of the initial coordinates to the body velocities, $\mathbf{P} \in \mathbb{R}^{6+nc}$
$\mathbf{Q}$	generalized non-conservative forces exerted on the TLMCD, $\mathbf{Q} \in \mathbb{R}^{nc \times 1}$
$\mathbf{q}$	generalized coordinates of a multibody system
$\mathbf{q}_s$	generalized coordinates of a floating platform with constrained degrees of freedom
$\mathbf{q}_w$	generalized coordinates of a floating platform with TLMCD
$\mathbf{R}$	rotation matrix transferring a vector in the body frame to the initial frame by $\dot{\mathbf{x}} = \mathbf{R}\mathbf{v}^b$ , $\mathbf{R} \in \mathbb{R}^{3 \times 3}$
$\mathbf{r}^b$	cartesian coordinates of a point at $\sigma_i$ along the treamline in the body frame, $\mathbf{r}^b(\sigma_i) = [x^b(\sigma_i), 0, z^b(\sigma_i)]^\top \in \mathbb{R}^{3 \times 1}$
$\mathbf{R}_z$	rotation matrix about z-axis, $\mathbf{R}_z \in \mathbb{R}^3$
$\tilde{\mathbf{S}}(\cdot)$	cross product operator, $\tilde{\mathbf{S}}(\mathbf{x})\mathbf{y} \triangleq \mathbf{x} \times \mathbf{y}$ , if $\mathbf{x}, \mathbf{y} \in \mathbb{R}^{3 \times 1}$ , $\tilde{\mathbf{S}}(\cdot)^2 = -\tilde{\mathbf{S}}(\cdot)^\top \tilde{\mathbf{S}}(\cdot)$
$T$	total kinetic energy of the TLMCD system which is moving together with the FOWT

---

$T_i$	integral time constant of the turbine blade pitch PI controller
$T_p$	wave peak period
$T_r$	rise time of a closed loop control system
$T_s$	settling time of a closed loop control system
$\bar{u}$	mean wind speed
$V$	total potential energy of the TLMCD system which is moving together with the FOWT
$\mathbf{v}^b$	linear velocity of a rigid body in the body-fixed frame, $\mathbf{v}^b \in \mathbb{R}^{3 \times 1}$
$v_0$	rotor effective wind speed
$\mathbf{v}_{t,i}^b$	fluid velocity in an arbitrary position inside the TLMCD, which is a function of $\sigma_i$ , $\mathbf{v}_{t,i}^b(\sigma_i) \in \mathbb{R}^{3 \times 1}$
$\mathbf{v}_h$	fluid speeds in the horizontal ducts of the TLMCD, $\mathbf{v}_h \in \mathbb{R}^{N \times 1}$
$\mathcal{V}$	volume of fluid inside the TLMCD, an arbitrary small volume of fluid is written as $d\mathcal{V}$
$\mathbf{v}_p$	platform linear velocity described in the body frame, $\mathbf{v}_p \in \mathbb{R}^{3 \times 1}$
$w_i$	free surface position of the $i^{\text{th}}$ streamline
$\mathbf{w}$	generalize coordinates of the TLMCD, $\mathbf{w} = [w_1, w_2 \cdots w_{nc}] \in \mathbb{R}^{nc \times 1}$
$\mathbf{x}$	position of a rigid body's body-fixed frame in the Earth-fixed initial coordinate frame, $\mathbf{x} = [x, y, z]^T \in \mathbb{R}^{3 \times 1}$
$\mathbf{x}_p$	position of the FOWT's body-fixed frame in the Earth-fixed initial coordinate frame, $\mathbf{x} = [x_p, y_p, z_p]^T \in \mathbb{R}^{3 \times 1}$
$\mathbf{z}$	unit vector in the direction of z-axis of a Cartesian coordinate system, $\mathbf{z} = [0, 0, 1]^T$ , $\mathbf{z}^T = [0, 0, 1]$





# Abstract

In recent years, a growing number of floating offshore wind turbine (FOWT) prototypes have been demonstrated, increasing both the technology readiness level and market confidence. The future of the floating wind sector is looking increasingly promising. However, compared to bottom fixed wind turbines, FOWTs face additional challenges due to the complex environmental conditions including higher motions and structural loads induced by wind and waves. One of the research focuses is to reduce these motions and loads to enable FOWTs to compete with bottom-fixed wind turbines. The main objective of this thesis is to achieve this by implementing stabilization systems.

Due to limited space and different geometric and dynamic characteristics compared to ships, a Tuned Liquid Multi-Column Damper (TLMCD) is chosen. The first step is to develop a numerical tool capable of modeling the coupled TLMCD and FOWT system. For the TLMCD, an existing method based on Lagrangian mechanics is adapted to derive the equations of motion and to be integrated into the Simplified Low Order Wind Turbine (SLOW) model. Both implicit and explicit coupling methods are implemented, and their simulation results are compared. For ease of implementation and to increase the computational efficiency, a simplified formulation is derived for TLMCDs with uniform cross-sectional areas, which eliminates the need for numerical integration in the original method. The simplified equations can be easily incorporated into different numerical models for FOWTs, and the coupled model is linearized for controller design. In addition, the developed coupled model is verified by comparison with the engineering tool OpenFAST. A good agreement is found, particularly with regard to platform dynamics, although differences arise due to the simplified quasi-static rotor model and the mooring system.

Two model test campaigns are carried out to assess the performance of the developed numerical tool. The first campaign considers only the stand-alone TLMCD,

with free decay tests and forced harmonic oscillations performed to determine the natural frequencies and damping coefficients. The comparison between simulation and experiment shows the promising functionality of the TLMCD modeling, although the fluid mass needs to be calibrated. This observation is consistent with findings in other publications, where the calibration of the fluid mass varies with the geometrical properties of the TLMCD. In the second campaign, the TLMCD is integrated into a scaled 10 MW FOWT and tested in a wave tank. Various load cases are tested, simulated and compared. The model is shown to be capable of reproducing the dynamic behavior of the coupled system.

During the development process, it is found that the system performance depends on whether or not the blade pitch controller works in synergy with the TLMCD. The presence of the TLMCD changes the characteristics of the FOWT dynamic plant, in particular the negative aerodynamic damping is partially compensated by the TLMCD. Therefore, an automated control design method is developed to adapt the controller to the TLMCD stabilized system. This design procedure can easily adapt the controller for different TLMCD designs. The method is evaluated on two FOWTs, and the results demonstrate that a TLMCD, together with a suitable blade controller, can significantly dampen platform motion at above rated wind speeds, with up to 40% reduction in standard deviation. In addition, there is a remarkable reduction in the tower base bending moment. The stabilized system also contributes to the rotor speed, resulting in improved power quality as the generator torque remains constant.

Due to the strong coupling between the aerodynamics, hydrodynamics and the servo dynamics, the investigated subsystems, namely the TLMCD and the blade pitch controller, are closely linked to the platform design. To investigate whether installing a TLMCD could potentially reduce the size of the platform, a multi-objective control co-design optimization framework is employed. This allows the TLMCD, the controller, and the platform to be optimized simultaneously. By searching for the optimal design space, in which these subsystems achieve good synergy, a well-balanced trade-off between production cost and response performance can be achieved. The final result demonstrates a reduction of up to 20% in the displaced tonnage of the FOWT without adversely affecting the motion and load-related costs.

# Kurzfassung

In den letzten Jahren wurden immer mehr Prototypen von schwimmenden Offshore Windenergieanlagen (SOWEA) vorgestellt, was nicht nur den Technologie-Reifegrad sondern auch die Marktakzeptanz erhöht. Aufgrund der komplexen Umweltbedingungen, sind sie im Vergleich zu am Boden verankerten Windenergieanlagen mit zusätzlichen Herausforderungen konfrontiert. Insbesondere verursachen Wind und Wellen höhere Bewegungen und strukturelle Belastungen. Damit schwimmende Windenergieanlagen mit am Boden verankerten Anlagen konkurrieren können, müssen die Bewegungen und Lasten reduziert werden. Das Ziel der Dissertation ist die Reduzierung der Bewegungen und Lasten durch die Anwendung eines U-Tank Stabilisierungssystems aus der Schiffstechnik.

Ein herkömmlicher Flüssigkeitsdämpfer kann in den meisten Fällen nur einen Freiheitsgrad dämpfen, was für die SOWEA nicht geeignet ist. Darüber hinaus ist der Einbau solcher Dämpfer in eine SOWEA aus Platzgründen schwierig. Aus diesen Gründen wird ein Tuned Liquid Multi-Column Damper (TLMCD) ausgewählt. Zunächst wird ein numerisches Tool entwickelt, welches das gekoppelte System aus TLMCD und SOWEA modellieren kann. Für den TLMCD wird eine bestehende Methode zur Ableitung der Bewegungsgleichungen, basierend auf der Lagrange-Mechanik, angepasst und implementiert. Die Bewegungsgleichungen werden mit dem bestehenden numerischen Tool Simplified Low Order Wind Turbine (SLOW) gekoppelt. Um die Implementierung zu vereinfachen und die Recheneffizienz zu erhöhen, wird eine wesentlich einfachere Formulierung für TLMCDs mit gleichmäßigen Querschnitten abgeleitet, die leicht in verschiedene Simulationstools für SOWEAs integriert werden kann. Zusätzlich wird das gekoppelte Modell linearisiert, was für den Reglerentwurf essentiell ist. Das entwickelte gekoppelte Modell wird durch einen Code-zu-Code Vergleich mit dem Engineering Tool OpenFAST verifiziert. Es zeigt sich eine gute Übereinstimmung, insbesondere in Bezug auf die Plattformdynamik.

Die Hauptunterschiede ergeben sich aus dem vereinfachten quasistatischen Rotormodell und dem Verankerungssystem.

Um die Leistungsfähigkeit des entwickelten numerischen Tool zu evaluieren, werden zwei Testkampagnen durchgeführt. In der ersten Kampagne wird der TLMCD als Stand-Alone System betrachtet. Zur Bestimmung der Eigenfrequenzen und der Dämpfungskoeffizienten des TLMCD, werden sogenannte Ausschwingversuche und Versuche mit harmonischen Schwingungen durchgeführt. In der zweiten Kampagne wird der TLMCD zusammen mit einer skalierten 10MW SOWEA im Wellentank getestet. Tests in verschiedenen Lastfällen werden durchgeführt. Der Vergleich zwischen Simulation und Experiment zeigt, dass das numerische Tool in der Lage ist, das dynamische Verhalten des gekoppelten Systems abzubilden.

Die Simulationen zeigen, dass das Systemverhalten davon abhängt ist, ob der Pitchwinkel-Regler der Rotorblätter mit dem TLMCD zusammenwirkt. Die Existenz des TLMCD verändert die dynamischen Eigenschaften der SOWEA, insbesondere wird die sogenannte negative aerodynamische Dämpfung durch den TLMCD teilweise kompensiert. Daher wird ein automatisierter Regelungsentwurf entwickelt, der in der Lage ist, den Pitchwinkel-Regler an das TLMCD-stabilisierte System anzupassen. Das Entwurfsverfahren wird an zwei SOWEAs getestet. Die Ergebnisse zeigen, dass ein TLMCD, zusammen mit einem geeigneten Pitchwinkel-Regler in der Lage ist, die Bewegung der Plattform bei höheren Windgeschwindigkeiten deutlich zu dämpfen, bis zu 40 % der Standardabweichung. Auch das Biegemoment des Turmfußes wird deutlich reduziert. Darüber hinaus trägt der TLMCD zur Stabilisierung der Rotordrehzahl und damit zu einer besseren Stromproduktion bei.

Aufgrund der starken Kopplung zwischen der Aerodynamik und Hydrodynamik, sind die betroffenen SOWEA-Subsysteme, nämlich der TLMCD und der Pitchwinkel-Regler, eng mit dem Plattformdesign verbunden. Daher wird im letzten Schritt ein Multi-Objective Control Co-Design Optimierungsprozess entwickelt. Dieser ermöglicht die simultane Optimierung des TLMCD, des Reglers und der Plattform. Durch die Suche nach dem optimalen Design Space, in dem die oben genannten Subsysteme gute Synergieeffekte erzielen, kann ein ausgewogenes Verhältnis zwischen Produktionskosten und Leistungsverhalten erreicht werden kann. Die Fallstudie zeigt eine Reduktion der Wasserverdrängung der SOWEA um bis zu 20 % ohne Verschlechterung des dynamischen Verhaltens.

# 1 Introduction

This chapter provides an overview of the background, main motivation, and objectives of this thesis. It also summarizes briefly the relevant state-of-the-art technologies. To improve readability, the overall structure of the thesis is introduced in Section 1.3, while the notation rules used throughout the thesis are described in Section 1.4.

## 1.1 Motivation

The energy sector is facing increasing environmental challenges and geopolitical risks, making renewable energy resources, such as wind energy, more attractive. Over the past few decades, wind energy has experienced remarkable development, and the future of the wind industry looks increasingly rosy. However, limitations such as the lack of wind resources, the need for large installation areas, public acceptance, and logistical problems have hindered the future growth of the onshore wind. This has encouraged the market to move towards offshore wind solutions. Among these solutions, Floating Offshore Wind Turbines (FOWTs) offer the advantage of access to deeper water where wind is typically stronger and more stable. The commissioning of the world's first full-scale FOWT, the 2.3 MW Hywind, has increased both the technical readiness level and market confidence. Since then, various prototype projects have been deployed, making FOWT technology even more promising.

Despite their advantages, FOWTs face additional challenges compared to bottom fixed wind turbines due to the complex environmental conditions. On the one hand, the wave load, one of the dominant load sources, leads to additional responses, including at the tower base [1]. On the other hand, the flexible support structure can lead to instability due to coupling with the wind turbine controller and aerodynam-

ics. These factors lead designers to choose more conservative substructure designs, which are relatively large and heavy. As a result, the higher LCOE compared to onshore and bottom fixed offshore wind turbines slows down the industrialization and market acceptance of FOWTs. Therefore, minimizing the LCOE to enable FOWTs to compete with onshore and bottom fixed offshore wind turbines is a key challenge.

## 1.2 Objective

As discussed previously, the primary goal of most research related to FOWT is to reduce the Levelized Cost Of Electricity (LCOE), which involves a variety of factors, both economic and technical. From a system design perspective, reducing the motions and loads of FOWTs is one of the key aspects. There are many techniques to achieve this, such as developing innovative floating substructure concepts, implementing structural dampers, employing advanced control systems and so on. The main focus of this thesis is to learn from the existing stabilizer system of naval architectures and adapt them to FOWTs. The scope is limited to barge or semi-submersible floating platforms. To achieve this goal, the conventional Tuned Liquid Column Damper (TLCD) should be modified into Tuned Liquid Multi-Column Damper (TLMCD) by increasing the number of vertical columns. The developed TLMCD should be able to fit into the specific configurations of FOWTs. Furthermore, the overall system dynamic performance should be improved.

The main work of this thesis can be divided into two parts. The first part is to develop a numerical tool suitable for modeling such a TLMCD stabilized FOWT system. The developed tool should not only be able to capture the coupled dynamics between the TLMCD and the FOWT system, but also include the state-of-the-art aero-hydro-servo-elastic modeling capabilities. In addition, the model should be validated against experiments in order to achieve a certain level of accuracy.

The second part focuses on the application of TLMCDs to FOWTs. The specific requirements and constraints of FOWTs need to be considered, which differ significantly from those of marine applications. Since FOWTs are actively controlled systems, adding an additional damping device implies a modification of the plant dynamics. Therefore, the impact of this modification on the overall system performance should be investigated.

## 1.3 Structure of the Thesis

The thesis is structured as follows: Chapter 1 provides an overview of the challenges and motivation derived from the state-of-the-art research, and outlines the objectives based on the challenges. Chapter 2 reviews the related current research work. In Chapter 3, a numerical tool for the entire work is established, and its validation against experimental tests is presented in Chapter 4. Two different applications of TLMCDs to FOWTs are demonstrated in Chapters 5 and 6, which are focused on control and optimization, respectively. Finally, summary and outlook are presented in the last chapter.

## 1.4 Notation

The notations used in the numerical model for the FOWT, denoted by Simplified Low Order Wind turbine (SLOW), are mostly adopted from [2]. In addition, the notations used for the TLMCD modeling are inherited from [3]. However, minor adjustments have been made to resolve any conflicts. All variables are written in italic typeface, with vectors denoted by lower case letters, e.g.  $\mathbf{v}$ , and matrices written in italic upper case letters, e.g.  $\mathbf{M}$ .





## 2 Background and State-of-the-Art

This chapter introduces the research methodology used in the present work. A thorough review of the relevant publications is made, summarizing the relevant state-of-the-art technologies.

### 2.1 Mathematical Formalisms of Mechanics

Isaac Newton formulated Newton's laws of motion in 1687. About sixty years later, Leonhard Euler extended upon these laws for rigid bodies with two additional laws, known as Euler's First and Second Axioms. Another forty years later, Joseph Louis Lagrange reformulated these laws by considering the whole system with scalar properties, i.e. kinetic energy and potential energy, rather than using vectorial quantities for the system. Thanks to these fundamental developments, which took over a century, the numerical tool in this work could be developed for practical application. This chapter provides a brief summary of these laws in a mathematical representation, which is helpful in understanding the derivation of the equations of motion.

#### 2.1.1 General description

Mathematical models of dynamic systems describe why and how bodies move when forces are applied to the system or generated within the system. One of the most popular application areas is in the robotics, for the purpose of modeling and control of these systems. Different methods can be used to derive the relationships between forces and motions, but their end results are always equivalent to each other, i.e. a description of the equations of motion formulated as

$$\mathbf{M}(\mathbf{q})\ddot{\mathbf{q}} + \mathbf{c}(\mathbf{q}, \dot{\mathbf{q}}) + \boldsymbol{\tau}_g(\mathbf{q}) = \boldsymbol{\tau} + \mathbf{J}_c(\mathbf{q})^\top \mathbf{F}_c, \quad (2.1)$$

where the components are detailed as follows:

$\mathbf{q} \in \mathbb{R}^{f \times 1}$	Generalized position vector with $f$ Degrees of Freedom (DOFs)
$\dot{\mathbf{q}} \in \mathbb{R}^{f \times 1}$	Generalized velocity vectors, time derivative of $\mathbf{q}$
$\ddot{\mathbf{q}} \in \mathbb{R}^{f \times 1}$	Generalized acceleration vectors, time derivative of $\dot{\mathbf{q}}$
$\mathbf{M}(\mathbf{q}) \in \mathbb{R}^{f \times f}$	Generalized inertia matrix
$\mathbf{c}(\mathbf{q}, \dot{\mathbf{q}}) \in \mathbb{R}^{f \times f}$	Coriolis and centrifugal forces
$\boldsymbol{\tau}_g(\mathbf{q}) \in \mathbb{R}^{f \times 1}$	Gravitational forces
$\boldsymbol{\tau} \in \mathbb{R}^{f \times 1}$	External generalized forces
$\mathbf{F}_c \in \mathbb{R}^{6 \times 1}$	External forces described in Cartesian coordinates
$\mathbf{J}_c(\mathbf{q}) \in \mathbb{R}^{6 \times f}$	Geometric Jacobian matrix for the external forces

These are the so-called equations of motion, which can be found in many robotics textbooks, such as [4]. For offshore structures, [5] has adapted the conventional differential equations and formulated the hydrostatic and hydrodynamic forces in such a way that they can be integrated into this vectorial representation. The most widely used methods for deriving these equations include the Newton-Euler method, the Lagrange method, or a hybrid form of both.

### 2.1.2 Newton-Euler equations

The Newton-Euler method describes the motions and forces explicitly in Cartesian coordinates. Essentially, it formulates the principles of conservation of linear and angular momentum mathematically through Euler's First and Second Axioms. For a moving rigid body, the change in linear and angular momentum depends on the applied net forces and moments, respectively. When neglecting the Earth's rotation, a fixed point on the Earth can be considered as an inertial frame. As a result, these conservation laws can be expressed as

$$\begin{aligned}\frac{{}^i d}{dt}(m\mathbf{v}_g) &= \mathbf{f}_g \\ \frac{{}^i d}{dt}(\mathbf{I}_g\boldsymbol{\omega}_b) &= \mathbf{l}_g,\end{aligned}\tag{2.2}$$

where  $\mathbf{f}_g$  and  $\mathbf{l}_g$  are the total resulting forces and moments acting on the center of gravity of the body.  $\boldsymbol{\omega}_b$  is the body angular velocity with respect to the initial frame, and  $\mathbf{v}_g$  is the linear velocity of the center of gravity with respect to the initial frame. The inertia  $\mathbf{I}_g$  is also described about the center of gravity.

The time derivative in the initial frame  $\frac{{}^i d}{dt}$  represents the change in linear or angular momentum. For a rigid body, they are defined as

$$\begin{aligned}\frac{{}^i d}{dt}(m\mathbf{v}_g) &= m(\dot{\mathbf{v}}_g + \boldsymbol{\omega}_b \times \mathbf{v}_g) \\ \frac{{}^i d}{dt}(\mathbf{I}_g\boldsymbol{\omega}_b) &= \mathbf{I}_g\dot{\boldsymbol{\omega}}_b + \boldsymbol{\omega}_b \times (\mathbf{I}_g\boldsymbol{\omega}_b),\end{aligned}\tag{2.3}$$

### 2.1.3 Lagrangian mechanics

Lagrangian mechanics, as a branch of analytical mechanics, is an alternative to the Newton-Euler equations for deriving the equations of motion of mechanical systems. There are several essential concepts that differ from the Newton-Euler method. First, instead of using a position and velocity vector for each body, vector  $\mathbf{q}$  describing the generalized coordinates is defined for all possible DOFs. A scalar quantity called Lagrangian  $\mathcal{L}$  is used, which mainly has the mathematical functionality. For a mechanical system, the Lagrangian  $\mathcal{L}$  is the difference between the total kinetic energy  $T$  and the total potential energy  $V$  of that system:

$$\mathcal{L} = T - V,\tag{2.4}$$

then the system kinetics are given by

$$\frac{d}{dt} \frac{\partial \mathcal{L}}{\partial \dot{\mathbf{q}}} - \frac{\partial \mathcal{L}}{\partial \mathbf{q}} = \boldsymbol{\tau},\tag{2.5}$$

where  $\boldsymbol{\tau}$  is the generalized non-conservative forces, representing the energy in and out of the system.

As can be seen, unlike the Newton-Euler method, where forces (both internal and external) acting on each body are explicitly taken into account, the Lagrange method eliminates all the internal action and reaction forces of the system from the resulting equations of motion. This can be advantageous for a complex system with multiple bodies and joints.

## 2.2 Modeling Techniques of Floating Offshore Wind Turbines

The dynamics of a FOWT are complex due to the multidisciplinary nature of the system and the various external excitations it is subject to, such as structural dynamics, aerodynamics, hydrodynamics, and servo dynamics. Depending on the modeling purpose, as well as the required level of accuracy and computational efficiency, different numerical techniques and software tools are available. Generally, the level of model fidelity can be classified into three categories: low, mid, and high fidelity, with each having its own specific modeling techniques and applications. However, there is no standard for the choice of numerical modeling tools used for all applications.

### 2.2.1 Structural dynamics

The modeling focuses of the structural components of a FOWT are diverse in many aspects, therefore, the physical details captured by the models are different from component to component. Most numerical tools adopt a Multibody System (MBS) approach to simulate the structural dynamics of the FOWT, covering the floating platform (floater), tower, and turbine components. The turbine is typically decomposed into blades, nacelle, generator, and drivetrain. The level of complexity of the MBS and the modeling approaches employed for each body depend on the required model fidelity for a certain application.

Most numerical tools assume that the floater of a FOWT is a rigid body. For low fidelity models used for overall geometric sizing, optimization, or controller design, modeling the floater as a rigid body with partially constrained DOFs is sufficient. For example, a low fidelity model for controller design might consider only the

surge, heave, and pitch DOFs of the floater. The reduced number of DOFs simplifies modal analysis, stability analysis, as well as control loop shaping. Mid fidelity models capture similar structural dynamics, but with an increased number of DOFs. When writing the equations of motion, some numerical tools, such as OpenFAST and SIMPACK, use the small-angle approach to transfer the time derivatives of the position and orientation of a rigid body into linear and angular velocities described in the body frame. This simplifies the final system equations of motion and increases computational efficiency. However, inaccuracies arise when large rotational motions, such as the yaw motion of the floater, are present. As the size of wind turbines increases, floaters become larger and more flexible, increasing the need for structural load analysis, particularly for some lightweight FOWTs that use highly flexible components. Modeling the floater as a rigid body becomes insufficient as the structural stresses and deformations are missing. A simple solution is to add the corresponding stresses during post-processing after the time domain simulation, allowing for the analysis of the stress of the structural components.

In contrast to the floater, which is usually modeled as a rigid body, the tower is typically modeled as a flexible body. The main approaches for tower structural modeling are the Finite Element Method (FEM) and modal decomposition methods. The modal decomposition method, such as the Craig-Bampton approach [6], simplifies the structural model by order reduction, decomposing the complex motion of the tower into a set of simpler, predefined deformation modes. The basic idea is to use FEM to compute the natural frequencies and mode shapes of the tower, and then to use these mode shapes to construct a reduced-order model that captures the essential dynamic behavior of the tower. In practice, the tower need to be discretized into small sections with sectional structural properties such as mass, stiffness etc. Based on that, the overall modal stiffness and damping can be calculated. Then the reduced order equations of motion of the tower can be written. The resulting model can be treated as a flexible MBS with certain constraints. On the other hand, FEM is a more detailed method that can provide local stresses and strains. Due to the special geometry of the tower, beam models are normally sufficient for stress analysis. To increase computational efficiency, linear frame FEM models can be used by neglecting nonlinearities such as large displacements, axial shortening due to bending, and cross-sectional transverse shear effects. The nonlinear effect of off-

shore substructures has been studied in [7]. The results show that the nonlinearities are approximately 4% at the tower top and 3% at the tower base, quantified in terms of the maximum differences in displacements and stresses with respect to a linear calculation.

As for the wind turbine, there are many options for the turbine structural modeling, depending on the intended use cases. For state space representation or frequency domain simulation, a simple approach is to model the rotor (including the nacelle) as a mass point or as a rigid body described by an inertia matrix. This approach is useful for control design, optimization, or large number of simulations. A more detailed model separates the rotor and the nacelle and represents the blades as flexible structures. To account for the elasticity of the blades, beam models or flexible MBSs are commonly used, the principles of which are similar to the tower modeling. These more detailed models are typically used for load analysis, as well as for blade design and optimization.

### 2.2.2 Aerodynamics

The Blade Element Momentum Theory (BEMT) is a widely used numerical approach for modeling the aerodynamics of FOWTs. This method divides the turbine blades into smaller elements and calculates the aerodynamic lift and drag forces on each blade element by combining the actuator disk theory with the blade element theory. The forces on each blade element are calculated iteratively for a given inflow condition, and the loading of the entire rotor is the sum of the forces over the blades. The fundamental principle of BEMT can be found in many textbooks, such as [8] or [9].

However, modeling the aerodynamics of FOWTs using BEMT poses special challenges. One of the important characteristics of the aerodynamics of FOWTs is the dynamic inflow effect, which arises due to the pitch and surge motions of the platform, causing additional relative wind velocity and leading to unsteady aerodynamics. This effect can result in overshoot and additional thrust loading on the rotor, which cannot be effectively captured by BEMT alone [10]. Moreover, the unsteady wake effect, which is also not considered by BEMT, is more pronounced in FOWTs than in onshore wind turbines. To address these challenges, more advanced aerody-

dynamic models, such as the free wake method, can be used to reproduce the periodic deformation of wake vortices, as well as the large differences in thrust loading and power production caused by the platform motion.

Therefore, in recent years, there has been increasing interest in using higher fidelity aerodynamic models for FOWTs, especially as rotor size and blade elastic deformation increase significantly, making it more important to accurately capture these aerodynamic effects. To model the highly turbulent flow around the blades and the resulting wake behind the rotor, a high fidelity Computational Fluid Dynamics (CFD) method is the most appropriate approach. Recent advances in computational resources have made it possible to perform such high fidelity simulations, providing valuable insights into the complex fluid flow and fluid-structure interactions that occur in the real world and aiding in the design of more reliable systems. However, the high computational cost required for CFD simulations has limited their use during the conceptual development of FOWTs, where a large number of simulations need to be conducted.

Given these challenges, one popular compromise between the high computational cost required CFD methods and the more simplified BEMT model with a lot of assumptions is the mid fidelity Free Vortex Wake (FVW) method, which models the unsteady aerodynamics of FOWTs using a finite volume method. This method takes into account the dynamic inflow effect and the unsteady wake effects, and can provide more accurate results compared to BEMT. The computational cost of FVW is higher than BEMT, but lower than CFD methods, making it a more practical option during the design phase. In addition to mid fidelity models, simpler engineering models, such as the Generalized Dynamic Wake (GDW) method [11], can be used. It takes into account the dynamic inflow effect and wake-induced unsteadiness by correcting the BEMT model, which is supposed to represent the physics of aerodynamics more realistically, i.e., the aerodynamic loading on a blade element and its impact on the wake.

Despite the need for more accurate numerical models, computationally efficient aerodynamic models are also necessary, mainly for control design and concept optimization. One simple approach is to consider the rotor as a rigid disk and characterize the aerodynamics using thrust and power coefficients as functions of the blade pitch angle and the Tip Speed Ratio (TSR), which can be implemented using lookup

tables. As a result, aerodynamic forces that depend only on the wind speed, blade pitch angle, and TSR can be linearized, which is suitable for modal analysis and control design. Such simplified models provide a quick and efficient way to evaluate different control strategies and assess their impact on FOWT performance.

### 2.2.3 Hydrodynamics

Modeling practices related to hydrodynamics have been developed and advanced within the oil and gas industry, and these methodologies have been widely adopted for modeling the hydrodynamics of FOWTs.

To model the wave induced excitation forces, the Potential Flow (PF) theory is a standard engineering approach. The submerged geometry of the floater is predefined according to the design draft in still water, which is assumed to be constant. The wet surface of the floater can then be meshed into surface panels. Depending on the wave kinematics, the local dynamic pressure exerted on each panel can be calculated and integrated over the entire surface, resulting in hydrodynamic forces and moments for the six DOFs. These forces vary with the angular frequencies of the incident waves, and thus are expressed by hydrodynamic coefficients in the frequency domain, which can be solved using panel codes such as Ansys AQWA or WAMIT. In addition to the wave excitation forces, the motion of the floater itself induces additional hydrodynamic loads, referred to as added mass and radiation damping. The diffraction effect appears when the size of the floater increases, which influences the propagation of the incident waves. These effects can all be solved by panel codes in the frequency domain. For time domain simulations, the hydrodynamic coefficients are pre-processed and transformed into the time domain.

In the early stages of FOWT research, wave excitation forces are mostly described as linear, i.e. only the first-order forces within the range of wave frequencies are considered [12] [13]. However, as more wave tank testing and prototype testing are conducted, it becomes clear that second-order wave forces should also be included in the analysis. These forces are outside of the frequency range of wave energy and are due to the sum and difference of the regular components of waves. For most FOWTs (except tension leg type), forces resulting from the difference-frequency of the wave components are most relevant, which are known as low-frequency wave drift forces



(consist of mean wave drift forces and slowly varying forces on top) [14] [15] [16]. The frequency of these forces is typically much lower than the wave frequencies, and they can excite the platform's surge or pitch natural frequencies, resulting in large pitch motion or additional loads on the mooring system. Depending on the floater concept and the required simulation accuracy, models that take into account the second-order wave forces are becoming the standard for load simulation. The simplest approach to include the slow drift forces is Newman's approximation [17], which considers only the difference-frequency terms. Alternatively, the full second-order wave forces can be captured by using the Quadratic Transfer Function (QTF) matrix [18].

In addition to the wave excitation forces, hydrodynamic damping plays an important role in modeling FOWTs. PF theory neglects the viscosity of the fluid, so the hydrodynamic drag forces are not included. Especially for floaters with sharp corners or large heave plates, quantifying the viscous damping correctly becomes essential for the coupled simulation and load analysis. The Morison equation is a widely used semi-empirical approach that consists of two terms, accounting for both the inertial forces and the drag forces. Physically speaking, the inertial forces in the Morison equation are the Froude-Krylov forces in the PF theory. For floaters with slender geometries, the Morison equation can fully represent the hydrodynamic loading. However, as the member size increases, diffraction effects become significant, and the Morison equation may not be applicable. In such cases, a combination of PF theory and the Morison equation is commonly used. In this work, the inertial and diffraction forces are described by the PF theory, while the viscous damping is captured by the drag term of the Morison equation.

#### 2.2.4 Engineering tools

There are a number of engineering models for FOWT simulation. The features of the tools that are used in this work are summarized in the section.

OpenFAST [19] is an open-source tool for research purpose developed by National Renewable Energy Laboratory (NREL)<sup>†</sup>. It consists of several submodules modeling the aerodynamics, hydrodynamics, structural dynamics, and more. The model

---

<sup>†</sup><https://github.com/OpenFAST/openfast>. Accessed on 30.Oct.2022

solves the coupled nonlinear aero-hydro-servo-elastic dynamics of wind turbines (including FOWTs) in the time domain. The ElastoDyn, BeamDyn, or SubDyn submodules can be used to model the structural dynamics as either rigid or flexible bodies. In this work, the platform is modeled as a rigid body, while the modal method is used for the tower and blades. The AeroDyn submodule models the aerodynamics of the turbine using BEMT, the effect of the wake can be corrected by including GDW, but only BEMT is considered here. Hydrodynamics are modeled using a combination of PF theory and the Morison equation that captures the viscous damping. The HydroDyn module models both regular and irregular waves, as well as currents. OpenFAST includes three submodules for modeling the mooring system: the MAP++ module (a quasi-static representation), the FEAMooring module (an FEM-based dynamic model), and the MoorDyn module, which describes the mooring system as a mass spring damper system and includes the hydrodynamic inertial and drag forces. In this work, either MAP++ or MoorDyn is used to capture the static and dynamic mooring loads.

The SLOW model, used in this work to simulate the dynamics of a FOWT, was originally developed by [2]. With the aim of achieving a good trade-off between model accuracy and computational efficiency, the model focuses on representing the system dynamics of a FOWT with only the necessary DOFs and the most relevant physical effects. A validation of the model against wave tank tests can be found in [20], and its applications for controller design, load case simulation, and integrated optimization has been demonstrated in several works [21, 22, 23, 20, 24]. The SLOW model is comprised of a structural model and some submodels for external aerodynamics, hydrodynamics, and mooring loads. The structural model adopts a flexible multi-body system (MBS) formulation, with a rigid platform and a flexible tower. The system state vector includes the surge, heave and pitch motion of the platform, the fore-aft movement of the tower top, the blade pitch angle, and the azimuth angle. The aerodynamic forces are calculated assuming the rotor as a rigid actuator disk. In practice, a look-up table is generated based on the aerodynamic torque and thrust coefficients for each tip speed ratio and blade pitch angle to represent the quasi-static aerodynamic forces and their derivatives at each operating point. The catenary mooring lines are modeled quasi-statically, with static mooring loads determined by a look-up table that contains the relationship between the

fairlead tension and the position of a single mooring line. Wave excitation loads that vary with frequency are calculated using hydrodynamic panel code, such as Ansys-AQWA. For a given wave spectrum, the first order wave loads can be calculated by transforming the resulting frequency-domain representation of the forces and moments to the time domain and added to SLOW as predefined time vectors. While hydrodynamic radiation damping is not considered, additional viscous drag damping is captured by the Morison equation.

## 2.3 Research on Structural Damper

Generally, reducing motions and loads is one of the ways to reduce the overall LCOE of FOWTs. As one of the promising vibration control systems, TLCD, also known as anti-roll U-tank, has been widely used for ships. Research on U-tank for reducing ship roll motion dates back to the early 20th century, when Frahm modified the free surface tank design [25]. Since then, numerous studies on numerical modeling, design methodologies, experimental validation, and active control have been carried out. A comprehensive review of the development and modeling of TLCDs in the field of naval architecture is presented in [26]. A brief summary that is relevant for understanding the work presented in this thesis is provided here.

The Euler's equation was first introduced by [27] to develop the mathematical representation for passive TLCDs. The formulation was simplified in [28], which became one of the classical analytical models. This model is intuitive, easy to implement, and can be used for geometry design. The Lagrange method was used by [29], and further developed and extended by [30]. The extended version not only takes into account more dynamics due to the additional coupling terms in the inertia matrix, but also allows a free choice of cross section other than a rectangular prism. In terms of design methodology, [31] provides a detailed analysis of the effect of damping coefficient, fluid mass, as well as the installation location on the performance of the TLCD, providing important insights into these design considerations.

The conventional TLCD, despite its decades-long development and widespread application in civil and naval engineering, faces new challenges when applied to FOWTs. With only two columns, it is often difficult to fit them into the specific geometry of a FOWT. Additionally, the unidirectional damping effect limits the

damping performance, especially when the turbine yaws and both roll and pitch motions become critical. One solution proposed in [32] is to install two conventional TLCDs orthogonally to dampen the tower's fore-aft and side-to-side motion of a tension leg platform type FOWT. However, such multi-TLCD systems have been found to be less robust, particularly in the presence of wind and wave misalignment, as discussed in [3]. Moreover, this solution is not suitable for many semi-submersible substructures with three vertical columns. To address these challenges, the idea of TLMCDs has been proposed by [3], which is a TLCD-like damping system with more than two interconnected vertical columns. This allows for a more flexible design and increases the FOWT's robustness in combined wind and wave loading conditions. It has been found that the TLMCDs can provide a more stable behavior and thus a better damping effect, as well as installation flexibility, compared to installing multiple conventional TLCDs in different directions. However, the analytical model for the TLMCD proposed in [3] has not been verified by numerical simulations or experiments. Thus, it is unclear whether the conventional mathematical derivation for two-column TLCDs applies to the more complex damping system consisting of multiple columns.

Another important research focus related to TLCD modeling is the accurate determination of the damping coefficient. To understand better the fluid motion, many researchers have performed numerical simulations of complex fluid behavior in TLCDs. For example, [33] uses CFD techniques to study the stabilizing effect of anti-roll tanks, while [34] analyzed sloshing in a road container using numerical simulations to track the movement on the free surface. The volume of fluid method is used by [35] to capture the nonlinear liquid sloshing inside a tank. The impact of cross section shape and geometric scaling on the damping coefficient of the TLMCD is investigated using CFD simulations by [36]. In the case of TLCDs for FOWTs, the damping characteristics also affect the blade pitch controller, making it crucial to have a reliable estimation and careful design of the damping coefficient.

Apart from the modeling aspects, many performance studies of TLCDs are also available, and it has been found that their effectiveness is highly dependent on the wave conditions. For example, Frahm's passive U-tank has been found to be efficient in regular waves, achieving a roll reduction of approximately 50%. However, in choppy seas, where waves spread in multiple directions and have different patterns,

it has been observed that the motion is poorly damped, often with no visible roll reduction [37]. Similar findings have been reported in the application of TLCDs to FOWTs, where a reduction in mean roll amplitude of only 2% has been observed [38]. The limitations of passive TLCD performance have been confirmed in the evaluation of both passive and semi-active TLCD by [39]. However, recent research has shown that the TLCD combined with the turbine blade pitch controller can efficiently damp platform resonances [40]. This concept extends the potential of passive TLCDs for offshore structures.

## 2.4 Different Control Approaches

Another aspect, which significantly influences the motions and loads of a FOWT, is the blade pitch controller. This is due to the strong coupling between the hydrodynamics, aerodynamics and servo dynamics. This section explains the underlying physical causes of this problem and summarizes the state-of-the-art solutions related to the control design.

### 2.4.1 The non-minimum phase behavior

Modern multi-megawatt wind turbines are typically blade-pitch controlled. For onshore blade-pitch controllers, the approach often used in the literature is to aim for a constant closed loop frequency and damping across the above rated wind speeds [41], [42], [9]. So that the overshoot, rise time, as well as the settling time of the step response remain similar at different operating points (i.e. wind speeds). This means that the control design is performance oriented. When adapting a state-of-the-art onshore blade pitch controller to a FOWT, the instability problem of the platform pitch mode due to the soft substructure, is a well-known challenge. This phenomenon, called negative aerodynamic damping, was first discussed in [43]. From the viewpoint of control theory, the non-minimum phase behavior or the Right-Half-Plane Zero (RHPZ) problem arise when feeding back the generator speed to the blade pitch at above-rated wind speed limits the control robustness and performance. This leads to a larger generator speed fluctuation and higher tower base bending moment. Thus, stability becomes a driving factor for control of FOWTs.

## 2.4.2 Control approaches

To solve the non-minimum phase issue mentioned previously, a variety of methods addressing the RHPZ have been studied in recent years. A straightforward method is to detune the blade-pitch controller. Most recent research moves to more complex control approaches by adding additional sensors, actuators, or using model based control algorithms. All methods can be categorized into four categories and are summarized here:

- **Reduce bandwidth (single-input-single-output control)**

A pioneering solution to address the limitations of Single-Input Single-Output (SISO) controllers for FOWTs is proposed by [43]. The method retains the SISO control structure, but detunes the gains of the collective pitch controller such that the maximum closed-loop control frequency is below the pitch natural frequency of the floater. Compared to onshore turbines, this results in a significant reduction in control bandwidth, at which the controller is effective. Nevertheless, the method has been widely adopted by many other researchers to date due to its simplicity and ease of implementation. However, as the size of wind turbines increases and the natural frequency of the correspondingly larger supporting substructure decreases, further reduction of the bandwidth of the blade pitch controller can lead to insufficient performance in generator speed tracking [21]. As a result, recent research has focused on more complex control approaches that involve additional sensors, actuators, or model-based control algorithms.

- **Extra sensors (multi-input-single-output control)**

In [1], improved control performance is achieved by adding extra loops that feed back the platform pitch velocity and tower top velocity to the blade pitch. Another promising control sensor is LiDAR, which provides inflow information ahead of time. By applying feedforward control strategy, the effect of changing wind speeds on rotor speed can be compensated for before they can impact the turbine. For instance, the Lidar assisted feedforward control proposed by [44] uses wind preview data to adjust blade pitch and counteract the effects of wind speed changes. However, additional sensors can introduce measurement uncertainty and malfunctions, which can affect the reliability of the controllers.

As such, it is crucial to design robust and fault-tolerant control strategies that can handle sensor failures and other uncertainties.

- **Extra actuators (multi-input-multi-output control)**

The benefit of controlling the generator speed by regulating the generator torque is that the aerodynamic thrust will not be directly affected. It has been shown that feedback of the nacelle velocity to the generator torque can compensate for the non-minimum phase zeros [45], which is the origin of the instability problem. Similar result has been demonstrated for a different FOWT concept in [21]. However, the generator torque can only be regulated within a limited margin, leading to only a marginal improvement in system performance. Other actuators, such as active structural dampers and active ballast systems, have also been suggested in various studies to improve the overall system response. However, adding more actuators will inevitably increase maintenance costs.

- **Advanced control algorithm**

Model-based control strategies, such as the Linear Quadratic controller [23, 46] and the H-infinity approach [47], provide a systematic way to handle multi-input, multi-output systems. Model predictive control has also been adapted to FOWTs and has demonstrated good performance in damping platform motions and reducing loads [48]. Disturbance accommodating controllers can minimize the impact of wind speed perturbations [46], and individual blade pitch control has proven to be effective in reducing platform pitch motions [49]. However, the implementation of these model-based control approaches can be complex and strongly dependent on the quality of the model, as well as computationally expensive, which can pose challenges for their practical application.

To summarize, advanced controllers have shown promising control performance compared to traditional Proportional-Integral (PI) controllers. However, their success is highly dependent on the quality of sensors, actuators, and numerical models. As a result, advanced controllers remain primarily the focus of academic research and it is challenging to implement them in early demonstrators. The barrier stems from both limited access to the controller provided by the turbine manufacturers

and the reliability of additional sensors. In addition, controllers using advanced algorithms often require an online numerical model of the FOWT. However, uncertainties associated with these complex models, along with the representation of stochastic environmental conditions, can limit significantly the control performance in the real world. Given these facts, it is clear that the SISO PI blade-pitch controller remains a popular choice in the wind industry due to its simplicity and robustness, while still providing satisfactory control performance. However, as the wind industry moves towards floating platforms, where environmental conditions become more complex and induce additional motions and loads, SISO controllers may not meet the necessary control requirements. Therefore, the question of whether a detuning procedure for the simple controller can ensure full functionality and effectiveness in these challenging environments needs to be further investigated.

## 2.5 Control Co-Design

Sections 2.3 and Sections 2.4 explore potential solutions for reducing the motions and loads of a FOWT. However, given the highly coupled nature of the system, it is difficult to make progress by focusing solely on individual subsystems without considering their impact on other subsystems and the overall system. This is particularly true for actively controlled systems, where dynamic characteristics play a central role in determining the design of the control system. This is where Control Co-Design (CCD) approaches become important.

Figure 2.1 illustrates four general approaches to designing and optimizing an active system. The sequential design approach, whether one-way or iterative, optimizes different subsystems in isolation. In the case of FOWTs, the industry typically uses a sequential or iterative sequential design process. For instance, the substructure and the blade pitch controller are highly coupled subsystems due to the interaction of the controller with the hydrodynamics and aerodynamics. However, the control system is typically optimized as an independent step after the substructure design is finalized, when the hydrodynamic characteristics of the system are fixed. This approach may lead to more conservative designs that may not fully leverage on the potential cost reductions achievable by incorporating advanced sensing and control technologies into the substructure design process. As a consequence, control engineers may



encounter a situation where they think, 'If only I could modify the dynamic plant  $G$  (such as the substructure or tower design), the overall active system performance would significantly improve.

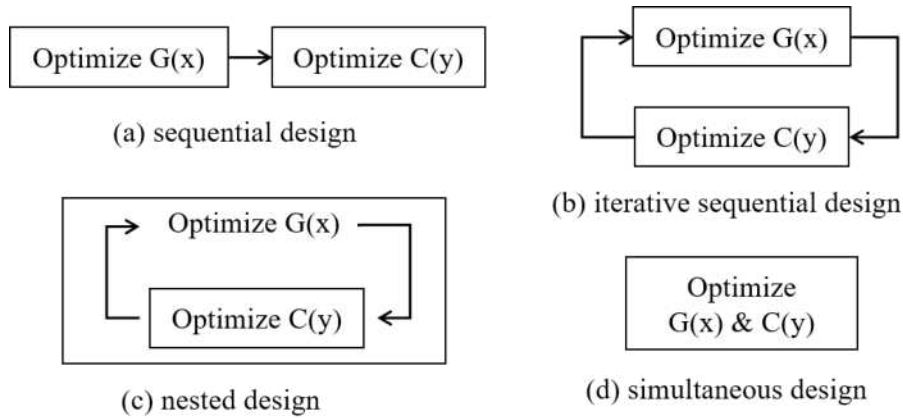


**Figure 2.1:** Multidisciplinary design optimization method.

Given the challenges of designing and optimizing FOWTs, there has been growing interest in optimizing simultaneously the subsystems, particularly the dynamic plant and the controller, which is known as the CCD. The ARPA-E ATLANTIS Program <sup>†</sup> has already announced several projects focusing on this topic [50]. The key challenge here is to determine how the subsystems of a FOWT can be designed to interact synergistically for optimal performance. Such a CCD optimization approach can play an important role in Multidisciplinary Design Optimization (MDO) methodologies, exploring potential physical and control system design solutions that enable new levels of performance and functionality.

## 2.6 Reference Models

Three FOWTs are used as reference models in this work. The DTU 10 MW reference wind turbine [51] is the only wind turbine used to demonstrate the developed methods. The key properties of this turbine are provided in Table 2.1. In addition, three substructure designs developed for the DTU 10 MW reference wind turbine

<sup>†</sup><https://arpa-e.energy.gov/technologies/programs/atlantia>. Accessed on 20.Oct.2022

are used, as illustrated in Figure 2.2. These designs include the 10 MW Reduced Draft Spar (RDS) concept from the Concrete Reduced-draft Offshore Wind turbine for iNdustry (CROWN) project, as well as the OO-Star and Nautilus-10 concepts, which are developed within the LIFES50+ project [52].

**Table 2.1:** System properties of the DTU 10 MW reference wind turbine.

Properties	Unit	Value
rated power	MW	10
hub height	m	118.39
rotor diameter	m	178.2
rotor mass	kg	230717
nacelle mass	kg	446006

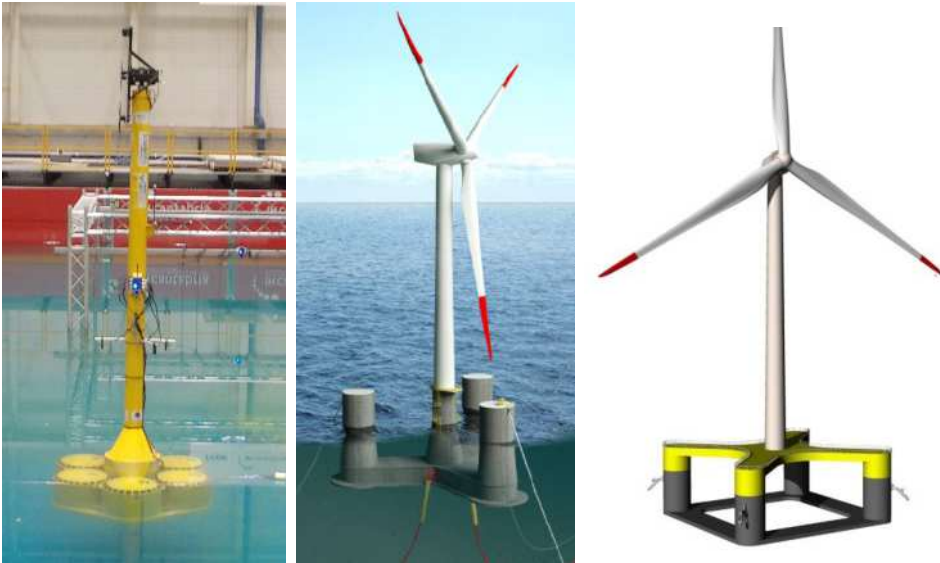


**Figure 2.2:** Three FOWT concepts used in this thesis: CROWN 10MW RDS FOWT (left); LIFES50+ OO-Star Wind Floater Semi 10MW (center); LIFES50+ NAUTILUS-DTU10 MW FOWT (right).

The CROWN 10 MW RDS concept is utilized to validate the coupled TLMCD and FOWT numerical model in Chapter 4. The OO-Star and NAUTILUS-10 concepts

**Table 2.2:** System properties of the FOWTs used for evaluation.

Properties	CROWN	OO-Star	NAUTILUS-10
wind turbine	DTU 10MW	DTU 10MW	DTU 10MW
platform material	concrete	concrete	steel
pitch natural period [s]	28	33	30

are used to assess the design methodology, which adapts the blade pitch controller for TLMCD damped FOWTs in Chapter 5. In addition, a quasi-NAUTILUS concept is employed as an initial starting point for the CCD optimization. The original NAUTILUS-10 concept is equipped with an active ballast system with varying ballast mass and center of gravity over operating wind speeds. This feature is however not implemented in the quasi-NAUTILUS concept. Table 2.2 provides a summary of the main system characteristics of the three FOWTs.



# 3 Numerical Tool: Modelling, Coupling and Verification

Good tools are essential for the successful execution of a task. Therefore, this chapter establishes the numerical tools used throughout the thesis. The physical basis for the numerical model is based on both the Newton-Euler equations (Newtonian mechanics) and the Lagrangian mechanics. When the coordinates are defined consistently, Newton's and Euler's axioms result in an equivalent mathematical expression for the dynamics as the principles of Lagrangian mechanics. This provides flexibility in deriving the equations of motion for complex systems, such as the coupled TLMCD and FOWT system studied in this work. The main result of this chapter is published in [53], but the methodology is described in more detail in the following sections. The chapter begins with fundamental but essential definitions, including the coordinates and the FOWT system. Next, the equations of motion of a TLMCD are set up. A simplified formulation for TLMCDs with uniform cross sections is derived and linearized for specific applications, such as control design. The TLMCD is then coupled to two existing numerical models for FOWTs, i.e. openFAST and SLOW. Different coupling methods are implemented in the SLOW model, and their simulation results are compared. Finally, a code-to-code comparison between openFAST and SLOW is carried out to verify the developed numerical model.

## 3.1 Reference Coordinates and Transformation

The substructure of a FOWT is usually considered as a rigid body, whose dynamics can be described by the Newton-Euler equations or Lagrangian mechanics. It is convenient to describe the motion of a rigid floating substructure using two frames(coordinates), i.e. an earth-fixed inertial frame and a body-fixed frame.

To describe the location of an arbitrary rigid body, the position of the origin of the body-fixed frame expressed in the inertial frame is used, denoted by  $\mathbf{x} = [x, y, z]^\top$ . The orientation of the body can be described by the Euler angle  $\Theta = [\varphi, \beta, \psi]^\top$ .<sup>†</sup>

The corresponding rotation matrices about each axis are:

$$\begin{aligned} \mathbf{R}_x(\varphi) &= \begin{bmatrix} 1 & 0 & 0 \\ 0 & \cos(\varphi) & -\sin(\varphi) \\ 0 & \sin(\varphi) & \cos(\varphi) \end{bmatrix}, \\ \mathbf{R}_y(\beta) &= \begin{bmatrix} \cos(\beta) & 0 & \sin(\beta) \\ 0 & 1 & 0 \\ -\sin(\beta) & 0 & \cos(\beta) \end{bmatrix}, \\ \mathbf{R}_z(\psi) &= \begin{bmatrix} \cos(\psi) & -\sin(\psi) & 0 \\ \sin(\psi) & \cos(\psi) & 0 \\ 0 & 0 & 1 \end{bmatrix}. \end{aligned} \tag{3.1}$$

To rotate a rigid body from its initial orientation to any given orientation in space, different rotation sequences are possible. For ships or aircrafts, the sequence of ZYX is usually used, which is called Cardan angles, the rotation matrix in this case is

$$\mathbf{R}(\Theta) = \mathbf{R}_z(\psi)\mathbf{R}_y(\beta)\mathbf{R}_x(\varphi). \tag{3.2}$$

An important feature, independent of the rotation sequences, is the transpose of the transformation matrix:

$$\mathbf{R}^\top(\Theta) = \mathbf{R}(\Theta)^{-1}. \tag{3.3}$$

Velocities of a rigid body are defined in a body-fixed frame. With the rotation matrix, one can connect the linear velocities in the body-fixed frame  $\mathbf{v}$  and the direct time derivative of the coordinates described in the inertial frame by

---

<sup>†</sup>Conventionally either  $\varphi, \theta, \psi$ , or  $\alpha, \beta, \gamma$  are used, since for wind turbines,  $\theta$  is often used to describe the blade pitch angle which is also the case in this work, a mixed notation is used. There are different names for the orientation angles, depending on the rotation sequence, proper Euler angles and Tait-Bryan angles are the two big categories, but both of them are called "Euler angles" in a general sense. This work uses Tait-Bryan angles, but will be referred to as Euler angles.

$$\mathbf{v}^b = \mathbf{R}^\top \dot{\mathbf{x}}. \quad (3.4)$$

Regarding the angular velocities  $\boldsymbol{\omega}^b$ , it's important to note that they cannot be directly integrated to determine the actual orientation coordinates. To address this issue, a transformation matrix  $\mathbf{G}$  is defined according to relation between the direct time derivative of the Euler angles and the angular velocities in the body fixed frame. With ZYX rotation sequence, this relation is expressed as:

$$\boldsymbol{\omega}^b \triangleq \mathbf{G}\dot{\boldsymbol{\Theta}} = \begin{bmatrix} \dot{\varphi} \\ 0 \\ 0 \end{bmatrix} + \mathbf{R}_x^\top \begin{bmatrix} 0 \\ \dot{\beta} \\ 0 \end{bmatrix} + \mathbf{R}_x^\top \mathbf{R}_y^\top \begin{bmatrix} 0 \\ 0 \\ \dot{\psi} \end{bmatrix}. \quad (3.5)$$

Therefore,  $\mathbf{G}$  can be determined as a function of Euler angles and is written as

$$\mathbf{G}(\boldsymbol{\Theta}) = \begin{bmatrix} 1 & 0 & -\sin \beta \\ 0 & \cos \varphi & \cos \beta \sin \varphi \\ 0 & -\sin \varphi & \cos \beta \cos \varphi \end{bmatrix} \quad (3.6)$$

In summary, if the location and orientation of a rigid body are defined as a vector written as  $[\mathbf{x}^\top, \boldsymbol{\Theta}^\top]^\top = [x, y, z, \varphi, \beta, \psi]^\top$ , then the corresponding velocities described in the body fixed frame are computed by the transformation matrices  $\mathbf{R}$  and  $\mathbf{G}$ , which is expressed as

$$\begin{bmatrix} \mathbf{v}^b \\ \boldsymbol{\omega}^b \end{bmatrix} = \begin{bmatrix} \mathbf{R}(\boldsymbol{\Theta})^\top & 0_{3 \times 3} \\ 0_{3 \times 3} & \mathbf{G}(\boldsymbol{\Theta}) \end{bmatrix} \begin{bmatrix} \dot{\mathbf{x}} \\ \dot{\boldsymbol{\Theta}} \end{bmatrix}. \quad (3.7)$$

## 3.2 Simplified Low Order FOWT Model

The SLOW model, introduced in Chapter 2, is used to simulate the dynamics of the FOWT in the coupled model. To evaluate the dynamic performance of the TLMCD model, the two-dimensional (2D) FOWT motions are extended to a three-dimensional (3D) by enabling additional DOFs of the platform. The model consists of a structural module and several sub-modules that account for external applied

loads, including aerodynamic, hydrodynamic, and mooring loads. The physical theories and mathematical expressions of this model are briefly summarized below, which is helpful in understanding the coupling between the TLMCD and the FOWT to be introduced later.

The equations of motion for the SLOW model are derived using a flexible MBS formulation with a tree structure. The platform is modeled as a rigid body with five DOFs (surge, sway, heave, roll, and pitch), while the elastic tower has only one DOF for the tower top fore-aft motion. The open loop tree structure is advantageous for incorporating additional dynamic components, such as the structural damper studied in this work. The MBS formulation is based on the fundamental physical principles of the Newton-Euler equations, which describe the linear and angular kinematics of a body and their relationship with the external forces and moments acting on the body. When considering an arbitrary body  $i$ , the Newton-Euler equations can be written as

$$\begin{aligned} \mathbf{m}_i \mathbf{a}_i &= \mathbf{f}_i^a + \mathbf{f}_i^r \\ \mathbf{I}_i \boldsymbol{\alpha}_i + \tilde{\mathbf{S}}(\boldsymbol{\omega}_i) \mathbf{I}_i \boldsymbol{\omega}_i &= \mathbf{l}_i^a + \mathbf{l}_i^r, \end{aligned} \quad (3.8)$$

where  $\mathbf{a}_i$ ,  $\boldsymbol{\alpha}_i$  and  $\boldsymbol{\omega}_i$  are the linear acceleration, angular acceleration and angular velocity of the rigid body defined in the initial frame. Note the cross-product  $\tilde{\mathbf{S}}(\cdot)$  in the equation represent:

$$\tilde{\mathbf{S}}(\boldsymbol{\omega}_i) \mathbf{I}_i \boldsymbol{\omega}_i \triangleq \boldsymbol{\omega}_i \times \mathbf{I}_i \boldsymbol{\omega}_i. \quad (3.9)$$

All the loads are written on the right hand side, including the external applied forces  $\mathbf{f}_i^a$  and moments  $\mathbf{l}_i^a$ , as well as the reaction loads  $\mathbf{f}_i^r$  and  $\mathbf{l}_i^r$ , coming from the connected neighboring bodies.

The velocities can be obtained by direct time differentiation of the body velocities. Assuming a system with generalized coordinates (or minimal coordinates)  $\mathbf{q}$ , the body velocities, equivalent to the velocities  $\mathbf{v}_g$  and  $\boldsymbol{\omega}_b$  in Equation 2.3, can be calculated by

$$\begin{aligned} \mathbf{v}_i(\mathbf{q}, \dot{\mathbf{q}}) &= \mathbf{R}(\boldsymbol{\Theta})^\top \mathbf{J}_{t,i}(\mathbf{q}) \dot{\mathbf{q}} \\ \boldsymbol{\omega}_i(\mathbf{q}, \dot{\mathbf{q}}) &= \mathbf{G}(\boldsymbol{\Theta}) \mathbf{J}_{r,i}(\mathbf{q}) \dot{\mathbf{q}}, \end{aligned} \quad (3.10)$$



where  $\mathbf{J}_{t,i}$  and  $\mathbf{J}_{r,i}$  are Jacobian matrices for each body, giving the kinematics in the initial coordinates of that body based on  $\mathbf{q}$ . As discussed in Section 3.1, the transformation matrices  $\mathbf{R}$  and  $\mathbf{G}$  can transform the vector described in the inertial coordinates to the body fixed coordinates. Regarding the accelerations in Equation 3.8, they can be calculated by the time differentiation of the body velocity, which are

$$\begin{aligned}\mathbf{a}_i &= \dot{\mathbf{v}}_i \\ \boldsymbol{\alpha}_i &= \dot{\boldsymbol{\omega}}_i.\end{aligned}\tag{3.11}$$

The complete expression of  $\mathbf{a}_i$  and  $\boldsymbol{\alpha}_i$  is rather complex. For a floating platform which has a small roll motion and the yaw motion is fixed,  $\mathbf{R}$  and  $\mathbf{G}$  can be neglected. Therefore the Equation 3.8 becomes

$$\begin{aligned}m_i \mathbf{J}_{t,i} \ddot{\mathbf{q}} + m_i \dot{\mathbf{J}}_{t,i} \dot{\mathbf{q}} &= \mathbf{f}_i^a + \mathbf{f}_i^r \\ \mathbf{I}_i \mathbf{J}_{r,i} \ddot{\mathbf{q}} + \mathbf{I}_i \dot{\mathbf{J}}_{r,i} \dot{\mathbf{q}} + \tilde{\mathbf{S}}(\boldsymbol{\omega}_i) \mathbf{I}_i \boldsymbol{\omega}_i &= \mathbf{l}_i^a + \mathbf{l}_i^r\end{aligned}\tag{3.12}$$

It is important to emphasize here that this simplification applies only to the platform, but not to the tower and the nacelle.

Assuming that there is a MBS with  $p$  bodies and  $f$  DOFs, multiplying the Equation 3.8 by the transpose of the global Jacobian matrix

$$\mathbf{J}^\top = [\mathbf{J}_{t,1}^\top, \dots, \mathbf{J}_{t,p}^\top, \mathbf{J}_{r,1}^\top, \dots, \mathbf{J}_{r,p}^\top] \in \mathbb{R}^{f \times 6p}\tag{3.13}$$

from the left, the internal reaction forces  $\mathbf{f}_i^r$  and moments  $\mathbf{l}_i^r$  can be eliminated according to the principle of d'Alembert [2]. Equation 3.12 can be further simplified as

$$\mathbf{M}(\mathbf{q}) \ddot{\mathbf{q}} + \mathbf{c}(\dot{\mathbf{q}}, \mathbf{q}) = \boldsymbol{\tau}(\dot{\mathbf{q}}, \mathbf{q}),\tag{3.14}$$

where  $\mathbf{M}(\mathbf{q}) \in \mathbb{R}^{f \times f}$  denotes the system inertia and  $\mathbf{c}(\dot{\mathbf{q}}, \mathbf{q}) \in \mathbb{R}^{f \times 1}$  represents the total Coriolis, centrifugal and gyroscopic forces. Note that the hydrodynamic added mass is also included in  $\mathbf{M}$ , how to handle this additional mass term can be found in [2], which will not be explained here. The external applied loads are included in the vector  $\boldsymbol{\tau} \in \mathbb{R}^{f \times 1}$ , which will be described in the following section.

External forces  $\boldsymbol{\tau}$  exerted on the FOWT are mainly from the aerodynamics, hydrodynamics, as well as the mooring system. How these forces are handled is described

already in Section 2.2.4. More details can be found in [2].

It is advantageous to linearize the numerical model for control design purposes. For a FOWT, this mainly concerns the aerodynamic forces and the mooring forces, sometimes also the hydrodynamics if Morison equations are used to represent the viscous drag forces. As a final result, the SLOW can be transformed into the linear format:

$$\mathbf{M}(\mathbf{q})\ddot{\mathbf{q}} + \mathbf{C}(\dot{\mathbf{q}})\dot{\mathbf{q}} + \mathbf{K}(\mathbf{q})\mathbf{q} = \boldsymbol{\tau}_0. \quad (3.15)$$

Here  $\mathbf{C}(\dot{\mathbf{q}})$  is a velocity-dependent matrix, resulting from both the external applied forces (mainly the aerodynamic and hydrodynamic forces) and the Coriolis and centrifugal forces. The matrix  $\mathbf{K}(\mathbf{q})$  includes the position dependent terms from the hydrostatics, mooring lines, the centrifugal forces and the gravitational forces. The applied forces  $\boldsymbol{\tau}_0$  consist of the loads from the environment that are independent of the kinematics of the FOWT.

### 3.3 Two-column Tuned Liquid Damper Model

Before analyzing the dynamics of TLMCD, it is helpful to derive the equations of motion for a simple TLCD with two columns. Figure 3.1 shows a basic TLCD. As can be seen, it consists of two vertical square columns connected by a horizontal duct. Such TLCDs are widely used in naval and civil engineering. The analytical formulation of the equations of motion, which dates back to the 19th century, is still in use today.

To allow a concise mathematical description of the fluid motion inside the TLCD, several assumptions are necessary:

- The cross sections of the vertical and horizontal columns are constant respectively
- The fluid inside the TLCD is incompressible
- Fluid velocity is uniform and flows along the central line of the column, which is called the streamline
- Free surface is perpendicular to the streamline
- Free surface is open to air, i.e. above the free surface is the atmospheric pressure

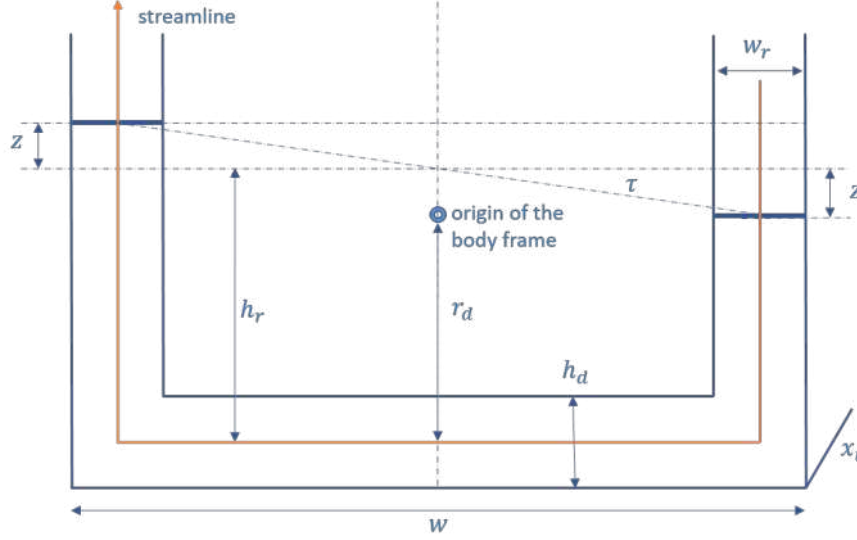


**Figure 3.1:** Schematic of a passive two-column TLCD with notation [40].

- The position of the free surface is always within the vertical column, i.e. the horizontal column is always full of fluid

Based on these assumptions, only one degree of freedom is necessary to describe the flow condition inside the TLCD. This is denoted by  $z$  in Figure 3.1, representing the change in the position of the fluid free surface with respect to that in steady state, which is expressed in the TLCD-fixed body frame. When  $z$  is relatively small, it can be replaced by  $z = \tau w/2$ , the case in [28] which leads to an equivalent result.

There are different methods to derive the equations of motion of the fluid flow inside the TLCD. One of the classical approaches is based on Euler's equation. Since the fluid is incompressible, the Euler's equation for the fluid flow is expressed as

$$\frac{\partial v_i}{\partial t} + \sum_{j=1}^3 \frac{\partial v_i}{\partial x_j} v_j + \frac{1}{\rho} \frac{\partial P}{\partial x_i} = k_i \quad (i = 1, 2, 3), \quad (3.16)$$

where  $v_i$ ,  $\rho$  and  $P$  are the fluid velocity, density and local pressure of the  $i_{th}$  component, respectively, and  $x_i$  represents an arbitrary unit length along the coordinate axis. The external force per unit mass  $k$  can be friction force, inertial forces due to gravity, or platform motions. Since it is assumed that the fluid flows always along the streamline and the cross section is constant, i.e.  $\frac{\partial v_i}{\partial x_j} = 0$ . To simplify the formu-

lation, curvilinear coordinates can be used to describe the streamline, the direction of which is indicated by an arrow at the end of the streamline. As a result, there are only two variables left, and Equation 3.16 can be reduced to

$$\frac{dv}{dt} + \frac{1}{\rho} \frac{dP}{ds} = k, \quad (3.17)$$

where  $s$  represents an arbitrary unit length on the curvilinear coordinate following the streamline. If  $z$  is used to describe the height difference of the fluid level in the two vertical columns, the local fluid speed can be written as

$$v = \begin{cases} \dot{z}, & \text{in the vertical column} \\ \dot{z} \frac{w_r}{h_d}, & \text{in the connecting duct} \end{cases} \quad (3.18)$$

The difference of the hydrostatic pressure  $P$  inside the TLCD due to the moving free surfaces is

$$\Delta P = 2\rho g z. \quad (3.19)$$

As for the external force per streamline length  $k$ , when neglecting the motion of the platform, only the damping forces due to the friction or vortex shedding at the corners of the structure are considered. Defining the damping ratio by rule of thumb is difficult. Both [54] and [55] have discussed the determination of the damping ratio, using CFD simulation and experimental tests. One main conclusion from the studies is that both linear and quadratic damping should be considered. To simplify the explanation and expression, the linear damping term will be used as an example in the following derivation. The quadratic damping term will be further elaborated in the following sections. Since the linear damping force is proportional to the fluid velocity with respect to the structure, a coefficient  $d_1$  can be defined, with the unit of  $[kg/s]$  or  $[N/(m/s)]$ . Then the damping force  $k$  can be written as

$$k = \begin{cases} \dot{z} \cdot \frac{-d_1}{\rho w_r x_t ds}, & \text{in the vertical column} \\ \dot{z} \frac{w_r}{h_d} \cdot \frac{-d_1}{\rho h_d x_t ds}, & \text{in the connecting duct} \end{cases} \quad (3.20)$$

By inserting all the components, i.e. Equation 3.18-3.20, into Equation 3.17, and

integrating along the streamline  $\int_{\text{TLCD}} \delta s$ , the Euler equation yields

$$\rho(2h_r + \frac{w_r w}{h_d}) \ddot{z} + 2\rho g z = -2d_1(\frac{1}{w_r x_t} + \frac{w_r}{h_d^2 x_t}) \dot{z}. \quad (3.21)$$

After multiplying the equation with the fluid mass of each cross section  $w_r x_t$ , the equation can be rewritten as

$$\rho(2h_r w_r x_t + \frac{w w_r^2 x_t}{h_d}) \ddot{z} + 2d_1(1 + \frac{w_r^2}{h_d^2}) \dot{z} + 2g\rho w_r x_t z = 0. \quad (3.22)$$

For conventional TLCDs,  $w_r$  is much larger than  $h_d$ , therefore, the damping term due to the friction in the vertical column can be neglected, i.e.  $1 + \frac{w_r^2}{h_d^2} \approx \frac{w_r^2}{h_d^2}$ .

To simplify the representation of Equation 3.22, the following notation is used:

$$\begin{aligned} A_{\text{tt}} &= \rho A_v (2h_r + \frac{A_v w}{A_h}) \\ B_{\text{tt}} &= 2d_1 \frac{A_v^2}{A_h^2} \\ C_{\text{tt}} &= 2g\rho A_v \end{aligned} \quad (3.23)$$

where  $A_v = w_r x_t$  and  $A_h = h_d x_t$  are the cross section areas of the vertical and horizontal columns, respectively. Considering also the forces coming from the floating platform, the equation of motion of a TLCD with rectangular prism shape is then given by

$$A_{\text{tt}} \ddot{z} + B_{\text{tt}} \dot{z} + C_{\text{tt}} z = \tau_{\text{ptfm}}, \quad (3.24)$$

where  $A_{\text{tt}}$ ,  $B_{\text{tt}}$ ,  $C_{\text{tt}}$  are all geometry-dependent coefficients, which characterize the fluid dynamics inside the TLCD. Equation (3.24) represents a classical second order system driven by the platform motions. More specifically, the resulting force  $\tau_{\text{ptfm}}$  depends on the platform pitch angle  $\beta_p$ , the acceleration  $\ddot{\beta}_p$  and the surge acceleration  $\ddot{x}_p$ . This part is formulated on the right hand side of the equation. Because of the action and reaction forces, the TLCD contributes with the stabilizing moment  $\tau_{\text{TLCD}}$  to reduce the platform pitch motion.

If the motion of the free surface level  $z$  is relatively small compared to the distance between the two vertical columns  $w$ , it is also possible to use the angle  $\tau$  to describe the fluid motion, which means  $z = \tau w/2$ . Since the motion variable in this case is

an angle, the moment of area of the vertical column cross section  $w w_r x_t / 2$  will be multiplied to the original Euler's equation. This preserves the form of the basic equation of rotational motion, which gives a better physical interpretation and leads to the following expression:

$$\rho \left( \frac{h_r w_r x_t w^2}{2} + \frac{w^3 w_r^2 x_t}{4 h_d} \right) \ddot{\tau} + d_1 \left( \frac{w^2}{4} + \frac{w^2 w_r^2}{4 h_d^2} \right) \dot{\tau} + \frac{\rho g w_r x_t w^2}{2} \tau = 0. \quad (3.25)$$

Equation 3.25 is in line with the classical model presented in [28, p. 265]. Note that the damping coefficient  $d_1$  is defined differently in this work.

The analytical model presented by [28] neglects several coupling terms between the TLCD and the platform. For example, loading and unloading the TLCD will change the total mass of the FOWT system, as well as the center of gravity and the moment of inertia, this effect is however not considered. According to [28], the neglected terms do not significantly affect the behavior of the model if the fluid mass of the TLCD is less than 5% of the total system mass.

### 3.4 Tuned Liquid Multi-Column Damper Model

The TLCD model introduced in the previous section has been widely used in naval and civil engineering for over a century. It is simple, easy to understand and implement, and nevertheless still generates satisfactory engineering results. However, there are several obstacles to applying this model to FOWTs. The first is due to the specific configuration of FOWTs. For state-of-the-art FOWT designs, which typically do not have large space, a conventional TLCD concept could be difficult to be integrated. Furthermore, unlike ships, which only need to be damped in roll motion (unidirectional damping), FOWTs tend to be symmetrical and thus require damping in both roll and pitch motion (bidirectional damping). This is how the concept of TLMCD was inspired in [3]. Due to the increasing complexity of the system, the authors derived the mathematical equations of the analytical model using a Lagrangian mechanics based method, which originates from [55]. It is the basis of the analytical model used in this work. Since the coordinates of the TLMCD and the coupling methodology are different in this work, the essential equations are derived again in the following sections. The basic modeling assumptions are the

same as for the TLCD modeling defined in Section 3.3.

### 3.4.1 Coordinates and notation

Before deriving the equations of motion, it is important to define the essential parameters that characterize a TLMCD. As discussed in Section 3.3, using the geometrical parameters shown in Figure 3.1 can result in very long and complex equations of motion, especially as the number of vertical columns increases. However, by using the cross sectional area and column length as defined in Equations 3.23 - 3.24, the equations can be simplified without altering the physical meaning of the TLMCD. Therefore, in this work, the TLMCD is defined based on its cross sectional area and column length.

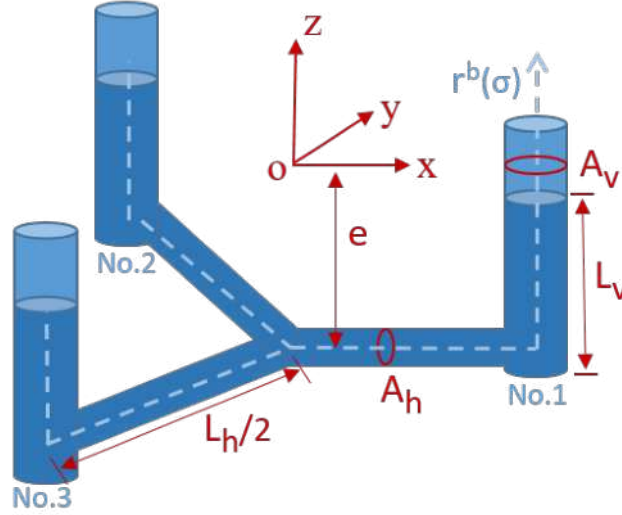


**Figure 3.2:** Sketch of a TLMCD showing the notation of geometrical parameters and the body fixed reference coordinate.

Figure 3.2 shows the notation used for the geometrical parameters of the TLMCD. The cross-sectional areas of the vertical and horizontal columns are denoted by  $A_v$  and  $A_h$ , respectively.  $L_v$  represents the vertical fluid height with respect to the center line of the horizontal arm at steady state, while  $\frac{L_h}{2}$  represents the length of the horizontal column. The use of  $\frac{L_h}{2}$  rather than  $L_h$  is consistent with the notation convention used for two-column TLCDs, which allows for easier comparison. In

addition, the body-fixed coordinate system, attached to the floating platform, is also shown, and  $e$  represents the vertical distance between this coordinate system and the horizontal arms of the TLMCD.

As for the configuration, the demonstrated TLMCD system in the figure consists of three elements, each of which can be considered as half of a conventional two-column TLCD, comprising half of the horizontal column and an attached vertical column. For convenience, these elements are numbered from No.1 to 3.

The general modeling approach, in particular the kinematic description, used for the two-column TLCD still applies in the case of multi-column TLCDs. However, since the fluid flow must be modeled across multiple columns, local curvilinear coordinates are used to describe the streamline in each column. The positive direction is defined as pointing outwards from the vertical column, as indicated by the arrow at the end of the dashed line. In the case of three columns, three curvilinear coordinates are needed, with each coordinate originating at the junction point of the three horizontal columns and pointing outwards from the respective vertical column. Here,  $\sigma_i$  (where  $i = 1, 2, 3$ ) can be used as generalized coordinates to describe each streamline.

Given this definition, it is convenient to map arbitrary points along a streamline to a body-fixed Cartesian coordinate system. For convenience, the TLMCD uses the same body-fixed (platform-fixed) coordinate system as that used for the platform. This coordinate system coincides with the Earth-fixed inertial coordinate system at steady state when the wind turbine is not attached. For element No.1, which is located in the  $xz$ -plane with positive flow pointing in the positive  $x$ -axis and  $z$ -axis directions, the mapping of the streamline to the Cartesian coordinate system is expressed as follows:

$$\begin{aligned} x^b(\sigma_i) &\triangleq \begin{cases} \sigma_i, & \forall \sigma_i \in [0, L_h/2) \\ L_h/2, & \forall \sigma_i \in [L_h/2, +\infty), \end{cases} \\ y^b(\sigma_i) &\triangleq 0, \\ z^b(\sigma_i) &\triangleq \begin{cases} e, & \forall \sigma_i \in [0, L_h/2) \\ e + \sigma_i - L_h/2, & \forall \sigma_i \in [L_h/2, +\infty). \end{cases} \end{aligned} \tag{3.26}$$



Then the corresponding derivatives can be calculated:

$$\begin{aligned}\frac{dx^b(\sigma_i)}{d\sigma_i} &\triangleq \begin{cases} 1, & \forall \sigma_i \in [0, L_h/2) \\ 0, & \forall \sigma_i \in [L_h/2, +\infty), \end{cases} \\ \frac{dy^b(\sigma_i)}{d\sigma_i} &\triangleq 0, \\ \frac{dz^b(\sigma_i)}{d\sigma_i} &\triangleq \begin{cases} 0, & \forall \sigma_i \in [0, L_h/2) \\ 1, & \forall \sigma_i \in [L_h/2, +\infty). \end{cases}\end{aligned}\quad (3.27)$$

Therefore, the position vector and its derivative of an arbitrary point along a streamline in element No. $i$  can be written as

$$\begin{aligned}\mathbf{r}^b(\sigma_i) &\triangleq [x^b(\sigma_i), 0, z^b(\sigma_i)]^\top \\ \frac{d\mathbf{r}^b(\sigma_i)}{d\sigma_i} &\triangleq \left[ \frac{dx^b(\sigma_i)}{d\sigma_i}, 0, \frac{dz^b(\sigma_i)}{d\sigma_i} \right]^\top.\end{aligned}\quad (3.28)$$

To place the vertical column at flexible directions, an element can be rotated  $\alpha_i$  degrees about the z-axis of the body frame, the Cartesian coordinates are then rotated and become

$$\mathbf{R}_z(\alpha_i)\mathbf{r}^b(\sigma_i), \quad i = 1 \dots N, \quad (3.29)$$

where  $\mathbf{R}_z(\alpha_i)$  is the rotation matrix about z-axis. According to the principle of Equation 3.1,  $\mathbf{R}_z(\alpha_i)$  is a function of  $\alpha_i$  and can be written as

$$\mathbf{R}_z(\alpha_i) = \begin{bmatrix} \cos(\alpha_i) & -\sin(\alpha_i) & 0 \\ \sin(\alpha_i) & \cos(\alpha_i) & 0 \\ 0 & 0 & 1 \end{bmatrix}. \quad (3.30)$$

Regarding the cross sectional area,  $A(\sigma_i)$  is defined as a function of  $\sigma_i$  for the whole TLMCD:

$$A(\sigma_i) \triangleq \begin{cases} A_h, & \forall \sigma_i \in [0, L_h/2) \\ A_v, & \forall \sigma_i \in [L_h/2, +\infty) \end{cases}. \quad (3.31)$$

### 3.4.2 Kinematics

To describe the time dependent fluid motion (or to say the fluid distribution within the columns), variables that measure the free surface position are needed. For conventional two-column TLCD, only one variable is needed to describe the flow condition within the columns, which is  $z$  in Section 3.3. As the number of vertical columns increases, more variables are required. Since the fluid is assumed to be incompressible, for a TLMCD with  $N$  elements, at least  $N-1$  variables are necessary to describe the fluid dynamics inside the TLMCD, here  $nc = N - 1$  is used for simplicity.

Assuming that the fluid in the  $i_{th}$  streamline accumulates to a length of  $\sigma_i = \zeta_i$ , then the total length of the streamline is from  $\sigma_i = 0$  to the free surface. In this case, the relative position of the free surface in the  $i_{th}$  vertical column with respect to that in steady state is  $z_i = \zeta_i - L_h/2 - L_v$ . To avoid confusion between the free surface motion and the platform heave motion,  $w_i$  is defined to replace the  $z_i$  used in Section 3.3. In terms of the direction, if the free surface level is higher than the one in steady state,  $w_i > 0$ , or vice versa. Finally, the generalized position vector required to describe the flow state is defined as

$$\mathbf{w} \triangleq [w_1, w_2, \dots, w_{nc}]^T. \quad (3.32)$$

The direct time derivative of Equation 3.32 results the speed of the fluid flow, which equals  $\dot{w}_i$  in the  $i_{th}$  vertical column. In the horizontal column, due to the mass conservation, the flow speed equals  $\frac{A_v}{A_h} \dot{w}_i$ . By adding the directions to the speed, the fluid velocity at any cross section (or to say point along the streamline) inside the TLMCD in the platform-fixed body frame can be derived as

$$\mathbf{v}_{t,i}^b(\sigma_i) = \frac{A_v \dot{w}_i}{A(\sigma_i)} \mathbf{R}_z(\alpha_i) \frac{d\bar{\mathbf{r}}^b}{d\sigma_i}(\sigma_i), \quad (3.33)$$

where  $\frac{d\bar{\mathbf{r}}^b}{d\sigma_i}(\sigma_i)$  is the unit vector of  $\frac{d\mathbf{r}^b}{d\sigma_i}(\sigma_i)$  which is defined as

$$\frac{d\bar{\mathbf{r}}^b}{d\sigma_i}(\sigma_i) \triangleq \frac{\frac{d\mathbf{r}^b}{d\sigma_i}(\sigma_i)}{\left\| \frac{d\mathbf{r}^b}{d\sigma_i}(\sigma_i) \right\|}. \quad (3.34)$$

When the TLMCD moves together with the floating wind turbine, which has the linear velocity  $\mathbf{v}_p$  and angular velocity  $\boldsymbol{\omega}_p$ , the velocity in the moving body frame of an arbitrary point at  $\sigma_i$  on the streamline becomes

$$\mathbf{v}_{t,i}^b = \mathbf{v}_p + \boldsymbol{\omega}_p \times \mathbf{R}_z(\alpha_i) \mathbf{r}^b(\sigma_i) + \frac{A_v \dot{\sigma}_i}{A(\sigma_i)} \mathbf{R}_z(\alpha_i) \frac{d\bar{\mathbf{r}}^b}{d\sigma_i}(\sigma_i), \quad (3.35)$$

where  $i = 1 \dots N$  represents the  $i_{th}$  column of the TLMCD.

The generalized coordinates of the free surface position are defined as

$$\mathbf{q} = [\mathbf{x}_p^\top, \boldsymbol{\Theta}_p^\top, \mathbf{w}^\top]^\top. \quad (3.36)$$

To link the body fixed velocities and the time differentiation of the coordinates, Equation 3.7 can be extended, which results in  $\mathbf{P}$  as the transformation matrix:

$$\mathbf{P}(\boldsymbol{\Theta}) \triangleq \begin{bmatrix} \mathbf{R}(\boldsymbol{\Theta})^\top & 0_{3 \times 3} & 0_{3 \times nc} \\ 0_{3 \times 3} & \mathbf{G}(\boldsymbol{\Theta}) & 0_{3 \times nc} \\ 0_{nc \times 3} & 0_{nc \times 3} & \mathbb{I}_{nc} \end{bmatrix} \in \mathbb{R}^{6+nc}. \quad (3.37)$$

Thus, the velocity of the TLMCD free surface in the initial coordinates can be expressed by using the translational and rotational velocities of the rigid body as

$$[\mathbf{v}_p^\top, \boldsymbol{\omega}_p^\top, \dot{\mathbf{w}}^\top]^\top = \mathbf{P} \dot{\mathbf{q}} \quad (3.38)$$

### 3.4.3 Potential and kinetic energy

The equations of motion describing the fluid flow are derived by using Lagrangian mechanics, which has been introduced in Chapter 1. This approach results in a set of Lagrange's equations described in initial coordinates, which are compatible with SLOW, if the generalized coordinates are defined in the same way. The basis of using Lagrangian mechanics is to establish the formula representing the potential and kinetic energy of the TLMCD.

When considering a very small volume of fluid  $d\mathcal{V}$  along the streamline, the volume of which can be calculated as  $d\mathcal{V} = A(\sigma_i) d\sigma_i$ , the corresponding kinetic energy  $dT$  is determined by the fluid velocities, which can be expressed in the body

frame:

$$dT = \frac{1}{2} \rho dV \left\| \mathbf{v}_{t,i}^b \right\|_2^2, \quad (3.39)$$

where  $dV$  represents an infinitesimally small volume of fluid inside the TLMCD, equal to  $A(\sigma_i)d\sigma_i$ . The vector norm  $\left\| \mathbf{v}_{t,i}^b \right\|_2$  is defined as

$$\left\| \mathbf{v}_{t,i}^b \right\|_2 = \left( \sum_{j=1}^n v_{t,ij}^b{}^2 \right)^{\frac{1}{2}}. \quad (3.40)$$

By integrating the kinetic energy of small fluid volumes along the streamlines, the total kinetic energy of the TLMCD can be obtained. As a result, the kinetic energy accumulates, yielding the total amount of kinetic energy  $T$  in the TLMCD system, which can be expressed as

$$\begin{aligned} T &= \sum_{i=1}^N \int_0^{\zeta_i} \frac{1}{2} \rho \left\| \mathbf{v}_{t,i} \right\|_2^2 A(\sigma_i) d\sigma_i \\ &= \frac{\rho}{2} \sum_{i=1}^N \int_0^{\zeta_i} \left\| \mathbf{v}_p + \boldsymbol{\omega}_p \times \mathbf{R}_z(\alpha_i) \mathbf{r}^b(\sigma_i) + \frac{A_v \dot{w}_i}{A(\sigma_i)} \mathbf{R}_z(\alpha_i) \frac{d\bar{\mathbf{r}}^b}{d\sigma_i}(\sigma_i) \right\|_2^2 A(\sigma_i) d\sigma_i \quad (3.41) \\ &= \frac{\rho}{2} \sum_{i=1}^N \int_0^{\zeta_i} \left\| \mathbf{v}_p - \tilde{\mathbf{S}}(\mathbf{R}_z(\alpha_i) \mathbf{r}^b(\sigma_i)) \boldsymbol{\omega}_p + \frac{A_v \dot{w}_i}{A(\sigma_i)} \mathbf{R}_z(\alpha_i) \frac{d\bar{\mathbf{r}}^b}{d\sigma_i}(\sigma_i) \right\|_2^2 A(\sigma_i) d\sigma_i \end{aligned}$$

where  $d\sigma_i$  is a differential length along the  $i_{\text{th}}$  streamline described by curvilinear coordinates. The geometry related parameter  $A(\sigma_i)$  describes the change in cross sectional area over the streamline. In the case of a TLMCD with uniform cross section, as shown in Figure 3.2, then  $A(\sigma_i > L_h/2) = A_v$ , otherwise,  $A(\sigma_i \leq L_h/2) = A_h$ .

To better understand the underlying components of the kinetic energy,  $T$  can be expanded into

$$\begin{aligned}
T = & \frac{1}{2} \underbrace{\left( \rho \sum_{i=1}^N \int_0^{\zeta_i} A(\sigma_i) d\sigma_i \right)}_{m_t} \|\mathbf{v}_p\|_2^2 \\
& + \frac{1}{2} \underbrace{\boldsymbol{\omega}_p^\top \left( -\rho \sum_{i=1}^N \int_0^{\zeta_i} A(\sigma_i) \tilde{\mathbf{S}}^2 (\mathbf{R}_z(\alpha_i) \mathbf{r}^b(\sigma_i)) d\sigma_i \right)}_{\mathbf{M}_\omega} \boldsymbol{\omega}_p \\
& + \underbrace{\boldsymbol{\omega}_p^\top \left( -\rho \sum_{i=1}^N \int_0^{\zeta_i} A(\sigma_i) \tilde{\mathbf{S}} (\mathbf{R}_z(\alpha_i) \mathbf{r}^b(\sigma_i)) d\sigma_i \right)}_{\mathbf{M}_{v\omega}} \mathbf{v}_p \\
& + \underbrace{\mathbf{v}_p^\top \left( \rho A_v \sum_{i=1}^N \int_0^{\zeta_i} \mathbf{R}_z(\alpha_i) \frac{d\mathbf{r}^b}{d\sigma_i} d\sigma_i \right)}_{\mathbf{M}_{vq}} \dot{w}_i \\
& + \underbrace{\boldsymbol{\omega}_p^\top \left( \rho A_v \sum_{i=1}^N \int_0^{\zeta_i} \tilde{\mathbf{S}} (\mathbf{R}_z(\alpha_i) \mathbf{r}^b(\sigma_i)) \mathbf{R}_z(\alpha_i) \frac{d\mathbf{r}^b}{d\sigma_i} d\sigma_i \right)}_{\mathbf{M}_{\omega q}} \dot{w}_i \\
& + \frac{1}{2} \underbrace{\left( \rho \sum_{i=1}^N \int_0^{\zeta_i} \frac{A_v^2}{A(\sigma_i)} d\sigma_i \right)}_{\mathbf{M}_q} \dot{w}_i^2
\end{aligned} \tag{3.42}$$

For convenience,  $T$  can also be written in matrix format as

$$T = \frac{1}{2} [\mathbf{v}_p^\top, \boldsymbol{\omega}_p^\top, \dot{\mathbf{w}}^\top] \mathbf{M}_{\text{NS}} [\mathbf{v}_p^\top, \boldsymbol{\omega}_p^\top, \dot{\mathbf{w}}^\top]^\top, \tag{3.43}$$

where  $\mathbf{M}_{\text{NS}}$  is the full inertia matrix with different components in inertial coordinates, defined as

$$\mathbf{M}_{\text{NS}}(\mathbf{w}) \triangleq \begin{bmatrix} m_t \mathbb{I}_3 & \mathbf{M}_{v\omega}(\mathbf{w}) & \mathbf{M}_{vq}(\mathbf{w}) \\ \mathbf{M}_{v\omega}^\top(\mathbf{w}) & \mathbf{M}_\omega(\mathbf{w}) & \mathbf{M}_{\omega q}(\mathbf{w}) \\ \mathbf{M}_{vq}^\top(\mathbf{w}) & \mathbf{M}_{\omega q}^\top(\mathbf{w}) & \mathbf{M}_q(\mathbf{w}) \end{bmatrix} \in \mathbb{R}^{6+nc}. \tag{3.44}$$

$\mathbf{M}_q$  defines the time dependent fluid mass distribution inside the TLMCD. The mass

and moment of inertia of the TLMCD as a rigid body are calculated by  $m_t$  and  $\mathbf{M}_\omega$ . The products of inertia, representing the cross-coupling between translational and rotational accelerations, are represented by  $\mathbf{M}_{v\omega}$ . The most important terms are  $\mathbf{M}_{vq}$  and  $\mathbf{M}_{\omega q}$ , which describe the coupling between the TLMCD and the platform. These terms are consistent with the conventional TLCD introduced in Section 3.3. Some of the analytical models neglect several terms that do not have a major impact on the overall dynamics, but significantly increase the computational effort. A comprehensive comparison and discussion on these terms is given in [30]. Based on this study,  $\mathbf{M}_\omega$  and  $\mathbf{M}_{v\omega}$  are neglected for the rest of the study.

As for the potential energy, assuming that the potential energy at the equilibrium position is zero, then the potential energy of an arbitrary volume of fluid  $d\mathcal{V}$  is

$$dV = g\rho h(\mathbf{r}^b, \mathbf{x}_p)d\mathcal{V} \quad (3.45)$$

where the function  $h(\mathbf{r}^b, \mathbf{x}_p)$  is the relative height with respect to the equilibrium position in the initial coordinates. It consists of two parts. On the one hand, the TLMCD moves as a rigid body in six DOFs which is described by  $[\mathbf{x}_p^\top, \boldsymbol{\Theta}^\top]^\top$ , so that the potential energy changes depending on the current position of the platform  $\mathbf{x}_p$ . On the other hand, the motion of the free surface changes the fluid distribution inside the TLMCD and thus changes the potential energy of the TLMCD, making it a function of  $\mathbf{r}^b$  and  $\boldsymbol{\Theta}$ . Since the potential energy only concerns the vertical position in the inertial coordinate, the unit vector in the direction of the z-axis  $\mathbf{z}$  is used to obtain the corresponding component of the position vector, which results in

$$h(\mathbf{r}^b, \mathbf{x}_p) = \mathbf{z}^\top (\mathbf{R}(\boldsymbol{\Theta})\mathbf{R}_z(\alpha_i)\mathbf{r}^b(\sigma_i) + \mathbf{x}_p). \quad (3.46)$$

Similar to kinetic energy, the potential energy can be summed up as follows:

$$\begin{aligned} V &= g\rho\mathbf{z}^\top (\mathbf{R}(\boldsymbol{\Theta})\mathbf{R}_z(\alpha_i)\mathbf{r}^b(\sigma_i) + \mathbf{x}_p) \sum_{i=1}^N \int_0^{\zeta_i} A(\sigma_i)d\sigma_i \\ &= g\rho\mathbf{z}^\top \mathbf{R}(\boldsymbol{\Theta}) \sum_{i=1}^N \int_0^{\zeta_i} A(\sigma_i)\mathbf{R}_z(\alpha_i)\mathbf{r}^b(\sigma_i)d(\sigma_i) + g\rho z_p m_t \end{aligned} \quad (3.47)$$

### 3.4.4 Non-conservative forces

The Lagrangian principle shows the law of conservation of energy, so the action and reaction forces between the components of the system do not need to be considered in the equations of motion. The only forces that enter the equation are the non-conservative forces, which represent the energy going into and out of the system. For a FOWT, there are two main types of energy transformations. On the one hand, energy enters the system from excitations such as wind, waves, and currents. On the other hand, energy is dissipated due to the fluid viscosity, energy radiation, or vortex shedding.

The external disturbance forces, as well as the viscous drag forces due to the wave, are exerted only on the FOWT. These forces are already taken into account by the SLOW model. The presence of the TLMCD does not affect this part. The additional forces introduced by the TLMCD are due to the energy dissipation, described by the damping terms in the equations of motion. As mentioned in Section 3.3, there are both linear and quadratic damping terms. How to model the linear damping has been given in Equation 3.20. Therefore, only the quadratic term is described here, denoted by  $Q$ .

As the fluid flows, friction exists between the moving fluid and the column wall, which converts part of the kinetic or potential energy into thermal energy. This conversion and loss of energy is known as the major head loss and is proportional to the square of fluid velocity. There is also some minor head loss caused by sudden pressure drops, e.g. at the junction point of the columns. In addition, energy dissipation occurs due to the local vortex shedding at sharp corners, turbulence at the free surface, etc. For the major head loss, the damping is proportional to the square of fluid speed (norm of the local velocity vector). Assume that the fluid speed in the horizontal arms is

$$\mathbf{v}_h \triangleq [v_{h,1} \quad v_{h,2} \quad \dots \quad v_{h,N}]^\top, \quad (3.48)$$

then the resulting damping forces in the body frame can be written as

$$\mathbf{F}_h(\dot{\mathbf{w}}) = \frac{1}{2} \rho A_h \eta |\mathbf{v}_h| \circ \mathbf{v}_h, \quad (3.49)$$

where  $\eta$  is a non-dimensional head loss coefficient. The symbol " $\circ$ " in the equation denotes the Hadamard product, which is the element-wise multiplication of two matrices <sup>†</sup>.

Similar to Equation 3.18, because of the continuity of mass inside the TLMCD, the fluid speed in the horizontal arm  $\mathbf{v}_h$  can be determined by the free surface position  $w_i$ , which is written as

$$\mathbf{v}_h = [\dot{w}_1 \quad \dot{w}_2 \quad \dots \quad \dot{w}_N]^\top \frac{A_v}{A_h}. \quad (3.50)$$

To simplify the expression, a transformation matrix  $\mathbf{P}_h$  is defined as a function of the cross sectional area ratio  $\frac{A_v}{A_h}$ :

$$\mathbf{P}_h = \bar{\mathbf{P}}_h \frac{A_v}{A_h} \quad (3.51)$$

with

$$\bar{\mathbf{P}}_h = \begin{bmatrix} 1 & & & \\ & \ddots & & \\ & & 1 & \\ -1 & \dots & -1 & \end{bmatrix} \in \mathbb{R}^{N \times nc}. \quad (3.52)$$

Then the fluid speed vector  $\mathbf{v}_h$  can be directly linked to the generalized coordinates of the TLMCD  $\mathbf{w}$ , which is written as

$$\mathbf{v}_h = \mathbf{P}_h \dot{\mathbf{w}} = \bar{\mathbf{P}}_h \frac{A_v}{A_h} \dot{\mathbf{w}}. \quad (3.53)$$

The matrix  $\bar{\mathbf{P}}_h$  has no direct physical meaning, but can be understood as a Jacobian matrix which relates the generalized TLMCD coordinates to the fluid speed in the vertical columns, which means

$$\bar{\mathbf{P}}_h \dot{\mathbf{w}} = [\dot{w}_1 \quad \dot{w}_2 \quad \dots \quad \dot{w}_N]^\top. \quad (3.54)$$

---

<sup>†</sup>For any matrices  $A$  and  $B$ , the Hadamard product  $A \circ B$  produces another matrix whose elements are obtained by multiplying the corresponding elements of  $A$  and  $B$ . For example, the  $(i, j)$ -th element of  $A \circ B$  is given by  $(A \circ B)_{ij} = A_{ij} \cdot B_{ij}$ .



Given the corresponding forces and velocities, the virtual power can be calculated by  $\mathbf{v}_h^\top \mathbf{F}_h$ . If we define the generalized forces as  $\mathbf{Q}$ , the virtual power can also be calculated by  $\dot{\mathbf{w}}^\top \mathbf{Q}$ , which means

$$\mathbf{v}_h^\top \mathbf{F}_h = \dot{\mathbf{w}}^\top \mathbf{Q}. \quad (3.55)$$

After knowing  $\mathbf{v}_h$ ,  $\mathbf{F}_h$  and  $\mathbf{w}$ , the generalized forces  $\mathbf{Q}$  can be derived as

$$\begin{aligned} \mathbf{Q} &= (\dot{\mathbf{w}}^\top)^{-1} (\mathbf{P}_h \dot{\mathbf{w}})^\top \mathbf{F}_h \\ &= \mathbf{P}_h^\top \mathbf{F}_h \\ &= \frac{1}{2} \rho A_h \eta \mathbf{P}_h^\top \left( |\mathbf{v}_h| \circ \mathbf{v}_h \right) \\ &= \frac{1}{2} \rho A_h \eta \mathbf{P}_h^\top \left( |\mathbf{P}_h \dot{\mathbf{w}}| \circ \mathbf{P}_h \dot{\mathbf{w}} \right) \in \mathbb{R}^{nc \times 1}. \end{aligned} \quad (3.56)$$

As can be seen,  $\mathbf{Q}$  is dependent on the cross sectional areas of the TLMCD, as well as the time varying free surface motion of the TLMCD  $\dot{\mathbf{w}}$ .

### 3.4.5 Equation of motion

After obtaining all the components of Equation 2.5, the equations of motion for the TLMCD can be derived. Since the potential energy in classical mechanical systems is independent of velocities, meaning  $\frac{\partial V}{\partial \dot{\mathbf{q}}}$  equals zero, Equation 2.5 can be simplified as

$$\frac{d}{dt} \frac{\partial T}{\partial \dot{\mathbf{q}}} - \frac{\partial T}{\partial \mathbf{q}} + \frac{\partial V}{\partial \mathbf{q}} = \boldsymbol{\tau}. \quad (3.57)$$

As a first step, the partial derivatives of  $T$  and  $V$  with respect to the generalized coordinate  $\mathbf{q}$ , defined in Equation 3.36, can be established. The results of the partial differentiation are detailed as follows:

$$\frac{\partial V}{\partial \mathbf{q}} = \begin{bmatrix} m_t g z \\ -g \rho \mathbf{G}^\top \tilde{\mathbf{S}} (\mathbf{R}^\top \mathbf{z}) \sum_{i=1}^N \int_0^{\zeta_i} A(\sigma_i) \mathbf{R}_z(\alpha_i) \mathbf{r}^b(\sigma_i) d(\sigma_i) \\ g \rho A_v \mathbf{z}^\top \mathbf{R}(\boldsymbol{\Theta}) (\mathbf{R}_z(\alpha_1) \mathbf{r}^b(\zeta_1) - \mathbf{R}_z(\alpha_N) \mathbf{r}^b(\zeta_N)) \\ \vdots \\ g \rho A_v \mathbf{z}^\top \mathbf{R}(\boldsymbol{\Theta}) (\mathbf{R}_z(\alpha_{nc}) \mathbf{r}^b(\zeta_{nc}) - \mathbf{R}_z(\alpha_N) \mathbf{r}^b(\zeta_N)) \end{bmatrix}, \quad (3.58)$$

$$\frac{\partial T}{\partial \mathbf{q}} = \begin{bmatrix} 0_{3 \times 1} \\ \frac{\partial(\mathbf{P}\dot{\mathbf{q}})^\top}{\partial \Theta} \mathbf{M}_{\text{NS}} \mathbf{P} \\ \frac{1}{2}(\mathbf{P}\dot{\mathbf{q}})^\top \frac{\partial \mathbf{M}_{\text{NS}}}{\partial w_i} \mathbf{P} \\ \vdots \\ \frac{1}{2}(\mathbf{P}\dot{\mathbf{q}})^\top \frac{\partial \mathbf{M}_{\text{NS}}}{\partial w_{nc}} \mathbf{P} \end{bmatrix} \dot{\mathbf{q}}, \quad (3.59)$$

where  $-\mathbf{G}^\top \tilde{\mathbf{S}}(\mathbf{R}^\top \mathbf{z})$  is resulted from  $\frac{\partial \mathbf{z}^\top \mathbf{R}}{\partial \Theta}$  [3, p. 287].

Based on this, the time differentiation of the partial derivative of  $T$  with respect to  $\dot{\mathbf{q}}$  can then be determined, which is expressed as

$$\frac{d}{dt} \left( \frac{\partial T}{\partial \dot{\mathbf{q}}} \right) = \mathbf{P}^\top \mathbf{M}_{\text{NS}} \mathbf{P} \ddot{\mathbf{q}} + \mathbf{P}^\top \mathbf{M}_{\text{NS}} \dot{\mathbf{P}} \dot{\mathbf{q}} + \mathbf{P}^\top \sum_{i=1}^{nc} \dot{w}_i \frac{\partial \mathbf{M}_{\text{NS}}}{\partial w_i} \mathbf{P} \dot{\mathbf{q}} + \dot{\mathbf{P}}^\top \mathbf{M}_{\text{NS}} \mathbf{P} \dot{\mathbf{q}}. \quad (3.60)$$

As already mentioned previously, since the excitation forces from the wind, wave, and current are captured by SLOW, the energy dissipation inside the TLMCD, introduced in Section 3.4.4, is the only non-conservative force. Finally, the equations of motion can be assembled and formulated as

$$\mathbf{P}^\top \underbrace{\begin{bmatrix} \mathbf{M}_{\text{ns}} & \mathbf{M}_{vq}(\mathbf{w}) \\ \mathbf{M}_{\omega q}(\mathbf{w}) & \mathbf{M}_q(\mathbf{w}) \end{bmatrix}}_{\mathbf{M}_{\text{NS}}} \mathbf{P} \ddot{\mathbf{q}} + \mathbf{C}_{\text{NS}} \dot{\mathbf{q}} + \underbrace{\begin{bmatrix} \mathbf{K}_{\text{ns}} \\ \mathbf{K}_t \end{bmatrix}}_{\mathbf{K}_{\text{NS}}} = \begin{bmatrix} \mathbf{0} \\ \mathbf{Q}(\dot{\mathbf{w}}) \end{bmatrix}, \quad (3.61)$$

with

$$\mathbf{M}_{\text{ns}} = \begin{bmatrix} m_t \mathbb{I}_3 & \mathbf{M}_{v\omega}(\mathbf{w}) \\ \mathbf{M}_{v\omega}^\top(\mathbf{w}) & \mathbf{M}_{\omega}(\mathbf{w}) \end{bmatrix}. \quad (3.62)$$

This equation has a form consistent with Equation 2.1, with  $\mathbf{M}_{\text{NS}}$ ,  $\mathbf{C}_{\text{NS}}$  and  $\mathbf{K}_{\text{NS}}$  being the generalized inertia matrix, Coriolis and centrifugal matrix and gravitational forces respectively. While the external generalized forces are written on

the right hand side. These terms can be determined by

$$\mathbf{C}_{\text{NS}} = \begin{bmatrix} 0_{3 \times 1} \\ \frac{\partial(\mathbf{P}\dot{\mathbf{q}})^\top}{\partial \Theta} \mathbf{M}_{\text{NS}} \mathbf{P} \\ \frac{1}{2}(\mathbf{P}\dot{\mathbf{q}})^\top \frac{\partial \mathbf{M}_{\text{NS}}}{\partial w_i} \mathbf{P} \\ \vdots \\ \frac{1}{2}(\mathbf{P}\dot{\mathbf{q}})^\top \frac{\partial \mathbf{M}_{\text{NS}}}{\partial w_{nc}} \mathbf{P} \end{bmatrix} + \mathbf{P}^\top \mathbf{M}_{\text{NS}} \dot{\mathbf{P}} + \mathbf{P}^\top \sum_{i=1}^{nc} \dot{w}_i \frac{\partial \mathbf{M}_{\text{NS}}}{\partial w_i} \mathbf{P} + \dot{\mathbf{P}}^\top \mathbf{M}_{\text{NS}} \mathbf{P} \quad (3.63)$$

$$\mathbf{K}_{\text{NS}} = \frac{\partial V}{\partial \mathbf{q}}. \quad (3.64)$$

As can be seen,  $\mathbf{M}_{\text{NS}}$  is the mass matrix which is introduced in Equation 3.44.  $\mathbf{K}_{\text{NS}}$  represents the restoring forces due to the stiffness which is determined by  $\frac{\partial V}{\partial \mathbf{q}}$ . Coriolis and centrifugal forces are represented by  $\mathbf{C}_{\text{NS}}$  which is determined by  $\frac{\partial T}{\partial \dot{\mathbf{q}}}$  and  $\frac{d}{dt} \left( \frac{\partial T}{\partial \dot{\mathbf{q}}} \right)$ . Since the total mass of the TLMCD only takes a small proportion of the total mass of the coupled TLMCD and FOWT system,  $\mathbf{C}_{\text{NS}}$  will not have a significant influence. Thus, this term is omitted in this work, which is also not considered in some classical analytical TLCD models, e.g. [28].

Equation 3.61 is derived under the assumption that the TLMCD moves as a rigid body with a predefined velocity  $[\mathbf{v}_p^\top, \boldsymbol{\omega}_p^\top]^\top$  in space, which is the same as the FOWT. This is only true if the TLMCD and the FOWT are considered as a whole system. Therefore, the inertia properties, the non-conservative forces due to the environmental excitations, as well as the damping effect must be added to the equation. These terms are already solved by SLOW in Section 3.2. So Equation 3.61 can be extended by combining the terms in Equation 3.15, which is written as

$$\begin{aligned} \mathbf{P}^\top \begin{bmatrix} \mathbf{M}_p + \mathbf{M}_{\text{ns}} & \mathbf{M}_{vq}(\mathbf{w}) \\ \mathbf{M}_{\omega q}(\mathbf{w}) & \mathbf{M}_q(\mathbf{w}) \end{bmatrix} \mathbf{P} \ddot{\mathbf{q}} + \begin{bmatrix} \mathbf{C}_p & \mathbf{0} \\ \mathbf{0} & \mathbf{0} \end{bmatrix} \dot{\mathbf{q}} + \begin{bmatrix} \mathbf{K}_p \\ \mathbf{0} \end{bmatrix} \mathbf{q} + \begin{bmatrix} \mathbf{K}_{\text{ns}} \\ \mathbf{K}_t \end{bmatrix} \\ = \begin{bmatrix} \boldsymbol{\tau}_p(\mathbf{v}_p, \boldsymbol{\omega}_p) \\ \mathbf{Q}(\dot{\mathbf{w}}) \end{bmatrix}, \end{aligned} \quad (3.65)$$

where  $\mathbf{M}_p$ ,  $\mathbf{C}_p$ ,  $\mathbf{K}_p$  and  $\boldsymbol{\tau}_p$  are purely platform related parameters.

Compared to the equations of motion for the platform-only system, the matrices  $\mathbf{M}_{ns}$  and  $\mathbf{K}_{ns}$  can be considered as additional mass, inertia, and stiffness, which contribute to the system dynamics of the FOWT. This is similar to the case when the platform has changed its mass or mass distribution.

For the TLMCD, there should be forces coming from the platform that cause the TLMCD to move along with the platform. According to Newton's Third Law, there should be an equal amount of reaction forces exerted on the platform to hold the TLMCD. When the platform and the TLMCD are considered as one single system, represented by generalized coordinates, these internal forces are mathematically cancelled out when deriving the equations of motion. Physically, this implies that the internal forces do not increase or decrease the energy of the whole system. This is in line with Equation 3.15, where all the internal forces are mathematically eliminated by multiplying the Jacobian matrices.

Nevertheless, the internal forces, which keep the TLMCD moving along with the platform, do exist. These forces lead to the coupling between the platform states and the TLMCD states, described by  $\mathbf{M}_{vq}$ ,  $\mathbf{M}_{\omega q}$  and  $\mathbf{K}_{ns}$ :

$$\mathbf{M}_{vq}[:, j](\mathbf{w}) \triangleq \rho A_v \sum_{i=1}^N \int_0^{\zeta_i} \mathbf{R}_z(\alpha_i) \frac{d\mathbf{r}^b}{d\sigma_i} d\sigma_i \bar{\mathbf{P}}_h[i, j] \in \mathbb{R}^{3 \times 1}, \quad (3.66)$$

$$\mathbf{M}_{\omega q}[:, j](\mathbf{w}) \triangleq \rho A_v \sum_{i=1}^N \int_0^{\zeta_i} \tilde{\mathbf{S}}(\mathbf{R}_z(\alpha_i) \mathbf{r}^b) \mathbf{R}_z(\alpha_i) \frac{d\mathbf{r}^b}{d\sigma_i} d\sigma_i \bar{\mathbf{P}}_h[i, j] \in \mathbb{R}^{3 \times 1}, \quad (3.67)$$

$$\mathbf{K}_{ns} \triangleq g \begin{bmatrix} m_t \mathbf{z} \\ -\rho \mathbf{G}^\top \tilde{\mathbf{S}}(\mathbf{R}^\top \mathbf{z}) \sum_{i=1}^N \int_0^{\zeta_i} A(\sigma_i) \mathbf{R}_z(\alpha_i) \mathbf{r}^b(\sigma_i) d\sigma_i \end{bmatrix} \in \mathbb{R}^{6 \times 1} \quad . \quad (3.68)$$

Here  $j = 1 \dots nc$  means that  $\mathbf{M}_{vq}$  and  $\mathbf{M}_{\omega q}$  have the size of  $3 \times nc$  respectively. The mass term  $\mathbf{M}_q$  and the stiffness term  $\mathbf{K}_t$  are purely TLMCD related. They are the essential key parameters for the equation of motion for the TLMCD, which are

expressed as

$$\mathbf{M}_q(\mathbf{w}) \triangleq \rho A_v \left( \bar{\mathbf{P}}_h^\top \bar{\mathbf{P}}_h \frac{L_h}{2} (\gamma - 1) + \bar{\mathbf{P}}_h^\top \begin{bmatrix} \zeta_1 & & \\ & \ddots & \\ & & \zeta_N \end{bmatrix} \bar{\mathbf{P}}_h \right) \in \mathbb{R}^{nc} \quad (3.69)$$

$$\mathbf{K}_t \triangleq g \begin{bmatrix} \rho A_v \mathbf{z}^\top \mathbf{R}(\boldsymbol{\Theta}) (\mathbf{R}_z(\alpha_1) \mathbf{r}^b(\zeta_1) - \mathbf{R}_z(\alpha_N) \mathbf{r}^b(\zeta_N)) \\ \vdots \\ \rho A_v \mathbf{z}^\top \mathbf{R}(\boldsymbol{\Theta}) (\mathbf{R}_z(\alpha_{nc}) \mathbf{r}^b(\zeta_{nc}) - \mathbf{R}_z(\alpha_N) \mathbf{r}^b(\zeta_N)) \end{bmatrix} \in \mathbb{R}^{nc \times 1}. \quad (3.70)$$

To better understand the physical implications of these terms, their correlation to the classical model in [28, p. 265] is helpful. Specifically,  $\mathbf{M}_{vq}[2, 1]$  denotes an equivalent physical coupling to  $a_{\tau 2}$ , while  $\mathbf{M}_{\omega q}[1, 1]$  and  $\mathbf{M}_{\omega q}[3, 1]$  correspond respectively to  $a_{\tau 4}$  and  $a_{\tau 6}$ . Similarly, the connection between  $\mathbf{M}_q$  and  $a_{\tau \tau}$  is notable, whereas  $\mathbf{K}_t$  contains  $c_{\tau 4}$  and  $c_{\tau \tau}$ . When these terms are further simplified and linearized, they will yield an expression equivalent to that in [28, p.265], as detailed in the following Section 3.5.

Besides the mass and stiffness terms, there is additional damping due to the energy dissipation within the TLMCD. The damping term for the TLMCD is described by  $\mathbf{Q}(\dot{\mathbf{w}})$  and given in detail as

$$\mathbf{Q}(\dot{\mathbf{w}}) = \frac{1}{2} \rho A_h \eta \gamma^3 \bar{\mathbf{P}}_h^\top \left( |\bar{\mathbf{P}}_h \dot{\mathbf{w}}| \circ (\bar{\mathbf{P}}_h \dot{\mathbf{w}}) \right) \in \mathbb{R}^{nc \times 1} \quad (3.71)$$

Again, the above derivation is originally developed in [3]<sup>†</sup>, the differences with this study are the coordinates and the modeling of the FOWT. More specifically, a right-handed Cartesian coordinate system with the z-axis pointing upwards is used to describe the floating platform, and the dynamics of the platform are solved using Newton-Euler equations. This difference may lead to some different signs in the equations.

---

<sup>†</sup>Note that the expression of Equation 3.69 in the appendix of [3] contains typing errors. Therefore, the expression may look different here.

## 3.5 Equations of Motion of a TLMCD with Uniform Cross Sections

Although Section 3.4.5 provides the thorough formulation of the TLMCD dynamics, the equations are complicated to implement and to linearize. Since the kinematics are defined for a small volume of fluid of the TLMCD, integration along the streamline is required to obtain the parameters for the TLMCD, which also significantly reduces the computational efficiency. Considering that the cross section of most conventional TLCDs has regular shapes and is uniform along the columns, the integration can be calculated analytically, thus simplifying the Equation 3.66-3.71.

### 3.5.1 Simplified expression

Assuming that both the vertical columns and horizontal columns of the TLMCD have uniform cross sections, the integration term in Equation 3.66-3.70 can be simplified as a multiplication, which can be carried out analytically. The essential coefficients to form the equations of the motion for a TLMCD can be written more compactly:

$$\begin{aligned} \mathbf{M}_q(\mathbf{w}) = & \rho A_v \left( L_v + \frac{L_h \gamma}{2} + w_n \right) \mathbf{J}_{nc} + \\ & \rho A_v \text{diag} \left( L_v + \frac{L_h \gamma}{2} + w_1, \dots, L_v + \frac{L_h \gamma}{2} + w_{nc} \right) \in \mathbb{R}^{nc}, \end{aligned} \quad (3.72)$$

$$\mathbf{M}_{vq}[:, i](\mathbf{w}) = \rho A_v \begin{bmatrix} \frac{L_h}{2} (\cos(\alpha_i) - \cos(\alpha_N)) \\ \frac{L_h}{2} (\sin(\alpha_i) - \sin(\alpha_N)) \\ w_i - w_N \end{bmatrix} \in \mathbb{R}^{3 \times 1} \quad (3.73)$$

$$\mathbf{M}_{\omega q}[:, i](\mathbf{w}) = \rho A_v \frac{L_h}{2} \begin{bmatrix} \sin(\alpha_i)(L_v + w_i - e) - \sin(\alpha_N)(L_v + w_N - e) \\ -\cos(\alpha_i)(L_v + w_i - e) + \cos(\alpha_N)(L_v + w_N - e) \\ 0 \end{bmatrix} \in \mathbb{R}^{3 \times 1} \quad (3.74)$$

$$\mathbf{K}_{\text{ns}}[4:6, 1](\mathbf{q}) = -g\rho \begin{bmatrix} -\sin(\beta) \\ \cos(\beta) \sin(\varphi) \\ \cos(\beta) \cos(\varphi) \end{bmatrix} \times \begin{bmatrix} (A_h(\frac{L_h}{2})^2/2 + A_v(\frac{L_h}{2})L_v) \sum_{i=1}^N \cos(\alpha_i) + A_v \frac{L_h}{2} \sum_{i=1}^N w_i \cos(\alpha_i) \\ (A_h(\frac{L_h}{2})^2/2 + A_v(\frac{L_h}{2})L_v) \sum_{i=1}^N \sin(\alpha_i) + A_v \frac{L_h}{2} \sum_{i=1}^N w_i \sin(\alpha_i) \\ (A_h \frac{L_h}{2} e + A_v L_v e + A_v \frac{L_v^2}{2}) \cdot N + \frac{A_v}{2} (w_1^2 + w_2^2 + \dots + w_N^2) \end{bmatrix} \in \mathbb{R}^{3 \times 1} \quad (3.75)$$

$$\mathbf{K}_t[i, 1](\mathbf{q}) = g\rho A_v \begin{bmatrix} -\sin(\beta) \\ \cos(\beta) \sin(\varphi) \\ \cos(\beta) \cos(\varphi) \end{bmatrix} \circ \begin{bmatrix} (\cos(\alpha_i) - \cos(\alpha_N)) \frac{L_h}{2} \\ (\sin(\alpha_i) - \sin(\alpha_N)) \frac{L_h}{2} \\ w_i + w_1 + \dots + w_{nc} \end{bmatrix} \in \mathbb{R}^{1 \times 1} \quad (3.76)$$

where  $i = 1 \dots nc$  in the above equations and  $\mathbf{J}_{nc}$  is a  $nc \times nc$  matrix of ones. In scenarios involving two vertical columns, i.e., when  $nc = 1$ , these equations result in a formulation equivalent to that commonly used for conventional TLCs. The difference lies in the defined coordinate system.

### 3.5.2 Linearization

Given the simplified formulation of the equations of motion, it is possible to linearize the model assuming a fixed free surface position. When  $w_i = 0$ , the mass and stiffness terms become:

$$\mathbf{M}_q(0) = \rho A_v \left( L_v + \frac{L_h \gamma}{2} \right) \begin{bmatrix} 2 & 1 & \dots & 1 \\ 1 & 2 & \ddots & \vdots \\ \vdots & \ddots & \ddots & 1 \\ 1 & \dots & 1 & 2 \end{bmatrix} \in \mathbb{R}^{nc} \quad (3.77)$$

$$\mathbf{M}_{vq}[:, i](0) = \rho A_v \frac{L_h}{2} \begin{bmatrix} \cos(\alpha_i) - \cos(\alpha_N) \\ \sin(\alpha_i) - \sin(\alpha_N) \\ 0 \end{bmatrix}, \quad i = 1 \dots nc \quad (3.78)$$

$$\mathbf{M}_{\omega q}[:, i](0) = \rho A_v \frac{L_h}{2} (L_v - e) \begin{bmatrix} \sin(\alpha_i) - \sin(\alpha_N) \\ -\cos(\alpha_i) + \cos(\alpha_N) \\ 0 \end{bmatrix}, \quad i = 1 \dots nc \quad (3.79)$$

Based on the restoring forces, the stiffness matrix can be obtained when it is differentiated by the generalized coordinates of the TLMCD, i.e.  $\mathbf{q} = [\mathbf{x}_p^\top, \boldsymbol{\Theta}_p^\top, \mathbf{w}^\top]^\top$ :

$$\begin{aligned} \mathbf{K}_{ns,l}[i, j] &= \frac{\partial \mathbf{K}_{ns}[i, 1]}{\partial q_j} \\ \mathbf{K}_{t,l}[i, j] &= \frac{\partial \mathbf{K}_t[i, 1]}{\partial q_j} \end{aligned} \quad (3.80)$$

Then the linearized total restoring forces due to the TLMCD can be written as

$$\begin{bmatrix} \mathbf{K}_{ns}(\mathbf{q}) \\ \mathbf{K}_t(\mathbf{q}) \end{bmatrix} = \begin{bmatrix} \mathbf{K}_{ns,l}(0) \\ \mathbf{K}_{t,l}(0) \end{bmatrix} \cdot \mathbf{q}. \quad (3.81)$$

For simplicity, the stiffness matrix in Equation 3.81 is split into several elements:

$$\begin{bmatrix} \mathbf{K}_{ns,l}(0) \\ \mathbf{K}_{t,l}(0) \end{bmatrix} \triangleq \begin{bmatrix} \mathbf{0}_{3 \times 3} & \mathbf{0}_{3 \times 3} & \mathbf{0}_{3 \times nc} \\ \mathbf{0}_{3 \times 3} & \mathbf{K}_{ns,l22} & \mathbf{K}_{ns,l23} \\ \mathbf{0}_{nc \times 3} & \mathbf{K}_{t,l32} & \mathbf{K}_{t,l33} \end{bmatrix} \in \mathbb{R}^{(6+nc) \times (6+nc)} \quad (3.82)$$

$$\mathbf{K}_{ns,l22}(0) = -g\rho \left( A_h \frac{L_h}{2} e + A_v L_v e + A_v \frac{L_v^2}{2} \right) \cdot N \begin{bmatrix} 1 & 0 & 0 \\ 0 & 1 & 0 \\ 0 & 0 & 0 \end{bmatrix} \in \mathbb{R}^3 \quad (3.83)$$

$$\mathbf{K}_{t,l33}(0) = g\rho A_v \begin{bmatrix} 2 & 1 & \dots & 1 \\ 1 & 2 & \ddots & \vdots \\ \vdots & \ddots & \ddots & 1 \\ 1 & \dots & 1 & 2 \end{bmatrix} \in \mathbb{R}^{nc} \quad (3.84)$$



$$\mathbf{K}_{t,l32}(0) = g\rho A_v \frac{L_h}{2} \begin{bmatrix} \sin(\alpha_1) - \sin(\alpha_N) & -\cos(\alpha_1) + \cos(\alpha_N) & 0 \\ \sin(\alpha_2) - \sin(\alpha_N) & -\cos(\alpha_2) + \cos(\alpha_N) & 0 \\ \vdots & \vdots & \vdots \\ \sin(\alpha_{nc}) - \sin(\alpha_N) & -\cos(\alpha_{nc}) + \cos(\alpha_N) & 0 \end{bmatrix} \in \mathbb{R}^{nc \times 3} \quad (3.85)$$

$$\mathbf{K}_{ns,l23}(0) = g\rho A_v \frac{L_h}{2} \begin{bmatrix} \sin(\alpha_1) - \sin(\alpha_N) & \sin(\alpha_2) - \sin(\alpha_N) & \cdots & \sin(\alpha_{nc}) - \sin(\alpha_N) \\ -\cos(\alpha_1) + \cos(\alpha_N) & -\cos(\alpha_2) + \cos(\alpha_N) & \cdots & -\cos(\alpha_{nc}) + \cos(\alpha_N) \\ 0 & 0 & \cdots & 0 \end{bmatrix} \in \mathbb{R}^{3 \times nc} \quad (3.86)$$

It is worth mentioning that  $\mathbf{K}_{t,l32}(0) = \mathbf{K}_{ns,l23}(0)^\top$ .

As for the generalized force due to the damping forces  $\mathbf{Q}(\dot{\mathbf{w}})$ , we assume a linear damping coefficient  $d_1$  [kg/s], which is the same as in Equation 3.20. The generalized  $\mathbf{Q}_l(\dot{\mathbf{w}})$  is given by

$$\begin{aligned} \mathbf{Q}_l(\dot{\mathbf{w}}) &= \mathbf{P}_h^\top \cdot d_1 \mathbf{v}_h \\ &= d_1 \gamma^2 \bar{\mathbf{P}}_h^\top \bar{\mathbf{P}}_h \dot{\mathbf{w}} \\ &= d_1 \gamma^2 \begin{bmatrix} 2 & 1 & \cdots & 1 \\ 1 & 2 & \ddots & \vdots \\ \vdots & \ddots & \ddots & 1 \\ 1 & \cdots & 1 & 2 \end{bmatrix} \dot{\mathbf{w}} \in \mathbb{R}^{nc \times 1} \end{aligned} \quad (3.87)$$

## 3.6 Coupling with FOWT Numerical Model

Both explicit and implicit methods are used for the coupling. With the explicit method, the required states of the platform should be provided for the TLMCD module. Based on this, the corresponding stabilizing forces and moments can be calculated and fed back to the FOWT numerical model. The implicit method includes the TLMCD states in the equations of motion of the FOWT and then solves the coupled system of FOWT and TLMCD differential equations. This section first

explains the two coupling methods and then compares the simulation results.

### 3.6.1 Explicit coupling

In this work, the explicit coupling is implemented in Simulink. Figure 3.3 shows the block diagram of the coupling, where  $x_p$  and  $\Theta_p$  represent the position and orientation of the platform,  $\ddot{x}_p$  and  $\ddot{\Theta}_p$  are the corresponding accelerations in the inertial coordinate.

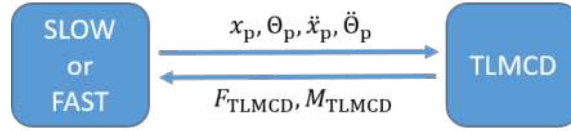


**Figure 3.3:** Block diagram showing the signal exchange between the FOWT and the TLMCD of the explicit coupling.

The additional forces and moments added to the platform due to the presence of the TLMCD are  $\mathbf{F}_{\text{TLMCD}}$  and  $\mathbf{M}_{\text{TLMCD}}$ , which are calculated using

$$\begin{bmatrix} \mathbf{F}_{\text{TLMCD}} \\ \mathbf{M}_{\text{TLMCD}} \end{bmatrix} = - \begin{bmatrix} \mathbf{R}\mathbf{M}_{vq}\ddot{\mathbf{w}} \\ \mathbf{G}^\top \mathbf{M}_{\omega q}\ddot{\mathbf{w}} \end{bmatrix} - \mathbf{K}_{\text{ns}}. \quad (3.88)$$

This approach aligns with the methodology presented in [28, p. 266]. For instance, concerning the roll direction,  $\mathbf{K}_{\text{ns}}[4, 1]$  denotes  $c_{4\tau}\tau$ , while  $\mathbf{M}_{\omega q}\ddot{\mathbf{w}}$  encompasses  $a_{4\tau}\ddot{\tau}$ . In the case of small-angle motions, the transformation matrices  $R$  and  $G$  are neglected, reflecting the conditions in [28].

With the explicit coupling method, the differential equations of the FOWT and the TLMCD are set up separately in their own block. The action and reaction forces between the platform and the TLMCD are treated as external forces for both of the systems. Therefore, these forces should be written on the right hand side of the platform equation of motion. At each time step, the platform motion and acceleration in 6 DOFs are forwarded to the TLMCD block. These motions induce forces on the TLMCD that keep the TLMCD moving along with the platform. After solving the differential equations of the TLMCD, the change of states is known

and the stabilizing forces can be calculated and sent back to the FOWT model. The stabilizing forces are then added as additional excitation forces acting on the platform, next to the wave excitation forces. The coupling principles in both SLOW and OpenFAST are similar, but the point at which the TLMCD forces are added differs for practical reasons. In SLOW, the forces are added at the center of gravity of the platform, whereas in OpenFAST the reference point is at the origin of the platform fixed frame of reference.

Because of this difference, the resulting TLMCD forces are processed differently in the two numerical models during the implementation:

- **SLOW**

The resulting stabilizing forces given by Equation 3.88 have a reference point at the origin of the body frame of the TLMCD, as illustrated in Figure 3.2. Since SLOW formulates the equations of motion for each body around its center of gravity, the moments need to be transformed from the center of flotation at sea water level to the center of gravity of the platform. The transfer matrix  $\mathbf{H}(\mathbf{r}_g)$  [5] can be used for this purpose:

$$\mathbf{H}(\mathbf{r}_g) = \begin{bmatrix} \mathbb{I}_{3 \times 3} & \tilde{\mathbf{S}}^\top(\mathbf{r}_g) \\ \mathbf{0}_{3 \times 3} & \mathbb{I}_{3 \times 3} \end{bmatrix}, \quad (3.89)$$

where  $\mathbf{r}_g$  is the position vector of the platform's center of gravity, expressed in the body fixed reference frame. Note that  $\mathbf{H}(\mathbf{r}_g)$  has the following characteristic:

$$\mathbf{H}(\mathbf{r}_g)^{-\top} = \begin{bmatrix} \mathbb{I}_{3 \times 3} & \mathbf{0}_{3 \times 3} \\ \tilde{\mathbf{S}}(\mathbf{r}_g) & \mathbb{I}_{3 \times 3} \end{bmatrix}. \quad (3.90)$$

The forces added to SLOW are expressed as

$$\begin{bmatrix} \mathbf{F}_{\text{TLMCD}} \\ \mathbf{M}_{\text{TLMCD,g}} \end{bmatrix} = \mathbf{H}(\mathbf{r}_g)^{-\top} \begin{bmatrix} \mathbf{F}_{\text{TLMCD}} \\ \mathbf{M}_{\text{TLMCD,0}} \end{bmatrix} \quad (3.91)$$

- **OpenFAST**

Within OpenFAST, the TLMCD force vector is added to the force output of HydroDyn, since all the forces exerted on the platform are summed up there

and later forwarded to the ElastoDyn input subroutine. The joint is defined at the WAMIT reference point, i.e. the center of flotation in this work.

There are several ways to introduce additional forces into OpenFAST. Considering the potential that the TLMCD can be active and thus becomes an actuator, the implementation in Simulink is control oriented. The additional TLMCD related forces are added next to the control inputs. The standardized control inputs of OpenFAST include generator torque, blade pitch, turbine yaw position, etc.

Explicit coupling is easier to implement and it also preserves the equations of motion of the FOWT system, but it has several disadvantages. The state variable, as well as the corresponding stabilizing forces of the TLMCD, are always found one time step later. If the system is very stiff and has very high frequency responses, numerical instability may occur. This is not the case for semi-submersible platforms, which have relatively low frequency motions, but could be a problem for tension leg platforms. Another disadvantage is related to the system linearization. Since the differential equations of the platform and the TLMCD are set up separately, linearization of the entire coupled system is not possible. Therefore, when it comes to control design where a linear model is needed, implicit coupling is necessary.

### 3.6.2 Implicit coupling

For a TLMCD with arbitrarily varying cross section, the equations of motion are complex. It is not suitable for linearizing the coupled system because it requires the integral along the streamline at each time step. Therefore, the implicit coupling is implemented only for TLMCDs with uniform cross sections. The FOWT numerical model used is SLOW. Unlike the explicit coupling, where the FOWT model remains almost unchanged (except for the additional external loads from the TLMCD), the implicit coupling requires a modification of the system states, as well as an update of the equations of motion.

Figure 3.4, illustrates how various bodies of the FOWT are interconnected, with the ellipses representing the rigid or flexible bodies and the yellow dots representing the joints that connect the bodies. Without a TLMCD, the MBS topology of a FOWT corresponds to serial chains which has open loop mechanisms. Each body

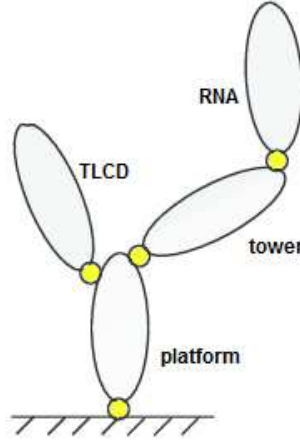


**Figure 3.4:** Structural topology of the coupled MBS system [40], illustrating the connections between each body.

is connected to a preceding body and it becomes basis of the next one. Note that the preceding body of the platform is the ground and the Rotor Nacelle Assembly (RNA) has a free end. By coupling to a TLMCD, the MBS is turned into a tree structure, with the floating platform acting as the base. Since the presence of the TLMCD does not affect the branch connecting the tower and the RNA, the coupling method described in this section only shows the interaction between the platform and the TLMCD. To reduce the size of the equations, the example shown here has three vertical columns.

According to Section 3.1, if the platform yaw motion is omitted, the generalized coordinates in  $\mathbf{q}_s$  for a platform in reduced order form are

$$\mathbf{q}_s = [x_p, y_p, z_p, \varphi_p, \beta_p]^\top, \quad (3.92)$$

with the motion states being platform surge  $x_p$ , sway  $y_p$ , heave  $z_p$ , roll  $\varphi_p$  and pitch  $\beta_p$ , respectively. The global Newton-Euler equation can be written as

$$\mathbf{M}_s(\mathbf{q}_s)\ddot{\mathbf{q}}_s + \mathbf{C}_s(\dot{\mathbf{q}}_s, \mathbf{q}_s)\dot{\mathbf{q}}_s = \boldsymbol{\tau}_s, \quad (3.93)$$

with the generalized mass matrix  $\mathbf{M}_s \in \mathbf{R}^{5 \times 5}$ , the Coriolis and centrifugal forces  $\mathbf{C}_s(\dot{\mathbf{q}}_s, \mathbf{q}_s)\dot{\mathbf{q}}_s \in \mathbf{R}^{5 \times 1}$  and the applied forces  $\boldsymbol{\tau}_s \in \mathbf{R}^{5 \times 1}$ .

For the coupled FOWT and TLMCD system, additional DOFs of the TLMCD  $\mathbf{w}$  need to be introduced, the generalized coordinates become

$$\mathbf{q}_w = [x_p, y_p, z_p, \varphi_p, \beta_p, w_1, w_2]^\top, \quad (3.94)$$

and the corresponding global Newton-Euler equation of the coupled system can be written as

$$\begin{bmatrix} \mathbf{M}_s(\mathbf{q}_s) & \mathbf{R}\mathbf{M}_{vq} \\ \mathbf{M}_{vq}^\top \mathbf{R}^\top & \mathbf{J}_q^\top \mathbf{G}^\top \mathbf{M}_{\omega q} \\ \mathbf{M}_{\omega q}^\top \mathbf{G} \mathbf{J}_q & \mathbf{M}_q \end{bmatrix} \ddot{\mathbf{q}}_w + \begin{bmatrix} \mathbf{C}_s(\mathbf{q}_s, \dot{\mathbf{q}}_s) \dot{\mathbf{q}}_s \\ \mathbf{0}_{nc \times 1} \end{bmatrix} = \begin{bmatrix} \boldsymbol{\tau}_s \\ \mathbf{0}_{nc \times 1} \end{bmatrix} + \begin{bmatrix} -\mathbf{K}_{ns}(1:3) \\ -\mathbf{J}_q^\top \mathbf{K}_{ns}(4:6) \\ -\mathbf{K}_t \end{bmatrix} + \begin{bmatrix} \mathbf{0}_{5 \times 1} \\ \mathbf{Q}(\dot{\mathbf{w}}) \end{bmatrix}, \quad (3.95)$$

where  $\mathbf{M}_{vq}$ ,  $\mathbf{M}_{\omega q}$ ,  $\mathbf{M}_q$ ,  $\mathbf{K}_{ns}$  and  $\mathbf{K}_t$  are given in Section 3.4.5, and are linearized in Section 3.5.2. Since the platform yaw DOF is omitted, the Jacobian matrix  $\mathbf{J}_q$  is necessary, which has the following form:

$$\mathbf{J}_q = \begin{bmatrix} 1 & 0 \\ 0 & 1 \\ 0 & 0 \end{bmatrix}. \quad (3.96)$$

### 3.6.3 Comparison between different models

A total of four coupled models are evaluated and compared. Two of these models are explicitly coupled and are implemented as an additional block next to the FOWT system in Simulink. The main difference between these two models lies in the formulation of the TLMCD. Specifically, the nonlinear model is based on Section 3.4, while the linear model results from the linearization process discussed in Section 3.5. The remaining two implicitly coupled models have an extended generalized system coordinate and use a linear TLMCD. In the case of coupling with the nonlinear FOWT model, Equation 3.95 is used to modify the S-function of the FOWT model. The

fully linearized coupled model uses a state-space representation, which is convenient for modal analysis and control design. To assess the performance of these models, the response to an Extreme Operating Gust (EOG) without waves is simulated and the results are presented in Figure 3.5.

Overall, the four models behave similarly, especially in terms of the transient response resulting from the sudden change in aerodynamic loads during the short period of the gust. However, the model with linear FOWT model yields slightly lower maximum rotor speed and blade pitch, due to the linearization of the aerodynamics. Notably, there are differences in the platform motions and the TLMCD free surface after the gust period. The nonlinear TLMCD model shows larger oscillations, indicated by higher response amplitudes, while the remaining linear TLMCD models have similar response amplitudes. In addition, there is a phase shift over time between the explicitly coupled models and the implicitly coupled model due to from the coupled dynamics. Although this shift cannot be eliminated, it is not apparent when the dynamic responses are dominated by large external excitations such as wind and waves.

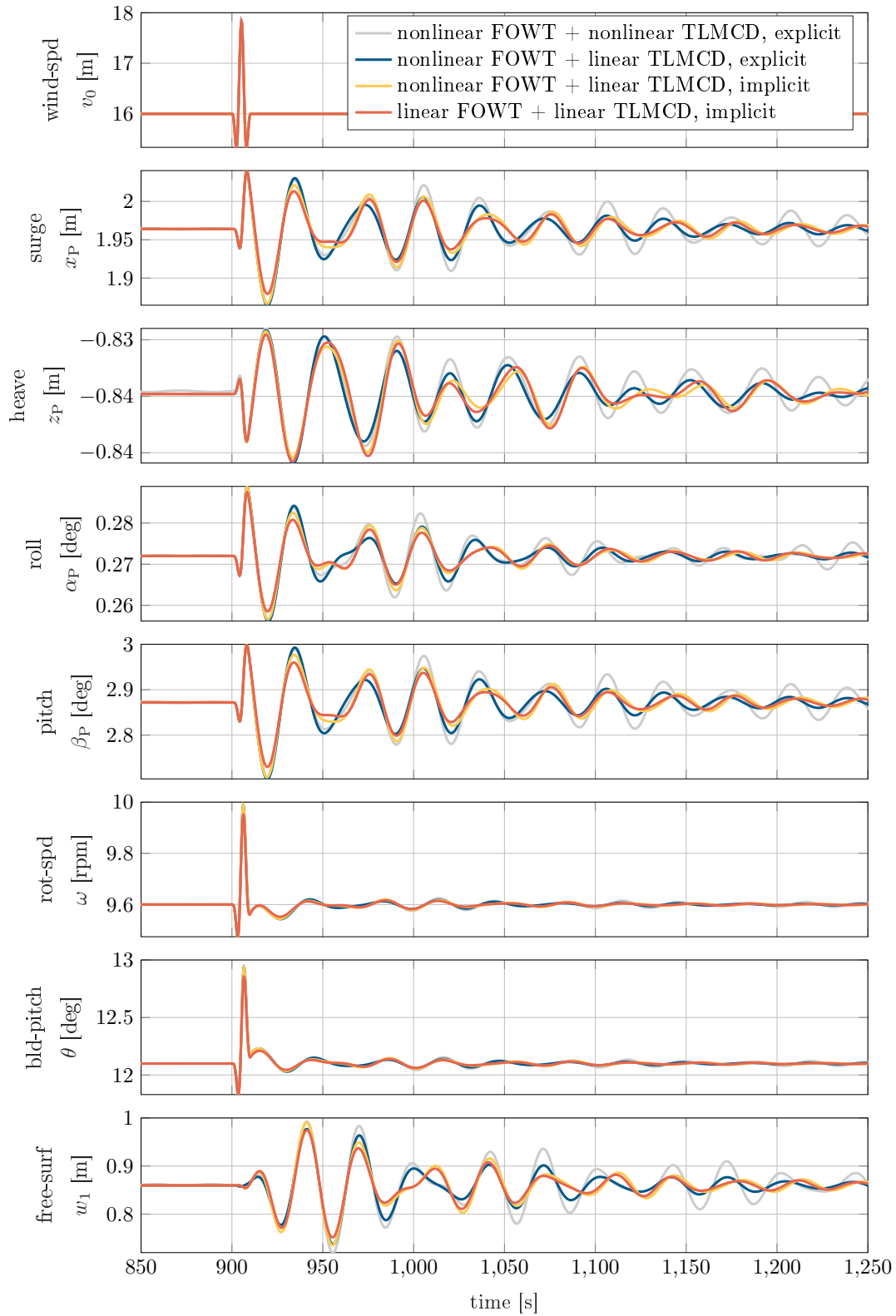
In summary, it is more accurate to use a nonlinear model, but in applications where a linear model is preferred, such as control design, a linearized model can still give reasonable predictions.

### 3.6.4 Code-to-code verification

This section shows the performance of the developed numerical tool. The simulation is carried out under turbulent wind condition with a mean speed of 16 m/s and irregular waves with an incident angle of 30 deg. The comparison between SLOW and OpenFAST is shown both in uncoupled mode and in explicitly coupled mode with the TLMCD.

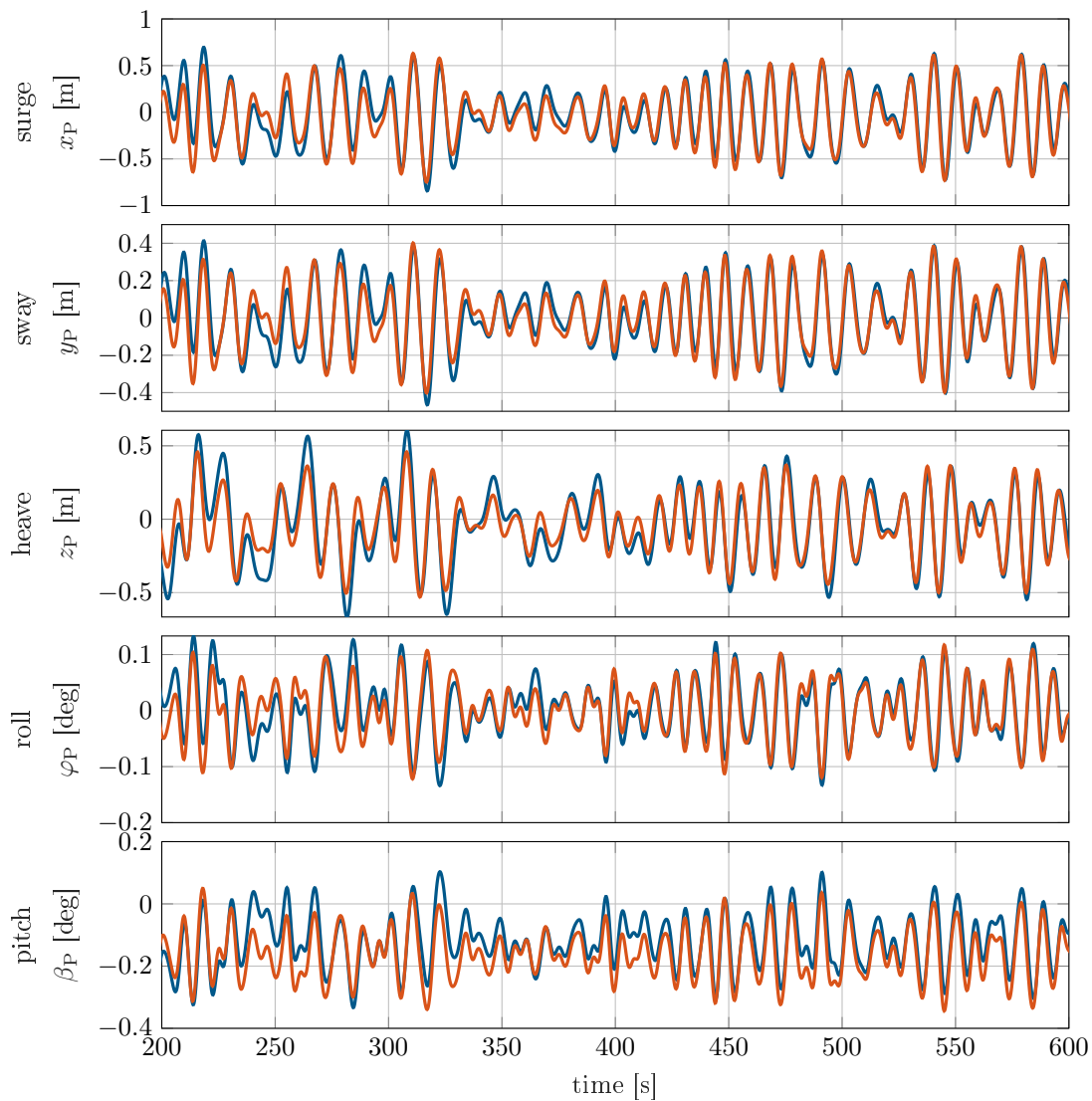
#### Stand-alone 3D SLOW

Figure 3.6 shows the comparison in the wave-only condition. The motions in all five DOFs agree very well between OpenFAST and SLOW. A very small offset in the platform pitch comes from the mass distribution of the turbine, whose blades are defined as flexible bodies in OpenFAST.



**Figure 3.5:** Time responses to EOG simulated by the coupled TLMCD and SLOW model using different coupling methods.





**Figure 3.6:** Comparison of time responses to waves between OpenFAST (blue line) and SLOW (orange line).

Comparisons of the system responses to wind and waves are presented in both the time domain (Figure 3.7) and the frequency domain (Figure 3.8). Both blue lines and yellow lines are simulated by OpenFAST. The only difference between them is in the wind field, where the blue lines use a 3D turbulent wind field and the yellow lines use uniform wind. Simulation results using SLOW are shown by the orange lines.

The largest difference can be found between the turbulent 3D wind field and the uniform wind, i.e. between the blue and yellow lines. In the time domain, the roll motion in 3D turbulent wind field is much larger due to the aerodynamic torsion caused by the spatial turbulence. In the frequency domain, the responses due to the spatial turbulence experienced by the blades are not captured by the uniform wind, which is visible near the three-per-revolution (3P) frequency range. In the lower frequency range, roll and sway are less excited by the uniform wind. Since SLOW uses only a rotor disk for the aerodynamics, these differences due to the wind field cannot be corrected. In spite of that, OpenFAST using uniform wind and SLOW have a better agreement in both time and frequency domain. The only difference is the static offset in the blade pitch sensor. Since the rotor disk of SLOW reads the lookup table of aerodynamic coefficients calculated with a bottom-fixed turbine, the steady position of the platform at different wind speeds is not taken into account, resulting in a steady offset in the blade pitch.

Another deviation comes from the mooring lines, which is evident in the fairlead sensor. Since SLOW only uses a lookup table to account for the static mooring forces, the high frequency responses due to the mooring dynamic effects can not be captured. For the pitch motion, there is a small discrepancy in the wave frequency range (around 0.09 Hz), where SLOW has larger responses than that of OpenFAST in the frequency domain. This is however not significant in the time domain.

### 3D SLOW coupled with TLMCD

Having accessed the differences between the FOWT simulation models, it is convenient to analyze the modeling capabilities when coupling a TLMCD to a FOWT and identify the impact of a TLMCD.

As previously discussed, the discrepancies between OpenFAST and SLOW are mainly due to the wind field and the aerodynamic model. Therefore, the verification of the model starts with load cases excluding aerodynamics. In Figure 3.9 (a), which illustrates the pitch decay test, both models show strong agreement. Moving to the second load case (Figure 3.9 (b)), the coupled system here is subjected to a regular wave with an amplitude of 4 m and a period of 15 s, with all DOFs initialized at zero positions. As can be seen, the simplified model also captures the same

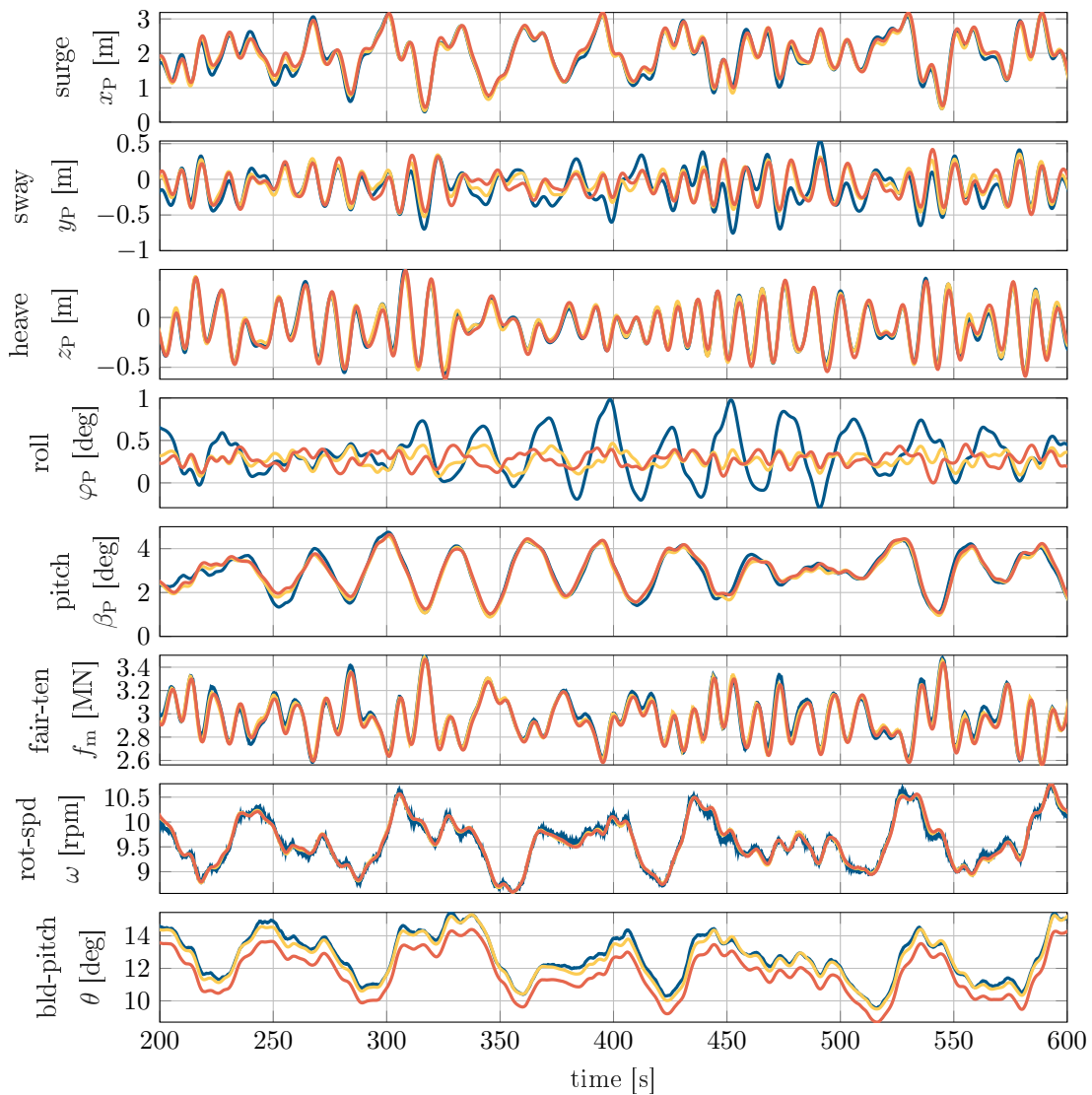


**Figure 3.7:** Comparison of time responses to wind and waves between OpenFAST with 3D wind field (blue line), OpenFAST with uniform wind (yellow line) and SLOW (orange line).

dynamics observed in both the transient and harmonic oscillation periods. Notably, there is a minor deviation in the free surface sensor during the harmonic oscillation period - more specifically, the free surface in the OpenFAST coupled model appears smaller than that in the SLOW coupled model. Overall, the simplified coupled model reproduces the most relevant system dynamics of the OpenFAST model in

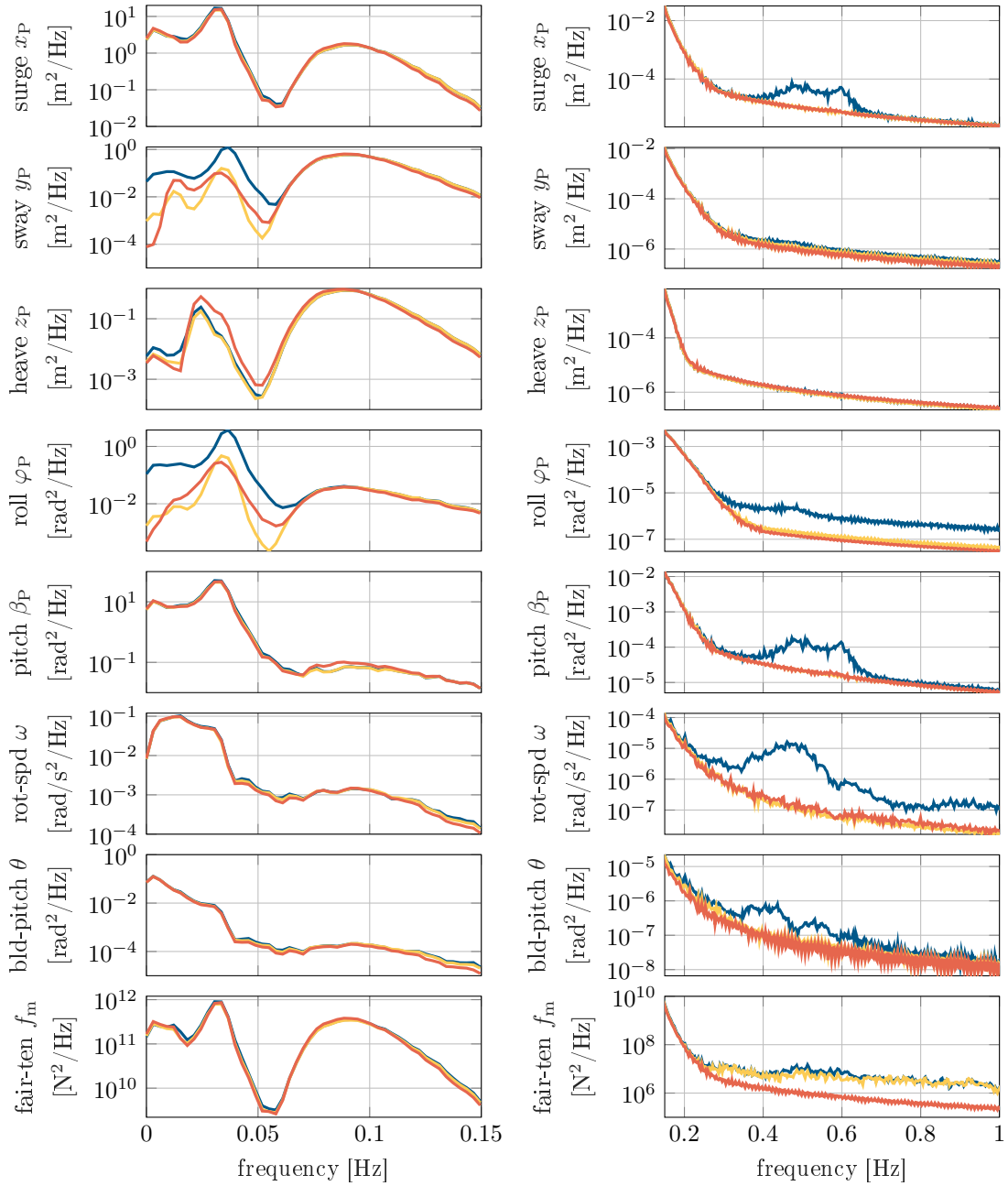


**Figure 3.8:** Comparison of frequency responses to wind and waves between OpenFAST (blue line with 3D wind field and yellow line with uniform wind) and SLOW (orange line).

the absence of aerodynamics.

For load cases involving wind and aerodynamics, the simplified FOWT model

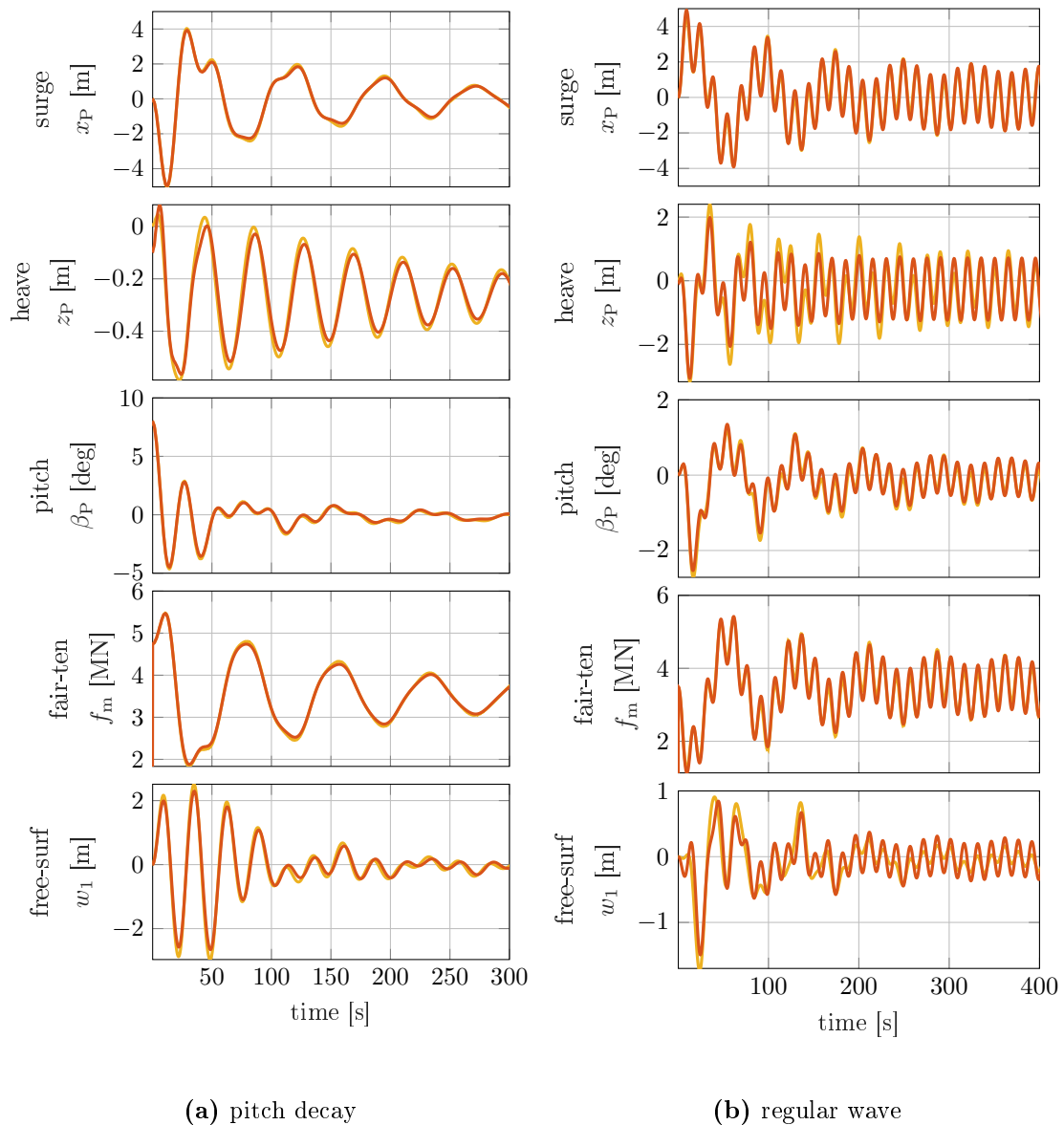


**Figure 3.9:** Comparison between OpenFAST (yellow line) and SLOW (orange line) for the FOWT and TLMCD coupled system in load cases without aerodynamics.

SLOW shows differences due to the simplified aerodynamics. In order to specifically assess the impact of the coupling of the TLMCD, a uniform wind field is employed in the simulations, isolating and focusing only on the effects of the TLMCD.

Figure 3.10 illustrates the dynamic responses in the time domain, while Figure 3.11

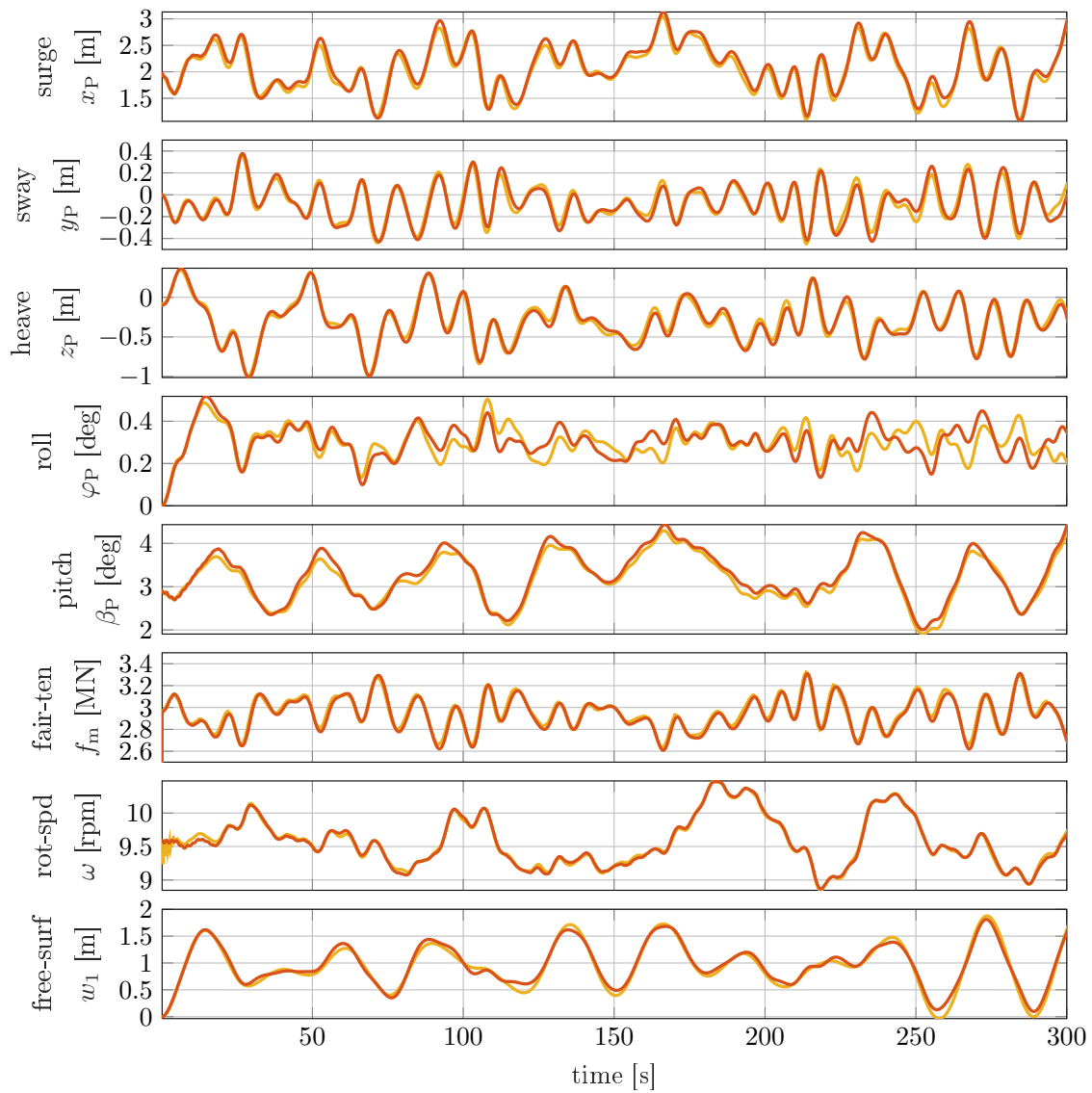


**Figure 3.10:** Comparison of time responses of the FOWT and TLMCD coupled system to wind and waves between OpenFAST (yellow line) and SLOW (orange line).

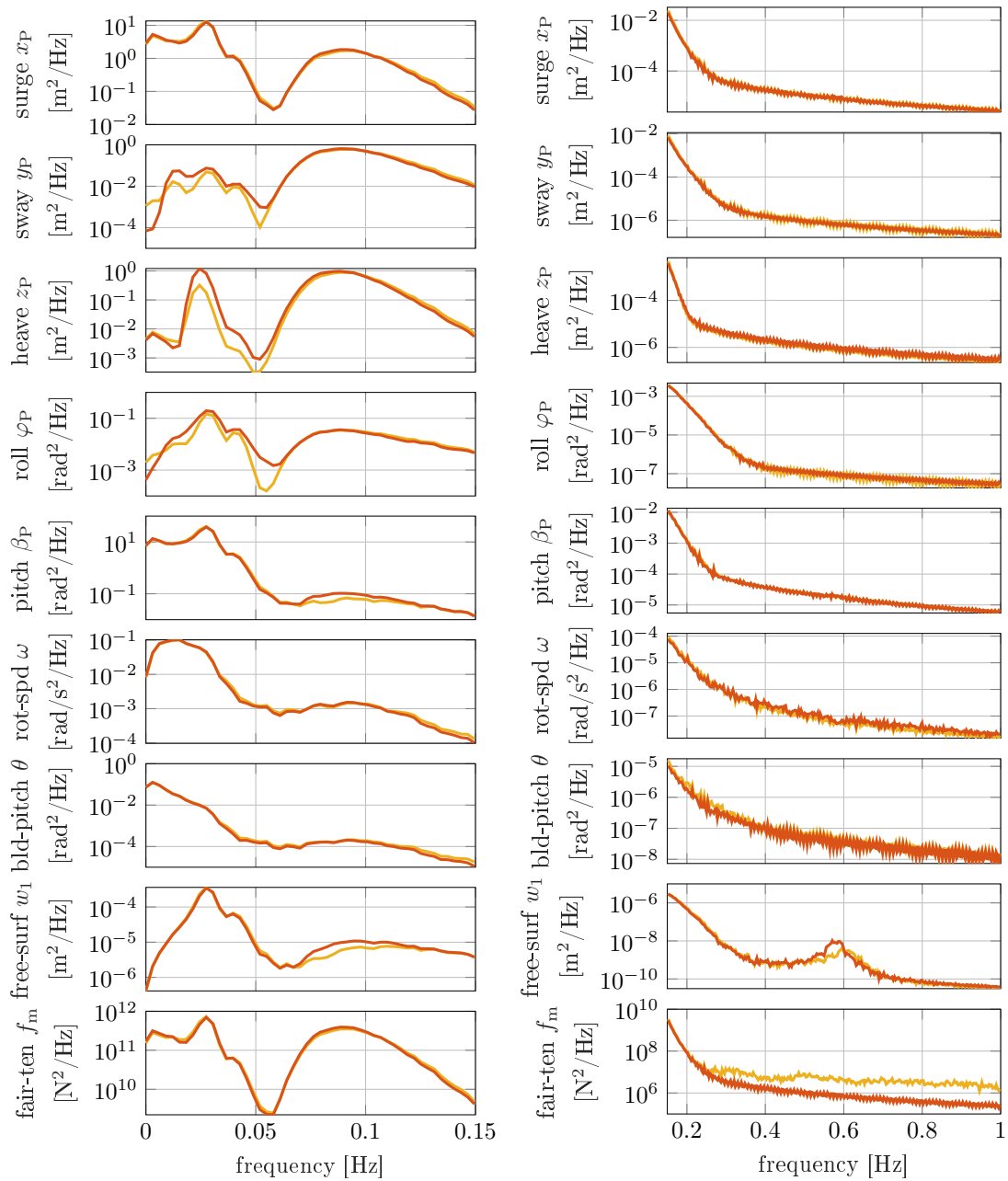


**Figure 3.11:** Comparison of the FOWT and TLMCD coupled system frequency responses between OpenFAST (yellow line) and SLOW (orange line).

compares the differences in the frequency domain. The response patterns are similar to those of the stand-alone SLOW model, but with noticeable differences due to the modeling simplifications mentioned above. In particular, the fairlead tension is underestimated in the higher frequency range due to the absence of dynamic effects from the mooring system. In addition, discrepancies in roll and sway motions at lower frequencies can be linked to the simplified aerodynamic model, where the aerodynamic torque is not included in the SLOW model.

Regarding the coupling of the TLMCD, both models exhibit a remarkable similarity in behavior. However, the SLOW coupled model demonstrates slightly larger amplitudes in both pitch motion and free surface dynamics. This divergence is evident within the wave frequency range in the frequency domain. These variations are directly due to the over-predicted pitch motion of the FOWT, as observed in the uncoupled scenario (Figure 3.8). Given the significant influence of the pitch motion on the free surface and its consequential impact, generating a stabilizing moment in the pitch direction, these discrepancies are further amplified in the coupled system.



# 4 Experimental Validation

To validate the developed numerical tool, two test campaigns are carried out. The first campaign tests a stand-alone TLMCD model in the laboratory of Stuttgart Wind Energy (SWE). And the second campaign involves testing a coupled system in the wave tank of the Environmental Hydraulics Institute of Cantabria (IHC). The majority of the results from these tests are published in [56, 53]. This chapter provides comprehensive insights into the setup of both test campaigns and presents the validation results, all of which are presented at the prototype scale.

## 4.1 Calibration of the TLMCD Stand-alone Model

In order to validate the numerical model established in Section 3.4, a scaled stand-alone TLMCD with three columns is built. With the prescribed platform motion in six DOFs, decay tests and harmonic oscillation tests are carried out. This section presents the test setup in Section 4.1.1, the data obtained, as well as the comparison between test and simulation in Section 4.1.2 and 4.1.3.

### 4.1.1 Laboratory setup

The stand-alone TLMCD experiments are carried out in the SWE laboratory. The hardware setup consists of a 6 DOF motion platform, a motion control software and a data acquisition system. The scaled TLMCD model is mounted above the motion platform. Free surface sensors are placed on top of each vertical column of the TLMCD. Figure 4.1 shows a sketch of the experimental setup. A photograph taken during the experiments is shown in Figure 4.2, which demonstrates the final implementation. A detailed description of the physical model construction, the sensors and the execution of the experiments can be found in [57]. The focus here

is on the validation and calibration of the numerical model.

Infrared laser distance sensors, installed at the top of each vertical column of the TLMCD, are used to measure the free surface motion. Short pulses of laser light are emitted to track the free surface inside each column. When the laser pulse reaches the free surface of the fluid, it is reflected towards the receiver. Based on the time difference between the laser emission and reception, the distance between the sensor and the free surface is calculated. The accuracy of the sensors is up to 3 mm.

The dimensions of the tested TLMCD are listed in Table 4.1. All the values are given without the wall thickness, i.e. the inner dimensions.

**Table 4.1:** Parameters of the scaled TLMCD.

Parameter	Value [mm]
Vertical column height $L_v$	405
Vertical column diameter $D_v$	174
Horizontal arm width $b_h$	155
Horizontal arm height $h_h$	16
Horizontal arm length $L_h/2$	597.3
Vertical location of the streamline origin $e$	70

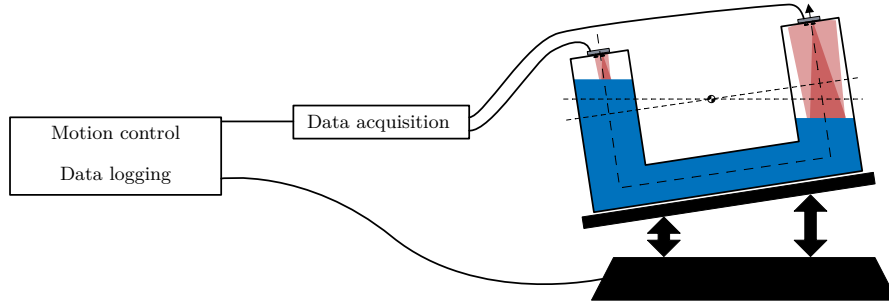


**Figure 4.1:** Illustration of the experimental setup with the data acquisition system included [57].

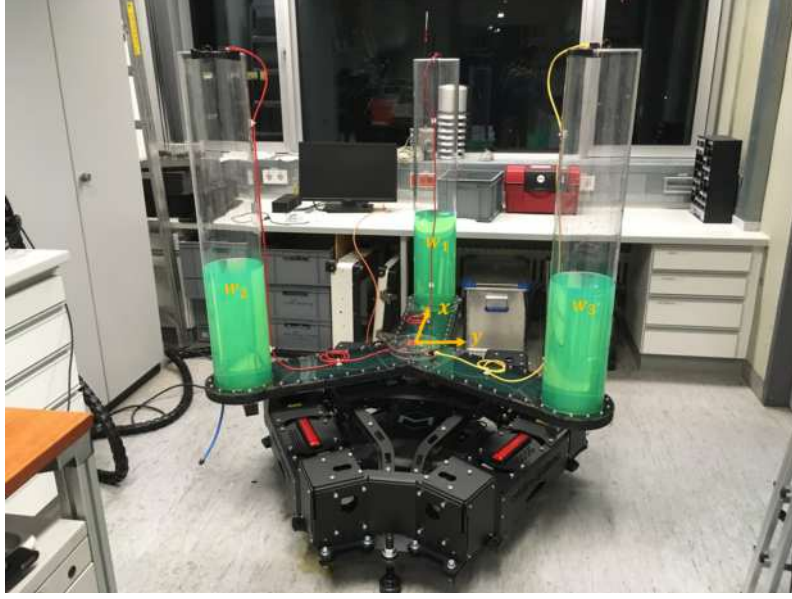


Figure 4.2: Hardware setup of the TLMCD laboratory test.

### 4.1.2 Free decay test

The most important properties to be determined through decay tests are the natural frequency and damping coefficients. According to Equation 3.72, the mass matrix depends on the system state  $\mathbf{w}$ . The natural frequency, without considering the dynamic term, is determined by [36], which is

$$\omega_0 = \sqrt{\frac{g}{\frac{L_h}{2} \frac{A_v}{A_h} + L_v}}. \quad (4.1)$$

This is also in line with the natural frequency of the two-column TLCD given by [28]. Besides the analytical method, the natural frequency can also be determined experimentally by fitting the measured free surface position to an exponentially decaying sinusoidal curve. The corresponding fit function is expressed as

$$w_i = w_{i,0} e^{-\zeta \omega_0 t} (\cos(\omega_d t) + \frac{\zeta}{\sqrt{1 - \zeta^2}} \sin(\omega_d t)) \quad (4.2)$$

---

<sup>†</sup>Note that the  $L_h$  in [36] should be  $\frac{L_h}{2}$ .

where  $\omega_0$  is the undamped natural frequency and  $\omega_d = \omega_0\sqrt{1 - \zeta^2}$  is the damped natural frequency.

Figure 4.3 compares the free surface position in the vertical column of element No.1 between experiment and simulation. It is observed that the experiment has a higher natural frequency than the simulation without calibration. This phenomenon has been reported in previous studies, including [55] through experiments and [54] through high-fidelity CFD simulations. However, these studies are limited to conventional two-column TLCs. This is due to the poorly defined fluid velocity inside the TLC, particularly at the transition part or sharp corners, because a certain amount of water remains stationary instead of flowing along the ideal streamline. This requires a different amount of fluid to achieve the desired natural frequency for a TLMCD, which is described as the effective volume of tank fluid in [55]. The theoretical fluid volume to match the desired natural frequency has a discrepancy of about 12% compared to the actual fluid volume. While the mass term in [54] is corrected based on CFD simulations, the correction factor varies between 10% and 30% depending on the TLC configurations. In contrast, the correction factor for the mass term in [36] is found to be only 5%. In this work, a correction factor of 32% is applied to the mass matrix of the TLMCD, denoted by  $(1 - \mu)\mathbf{M}_q$ . This may seem large compared to the 5% correction in [36], but it can be explained by the narrow horizontal arms of the Seaplace FOWT design, which contribute significantly to the correction factor  $\mu$ . Nevertheless, this correction is considered acceptable as it is close to the range found in [54].

As for the calculation of damping, Appendix A has formulated the detailed data processing of the experimental results. Based on this, both linear and quadratic damping are determined:

$$\begin{aligned} b_1 &= 0.0145 \\ b_2 &= 0.3514 \end{aligned} \tag{4.3}$$

The head loss coefficient  $\eta = 0.7$  is calculated using

$$\eta = \frac{(1 - \mu)m_t b_2}{0.5\rho A_v \gamma}. \tag{4.4}$$

A study on the damping coefficients is made in [36]. It is concluded that the linear

damping coefficient is more influenced by the cross-sectional shape and the quadratic damping coefficient is influenced by the scaling factor, which is the actual length of the columns. The reason for this is that the linear damping is dominated by the sudden pressure change at the junction area or sharp corner, which is called minor head loss. However, the major head loss that influences the quadratic damping is dominated by the fluid viscosity. The linear damping coefficient in [36] lies between 0.0328 (for square cross section) and 0.0087 (for circular cross section). The TLMCD tested here consists of both square and circular cross section and the linear damping ratio  $b_1$  is estimated to be 0.0145, which is a plausible value. As for the quadratic damping ratio  $b_2$ , a higher value is found for TLMCDs with smaller geometrical size in [36]. Since the TLMCD tested here is much smaller than that in [36],  $b_2$  is larger here as well.

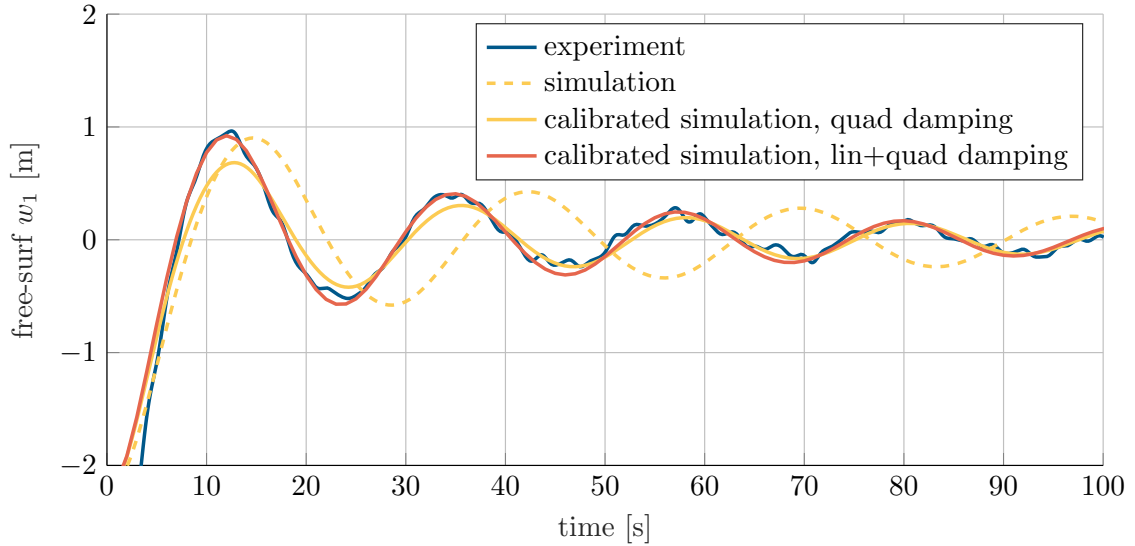


**Figure 4.3:** Comparison of the stand-alone decay test between experiments and different calibrated models.

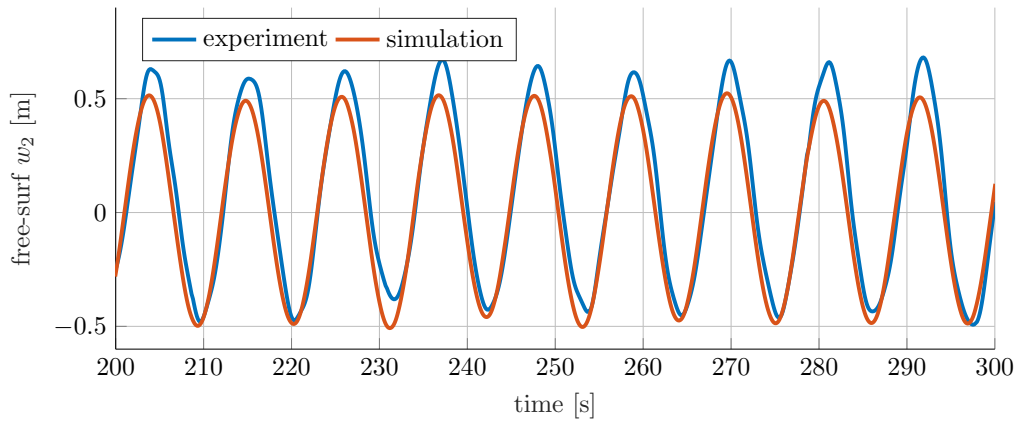
The final calibrated model based on the lab test is plotted with the red solid line in Figure 4.3, along with the original model and the partially calibrated model. It is clear that both linear and quadratic damping are important for the accuracy of the model. The calibrated numerical result agrees well with the experimental results.

### 4.1.3 Forced harmonic oscillation

To evaluate the dynamic responses, a motion platform is used to artificially reproduce the motion of a FOWT under regular wave excitation. The TLMCD is mounted on the motion platform and thus subjected to sinusoidal forcing. Tests are performed under both roll and pitch motions, i.e. rotation around the x-axis (roll) and y-axis (pitch) in Figure 4.2. Since the results show similar conclusions, only one set of the tests is shown and discussed here. The prescribed input roll signal, imposed on the motion platform, is

$$\varphi_{\text{mp}}(t) = \hat{\varphi}_{\text{mp}} \sin\left(\frac{2\pi t}{T_{\text{mp}}} + \theta_{\text{mp}}\right). \quad (4.5)$$

The maximum angle of the motion platform  $\hat{\varphi}_{\text{mp}}$  is set to 10 deg. Responses in various wave periods  $T_{\text{mp}}$  are tested, by prescribed motion ranging from 11 s to 55 s. The response of the free surface, which represents the fluid motion inside the TLMCD, is compared with the numerical results to validate developed stand-alone TLMCD model.



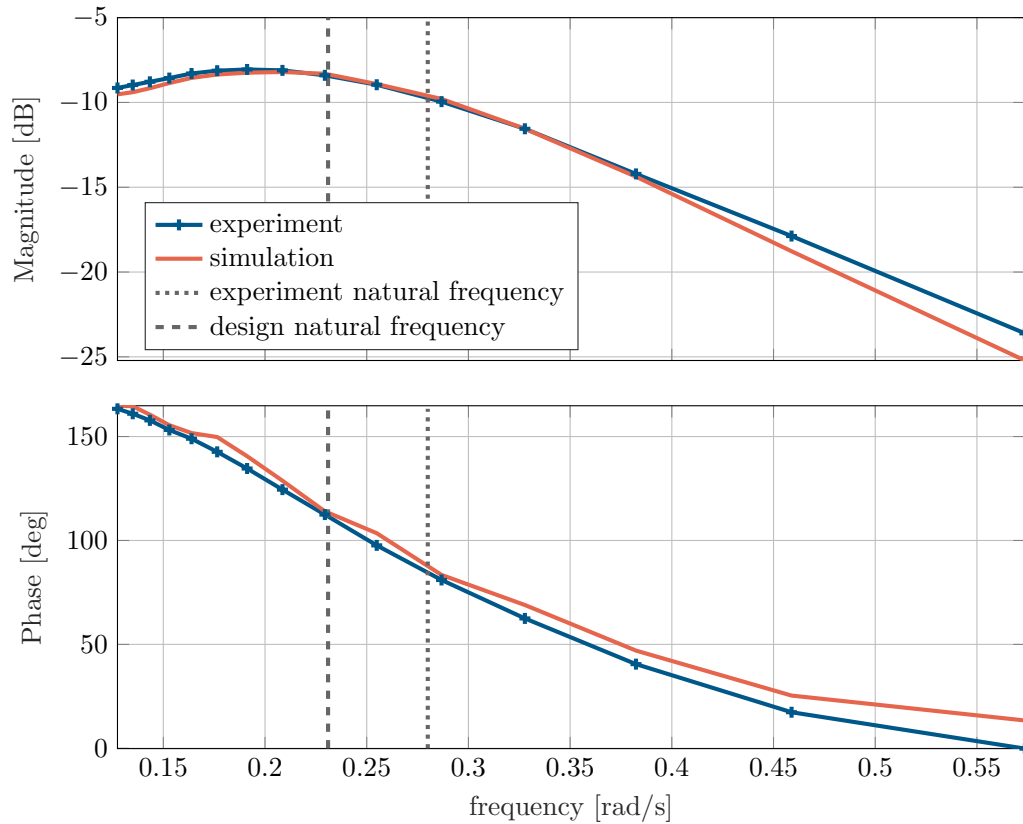
**Figure 4.4:** Comparison between the experiment and simulation of the time response of the free surface  $w_2$  under a prescribed sinusoidal motion with a period of  $T_{\text{mp}} = 11$  s.

Figure 4.4 shows the time response of the free surface  $w_2$ , the location of which is indicated in Figure 4.2. It is clear that the free surface experiences sinusoidal oscillation at the same frequency as the frequency of prescribed motion without

phase lag. The small difference is observed in the positive peak value (a positive value here means that the free surface is rising). For an ideal flow, the mean value of the free surface should be zero, which is the case in the simulation. The higher value measured in the experiment cannot be explained by physical reasons, but may be due to the sensors. On the one hand, the amplitude of the free surface motion becomes smaller when excited at higher frequencies, so that the sensor accuracy of 3mm leads to a larger relative measurement error. On the other hand, the ability to reproduce the prescribed motion of the motion platform decreases as the motion frequency increases. However, this cannot be proven within the scope of this test campaign.

If the amplitude of the sinusoidal response in Figure 4.4 is divided by the amplitude of the input signal, i.e.  $\hat{\varphi}_{mp}$  and the phase is subtracted by  $\theta_{mp}$ , a quasi transfer function from the motion platform roll motion to the TLMCD free surface motion can be derived. The term "quasi" is used here because a transfer function is normally a characterization for linear time-invariant systems, whereas the TLMCD system is nonlinear. Nevertheless, such a transfer function approximation can characterize and summarize the behavior of the TLMCD system quite well.

The Bode plot of the resulting "quasi" transfer function is given by Figure 4.5. The frequency range shown corresponds to that of the experiments. Each marker on the blue line represents a test under a specific regular wave excitation. The red line represents the results of the simulation model, calibrated according to the decay tests. The comparison shows a good agreement between the numerical model and the experimental model, especially in the region close to the natural frequency of the TLMCD, which also proves the effectiveness of the tuning process carried out in Section 4.1.2. Since the measured natural frequency is higher than the originally designed theoretical one, both of the frequencies are marked with different types of dashed lines. The time response shown in Figure 4.4 represents the frequency 0.57 rad/s, which has the largest error among the frequencies tested. Considering the relatively small difference of the time domain response in Figure 4.4, it can be concluded that the simulation model of the TLMCD has a very good performance and reproduces the free surface motion quite well.



**Figure 4.5:** Quasi transfer function from roll motion  $\varphi$  [deg] to TLMCD free surface position  $w_2$  [m], showing the response amplitude and phase lag of the free surface of the stand-alone TLMCD subjected to a sinusoidal roll motion in frequency domain.

## 4.2 Full System Wave Tank Test

To validate the established coupling between the TLMCD and the FOWT, a scaled model was tested together with the Seaplace 10MW FOWT. The test campaign of the scaled physical model is carried out at IHC by using a hybrid testing approach. The testing is funded by the Eurostars project CROWN. This section first describes the setup of the hybrid model, including the utilized sensors and load cases used. After that, the validation results using the coupled SLOW model are discussed.



### 4.2.1 The physical model, sensors and test matrix

The tested FOWT, the so-called CROWN Spar, is an evolution of the original RDS developed in the CHEF Turbine project, as part of the European DemoWind co-funding research program. The dynamic response of the original RDS in survival conditions is presented in [58]. The updated 10MW version CROWN is scaled down by a factor of 1:36 here. As can be seen in Figure 4.6, the scaled physical model consists of the following components:

- **Platform:** The scaled model is made mainly of painted aluminum (partially steel), with the mass characteristics adjusted by using a combination of solid ballast and liquid ballast (water). The internal subdivision of the model fully reproduces the dynamic effects of liquid ballast in the tanks, including a specific design of the TLMCD, fitted within the ballast tanks. A calibrated 3-line spread mooring system (truncated) is attached to the 3 fairleads, located at the top of the caisson.
- **Tower:** The tower is designed to provide the stiffness and strength necessary to withstand the forces produced by the turbine rotor. The platform is considered as a rigid body. The Qualysis markers and several of the devices serving the sensors layout are placed along the tower.
- **Multifan:** It is a component of the Hardware-in-the-Loop (HIL) system that is capable of reproducing the aerodynamic forces, which replaces the physical wind turbine. With an array of fans placed at the tower top of the FOWT model, the equivalent aerodynamic thrust forces can be calculated and reproduced in real-time based on the inflow conditions and the measured platform dynamics.
- **TLMCD:** The TLMCD is made of aluminum and consists of three vertical cylinders, which are connected to each other by a y-shaped duct that links their lowest part, see Figure 4.7. The connecting duct is fitted into the heave plate of the platform. During the different test campaign configurations, the TLMCD is enabled or disabled by activating or deactivating the vent placed on the cylinders cover, so that the fluid flow is controlled as required. Note that the geometry of the tested TLMCD at IHC differs slightly from the one tested in the lab of SWE, due to the limited choice of materials. The parameters of

the TLMCD are summarized in Table 4.2.

- **AHBS:** The Anti-Heeling Ballast System (AHBS) is composed by a set of electro-valves, a pump and tubes, which is used to compensate the mean tilting angle induced by the aerodynamic thrust forces. This system will not be discussed in detail as none of the tests associated with the AHBS are discussed in this work. However, it is important to note that the mean platform pitch angle is zero due to its presence.

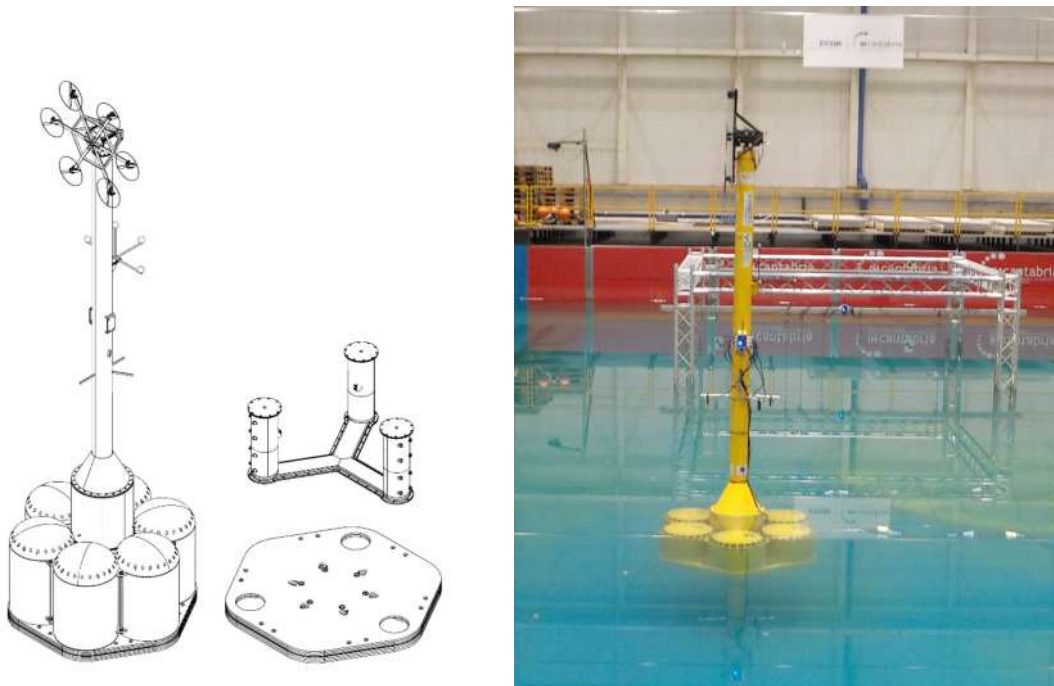


**Figure 4.6:** Sketch (left) and photo (right) of the scale model at IHC.

With the aim of collecting the required physical phenomena occurring during the tests, the following set of instrumentation and sensors have been used:

- Free surface transducers to measure water level oscillations in the basin (wave gauges), run-up around central column and water level oscillations inside the platform cylinders and TLMCD.
- Track motion system (Qualisys) to measure the FOWT motions.
- Axial load cells to measure forces on mooring lines.
- Accelerometer to record accelerations at the nacelle.

**Table 4.2:** Parameters of the scaled TLMCD at IHC.

Parameter	Value [mm]
Vertical column height $L_v$	388.9
Vertical column diameter $D_v$	178
Horizontal arm width $b_h$	150
Horizontal arm height $h_h$	20
Horizontal arm length $L_h/2$	582
Vertical location of the streamline origin $e$	-1166.7

**Figure 4.7:** Photo of the scaled TLMCD tested at IHC.

Multiple load cases are carried out, which can be categorized into two groups. One group is used to calibrate and validate the FOWT simulation tool. In this case, the TLMCD is deactivated by placing the waterproof rubber stopper directly on top of the free surface. The other group of load cases are defined to evaluate the performance of the coupled TLMCD and FOWT system. This means that the rubber stopper is removed and the fluid inside the TLMCD can flow freely. In general, the load cases can be divided into the following subsets:

- Static structural characterization
- Decay tests for dynamic system characterization
- Wind or wave only cases for system tuning
- Wind & wave combined cases for the validation of the system

- Special cases proving the functionality of the TLMCD, the state observer and the AHBS

Considering the objective of the present work, only a limited scope of load cases are selected here. These include the translational and rotational decay tests for the characterization of the dynamic system, regular wave-only cases to check the RAOs, and wind and wave combined cases evaluating the overall system dynamics. Finally, special cases are selected to demonstrate the functionality of the TLMCD. All of the load cases are performed in both situations: with the TLMCD deactivated and activated. The detailed wind and wave information for the load cases are listed in the Tables 4.3 and 4.4.

**Table 4.3:** Parameters of the irregular waves described by JONSWAP spectrum.

sea state	1	2	3	4	5
$H_s$ [m]	7	9	10.5	8	4
$T_p$ [s]	8.6	11.1	14.2	16	18.2
$\gamma$ [-]	5	4.5	2	1	1

**Table 4.4:** Wind and wave combined Load Case (LC).

LC	$H_s$ [m]	$T_p$ [s]	$\bar{u}_{hub}$ [m/s]
1	4	18.2	50
2	8	16	16
3	8	16	25

## 4.2.2 System identification

The entire FOWT dynamic system is identified through a series of decay tests, which consists of two steps. The first step is to calibrate the FOWT numerical model based on the decay tests with the TLMCD deactivated. More specifically, the natural frequencies of the FOWT are calibrated and the hydrodynamic damping coefficients are determined. This provides a solid basis for evaluating the performance of the TLMCD, as well as validating the coupled TLMCD and FOWT system.

To match the natural frequencies in roll and pitch, the platform center of mass is reduced by 0.2% of the original value. Considering the uncertainty due to the construction and the final ballast tuning to obtain the designed draft, this calibration can be considered as reasonable. The hydrodynamic damping coefficients are calibrated according to the experimental results. Nevertheless, these damping coefficients are often not valid in different sea states. This is due to the fact that the dimensionless numbers  $Re$  and  $KC$ , which significantly affect the hydrodynamic damping, vary when the fluid velocity and FOWT velocities change in different sea states. Therefore, the hydrodynamic damping coefficients are recalibrated for the load cases with wind and waves. A large heave plate is attached to the bottom of the platform, contributing mainly to the heave damping, which is assumed to be quadratic and can be captured by the drag term in the Morison equation [59]. The drag coefficient of the heave plate  $C_{D, hp} = 2.8$  is determined by comparing the simulation with the experimental results, which agree quite well. Therefore, no additional linear damping is applied to the heave DOF. On the contrary, for the surge DOF, both linear and quadratic damping are essential. The quadratic damping is not fully represented by the Morison elements defined along the platform, with a Morison drag coefficient  $C_D = 0.6$ . In addition, a linear damping coefficient is added to the surge DOF. This can have a contribution from the radiation damping (omitted in SLOW), the mooring system (the dynamic effect is neglected by the quasi-static model). For the pitch DOF, the motion is partially damped by the Morison drag forces defined on the heave plate. Only one additional linear damping coefficient is added which gives good agreement with the experiments.

The final comparison of the decay tests is presented in Figure 4.8. The results demonstrate that good agreement between simulation and experiment can be achieved by manually tuning of the hydrodynamic damping, providing a solid basis for comparison with the TLMCD. Figure 4.9 shows the decay performance with the TLMCD activated, where sensor  $w_1$  indicates the TLMCD free surface position. The first noticeable phenomenon is that both roll and pitch motions are significantly damped due to the additional damping introduced by the TLMCD, as can be seen by comparing Figure 4.8c and Figure 4.8d. It is important to mention that the mass correction coefficient  $\mu$  is not required in this case, despite the calibration results from Section 4.1 indicating its necessity. The reason for this could be attributed

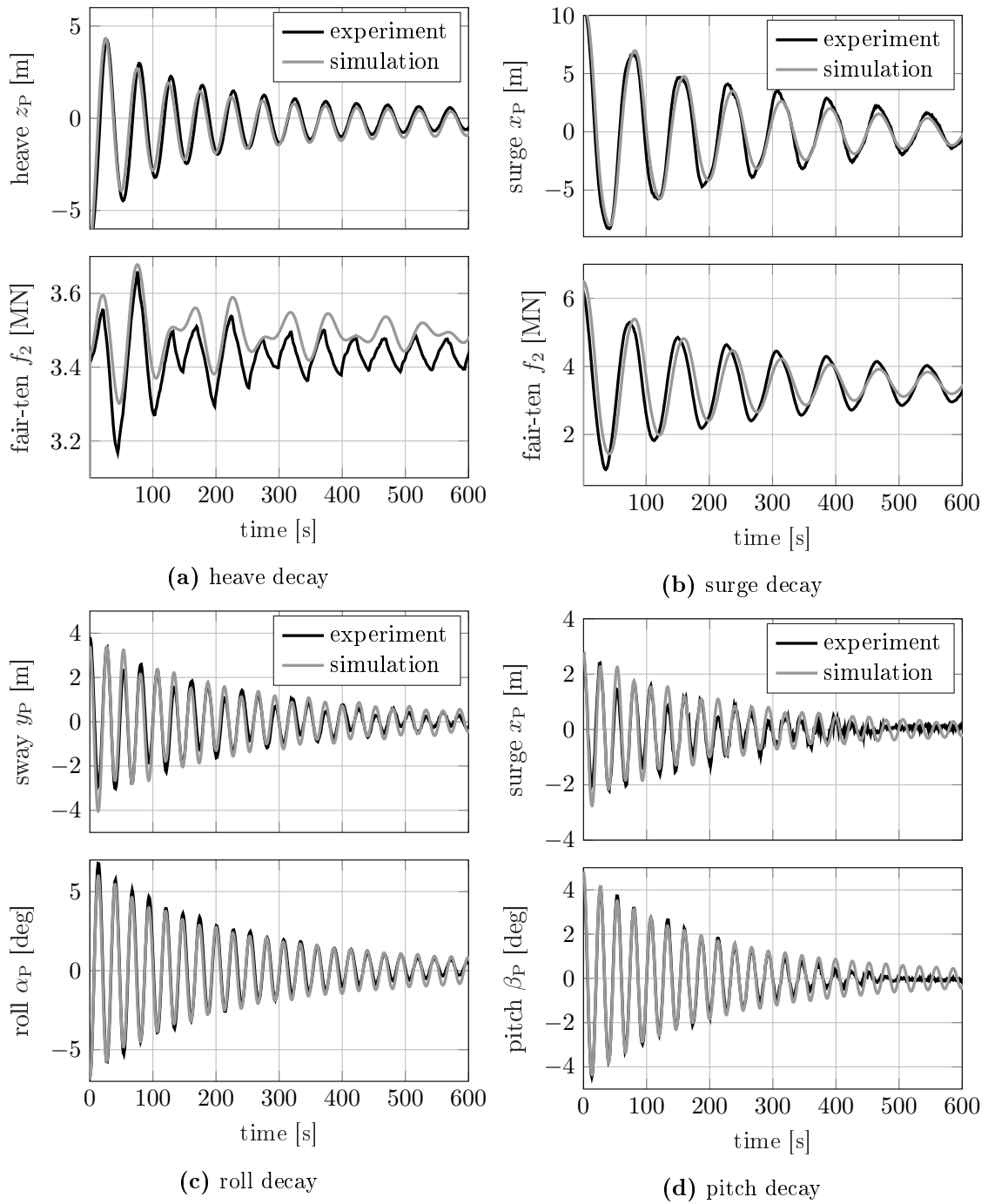


**Figure 4.8:** Comparison between simulation and experimental results of decay tests with TLMCD deactivated.

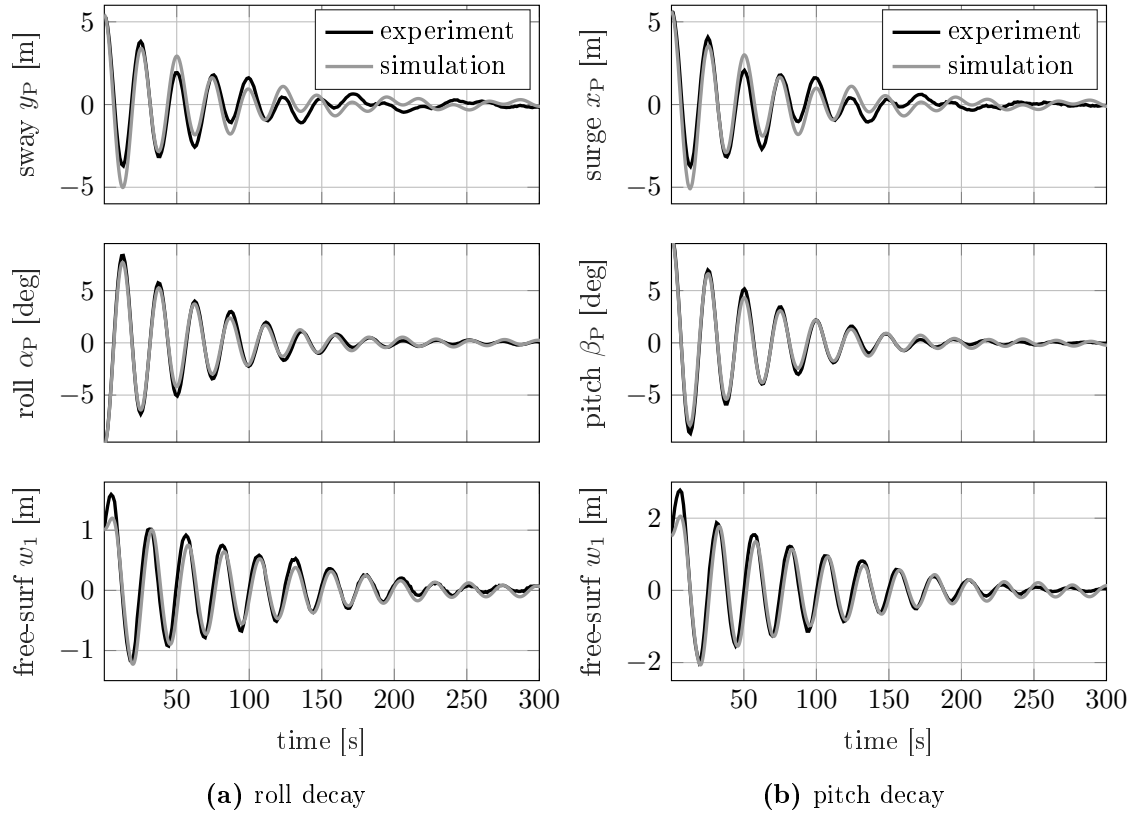


**Figure 4.9:** Comparison between simulation and experimental results of decay tests with TLMCD activated.

to the fact that the fluid flow inside the TLMCD follows the ideal streamline more closely when platform motions dominate. Therefore,  $\mu$  is set to zero for all the cases in the wave tank test. Additionally, the head loss coefficient derived from the lab test is not applicable, and thus  $\eta$  is adjusted to 2.8 to better match the experimental results, a value much larger than that in Section 4.1. The only parameter that remains the same is the linear term  $d1$ . However, it is important to note that the geometries of the two scale models tested are different, especially the cross-sectional area of the horizontal arm, which is a highly sensitive parameter for the damping ratio. Unfortunately, due to time and budget limitations, a thorough investigation of the effect of the horizontal arm geometries on damping could not be conducted in this work.

### 4.2.3 Wave-only load cases

Tests are carried out with regular, irregular and white noise waves. Based on the performance in white noise waves, tuning the drag coefficient  $C_D$  does not change the response much. Therefore, the irregular wave cases are used as the basis for determining the hydrodynamic damping coefficients.

#### Regular wave

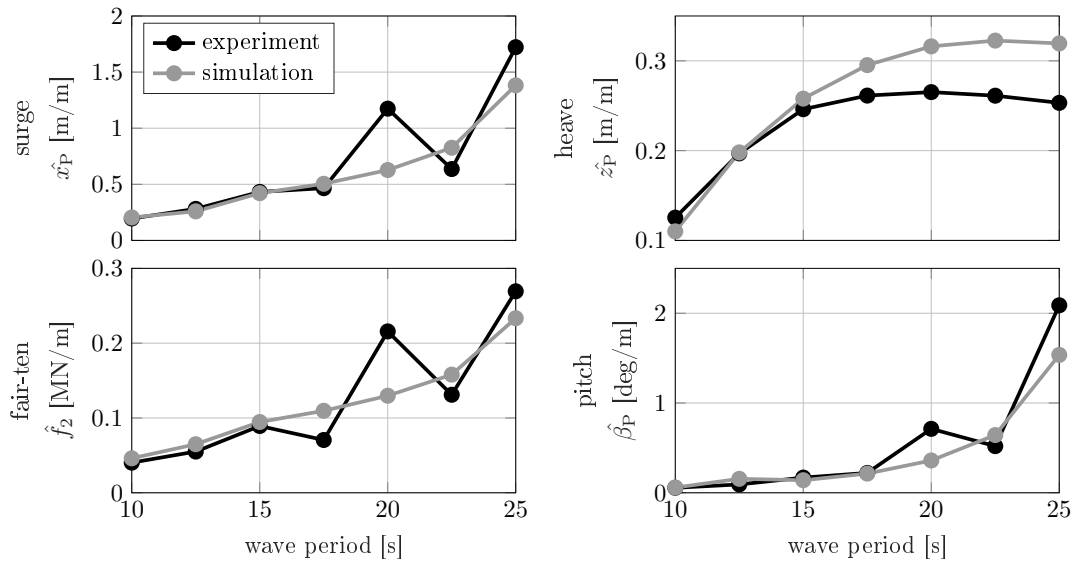
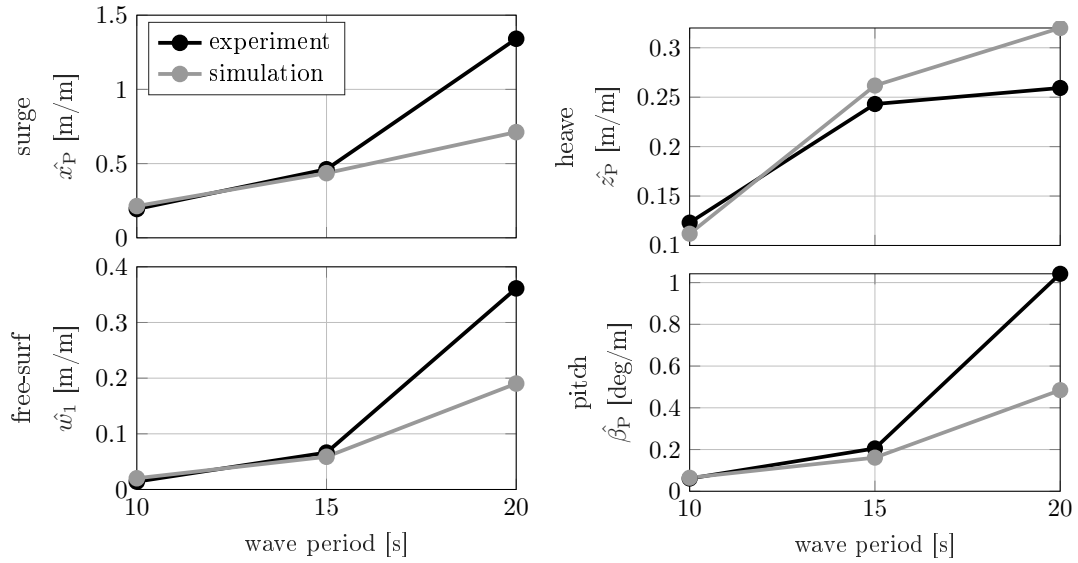


Figure 4.10: RAO based on regular wave tests with TLMCD deactivated.

Tests are carried out in regular waves with different wave periods from 10 s to 25 s. Two different wave heights were tested, i.e. 2 m and 4 m. Since the results are quite similar, only the cases with 4 m are shown here, and the platform response amplitudes are shown in Figure 4.10. In general, a good agreement between experiment and simulation can be obtained, except for the cases with wave period 20 s and 25 s, where large errors can be seen. This could be due to the parametric instability [60, 61], which is a common phenomenon existing in offshore structures, such as ships and spar platforms. The reason for this hypothesis is that the pitch stiffness is quite sensitive to the heave motion due to the very small water-plane area. Further discussion of this issue can be found in [56]. As the stability diagram





**Figure 4.11:** RAO based on regular wave tests with TLMCD activated.

is largely influenced by the damping and wave parameters [62], a detailed analysis on this is not carried out in this thesis.

The tests with TLMCD are performed under a reduced set of regular waves, i.e.  $T = [10 \ 15 \ 20]s$ . The response amplitude per meter wave height can be found in Figure 4.11. Similar to the results without TLMCD, apart from the good agreement at  $T = [10 \ 15]s$ , a large error in the Standard Deviation (STD) at 20s is evident. Again, this should be due to the parametric instability, which is already discussed in the cases where the TLMCD is not deactivated. Further details can be seen by looking at the time response. As an example, the time series for the wave period of 15s is plotted in Figure 4.12. Although the amplitude of the TLMCD free surface position is well reproduced, a small offset of the mean value can be seen.

### Irregular wave

As mentioned in Section 4.2.2, the hydrodynamic damping coefficients obtained from the decay tests are not valid in the presence of waves. Therefore, the coefficients are again manually tuned to match the system responses for different sea states described by the JONSWAP spectrum as shown in Table 4.3. Since the objective here is to obtain a reliable numerical model that can be used to validate of the

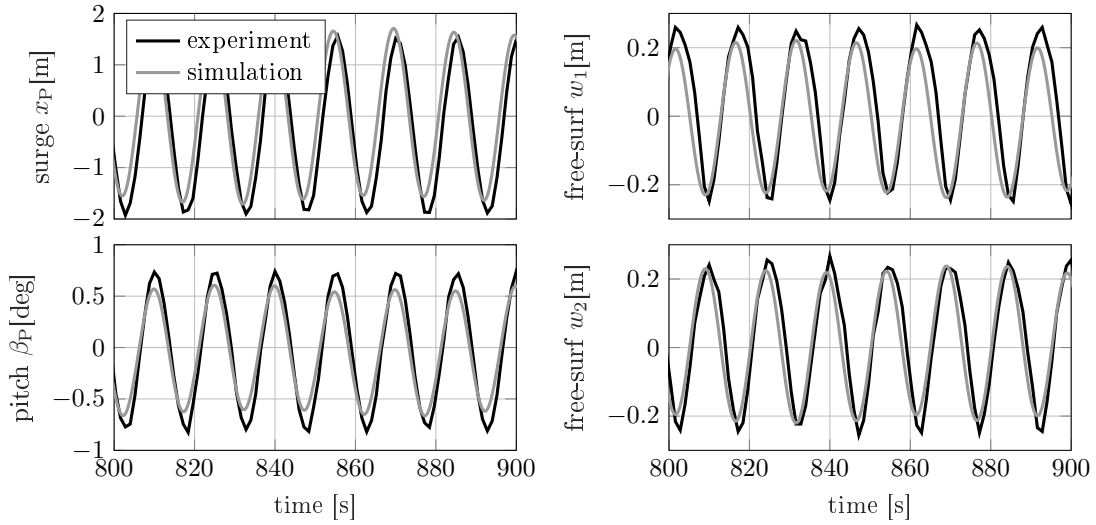


**Figure 4.12:** Time response in regular wave  $T = 15s$  with TLMCD activated.

coupled TLMCD and FOWT system, load cases with the TLMCD deactivated are used. It has been found that the Morison elements and hydrodynamic slow drift forces are necessary to capture the nonlinear damping, as well as the wave loads in the lower frequency range. The conclusion in [20] is also valid for the heave plate, i.e. the axial damping coefficient  $C_{D,hp}$  varies over sea states. However, this sea state dependent tuning does not hold for the hydrodynamic coefficient defined along the vertical columns of the platform, described as discretized members. This phenomenon could be caused by two reasons: One is due to the geometry of the platform, most of which is submerged in water where the velocity of the fluid particle is relatively low. The second is because of the special mooring system, with which the velocity of the platform surge motion is also relatively small. Considering the drag term of Morison's Equation, which is largely determined by the fluid and platform velocity, changing the drag coefficient doesn't significantly alter the Morison drag force in the surge direction. As a result, the drag coefficient is kept constant  $C_D = 0.6$  across all sea states. While the drag coefficient for the heave plate  $C_{D,hp}$  varies over sea states.

As a final result, Figure 4.13 shows the STD of the dynamic responses in irregular waves. Overall, the simulated results are in good agreement with the measured data. A noticeable deviation is found in sea state 1, where the heave motion is

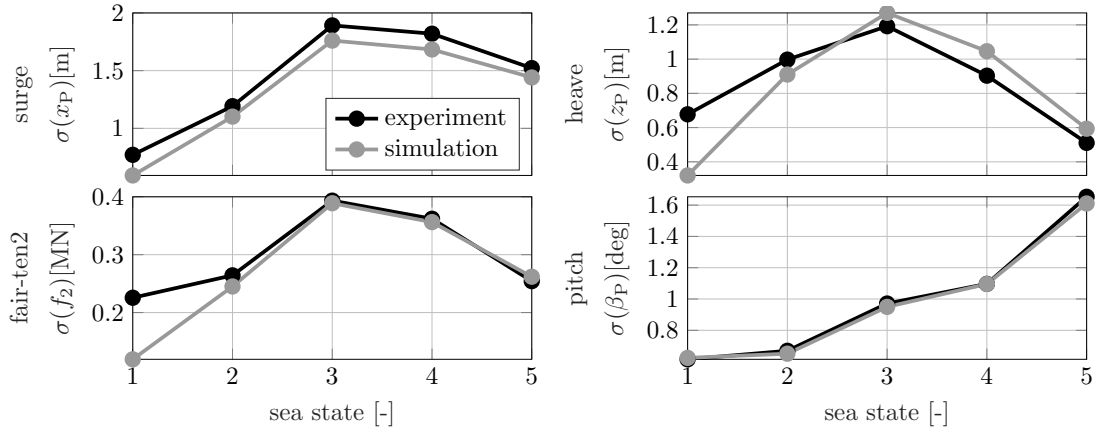


**Figure 4.13:** STD of responses in irregular waves with TLMCD deactivated.

visibly underestimated by the simulation model. This also leads to the difference in fairlead tension. However, this deviation cannot be eliminated by tuning the hydrodynamic damping coefficient. As sea state 1 is not used for the wind and wave combined cases, the current tuning is adopted for the following discussion.

#### 4.2.4 Irregular Wave and turbulent wind dynamic response

The previously calibrated model is used directly in this section, without further tuning. Simulations are carried out under various turbulent wind and irregular wave combined conditions. The selected LCs are listed in Table 4.4.

The dynamic responses of LC1 in both time and frequency domains are compared in Figure 4.14-4.15. The plots on the left side show the case when the TLMCD is inactive, while the plots on the right side present the case when the TLMCD is active.

Looking at the case where the TLMCD is inactive, overall, the simulation model is able to capture the dynamics of the FOWT. The amplitudes of the time responses are not well captured sometimes, especially in the heave and pitch DOFs. One reason for this is the time-varying water plane area due to the truncated cone-shaped transition piece. This results in a varying heave stiffness that is not captured in the simulation model. As a result, the Power Spectral Density (PSD) of the heave motion at the heave natural frequency (about 0.02 Hz) differs from the test measurements. Due to the strong coupling between heave and pitch, the pitch

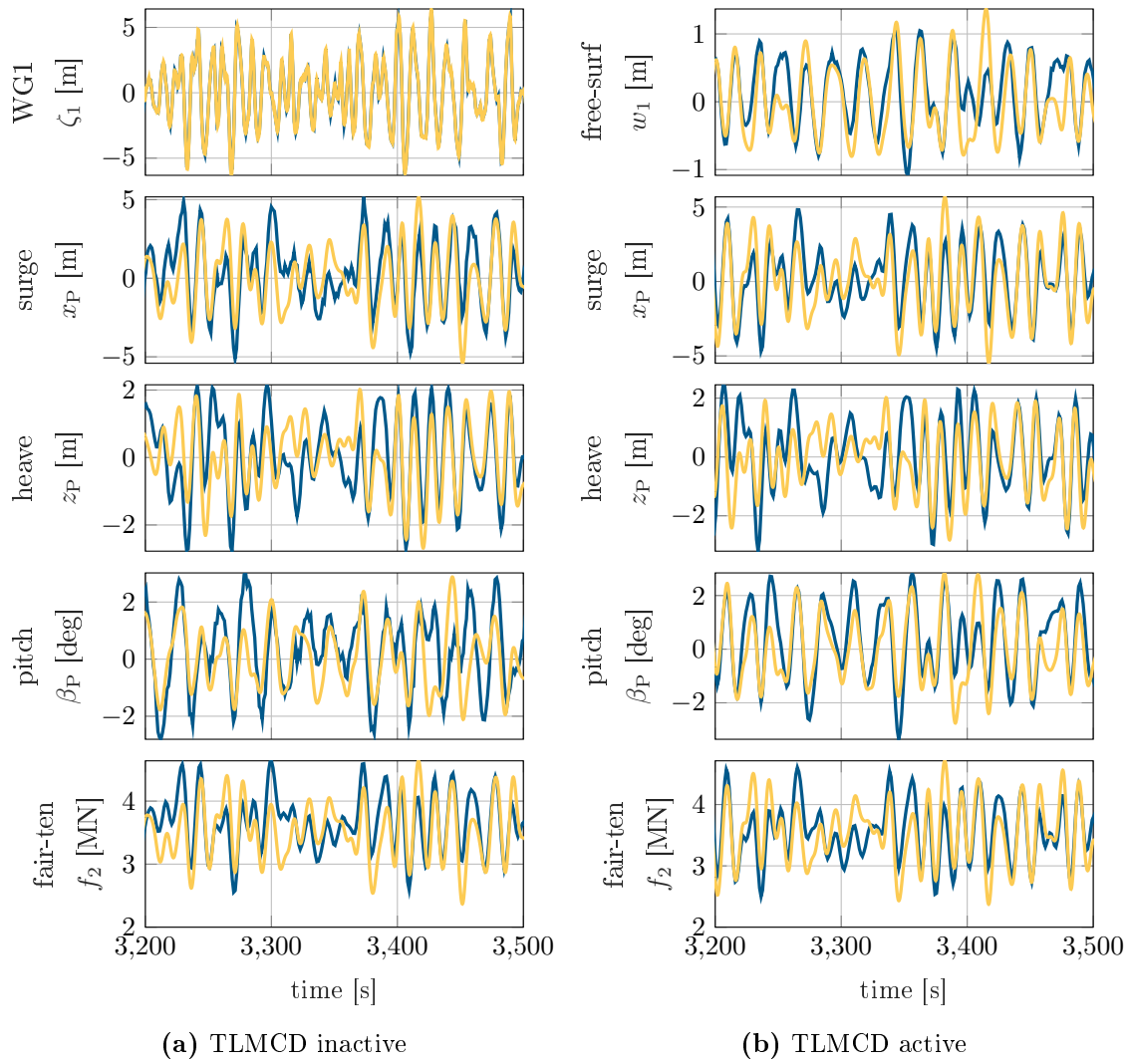


**Figure 4.14:** Comparison of time responses between experiment (blue line) and simulation (yellow line) in LC1.

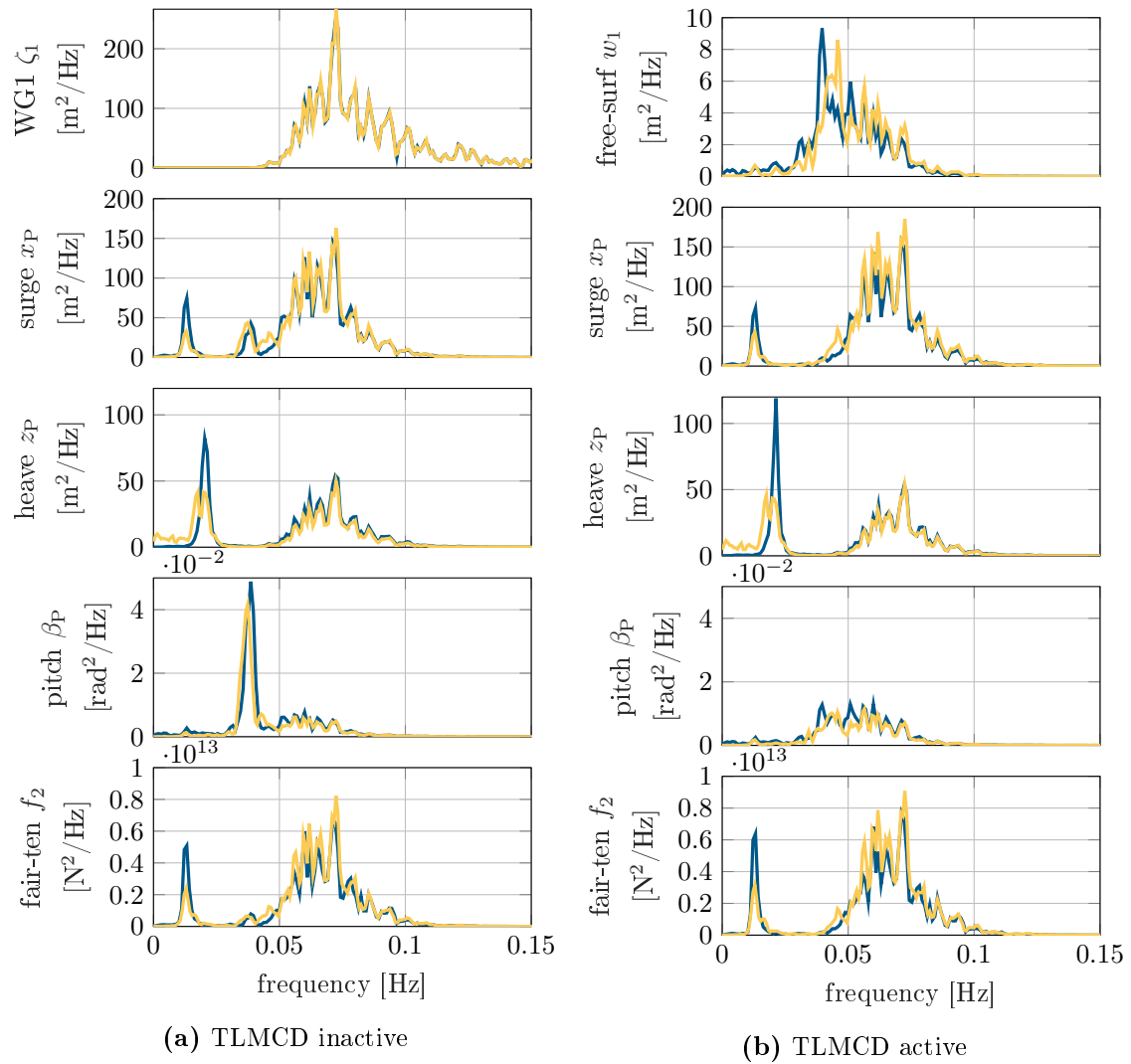


**Figure 4.15:** Comparison of frequency responses between experiment (blue line) and simulation (yellow line) in LC1.

motion is also affected. Another reason can be the viscous drag. Although Morison elements are attached to the platform and the heave plate. However, the reduced draft spar has a relatively large cross section compared to those slender cylindrical spars. How well the Morison equation with large diameters (over 50 m) can capture the viscous drag is uncertain. Since the focus here is to have a well tuned model to evaluate the TLMCD performance, rather than developing a perfect hydrodynamic model for this particular spar design, the differences between the simulation and measurement are also adopted.

When the TLMCD is active, the additional sensor free surface position  $w_1$  of the TLMCD is added to the plots, showing the fluid flow within the TLMCD. Figure 4.14b and 4.15b present the performance of the TLMCD and FOWT coupled numerical model. Similar to the pitch motion, some amplitudes of the time series are not captured. As the TLMCD free surface is mainly driven by the pitch dynamics in this load case, this error is largely inherited from the hydrodynamic model for the platform. Nevertheless, the overall performance is satisfactory, especially when comparing the pitch sensor in Figure 4.15a and Figure 4.15b. Because of the presence of the TLMCD, the PSD peak at the pitch natural frequency (about 0.04 Hz) is significantly damped, which is exactly the designed natural frequency of the passive TLMCD.

A similar comparison for LC2 is shown in Figure 4.16, where the turbine is in normal operation. A visible discrepancy can be detected at the frequency around 0.05 Hz (20 s), which has been detected in Section 4.2.3 as well. As previously discussed, the most probable cause of this behavior is the parametric pitch instability, which is amplified by the wave peak period in LC2 being closer to 20 s. Comparing the pitch sensor in Figure 4.16a and Figure 4.16b, the PSD peak at pitch natural frequency is again damped by the TLMCD, demonstrating the functionality of the TLMCD at the desired frequency. However, the motions at 20 s are excited, which is due to the additional dynamics at 20 s not being foreseen and considered during the TLMCD design phase. Otherwise, a different damping ratio could improve the performance at 20 s.

Due to this unmodeled dynamic at 20 s, it is more challenging to evaluate the effectiveness of the coupled FOWT and TLMCD model. To address this issue, the time series of the pitch motion and free surface position are plotted in Figure 4.17,

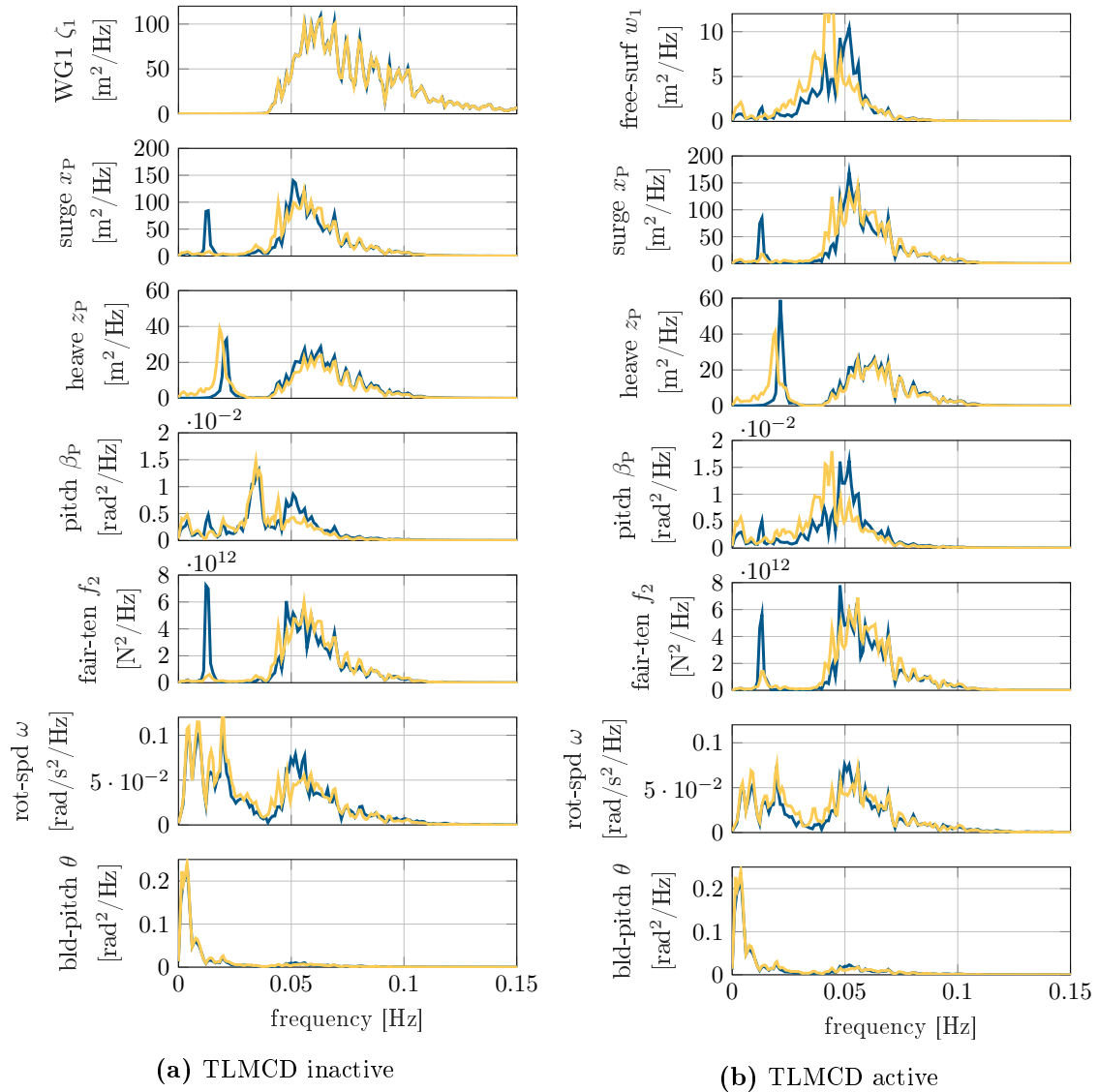


**Figure 4.16:** Comparison of frequency responses between experiment (blue line) and simulation (yellow line) in LC2.

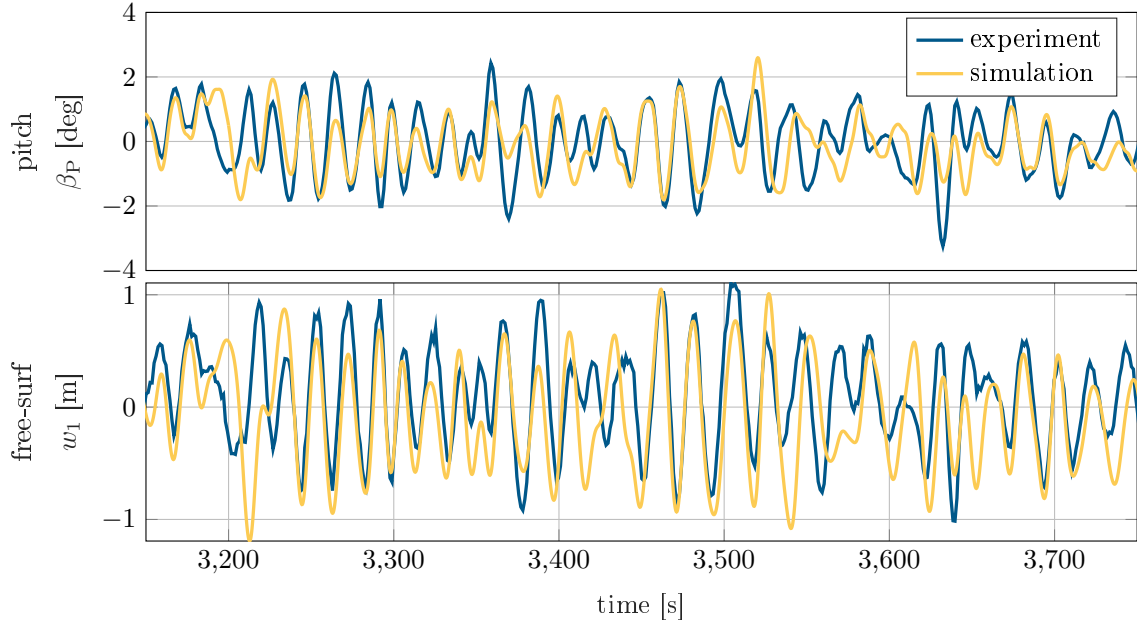


**Figure 4.17:** Comparison of time responses between experiment and simulation in LC2.

as the free surface is mainly influenced by the pitch motion when the wind and wave are coming from 0 deg. The figure shows that if the pitch motion is well reproduced by the simulation model, a better agreement of the free surface can be achieved. Table 4.5 presents the RMSE between the simulation and experiment for both LC1 and LC2, with the same simulation model parameters used regardless of whether the TLMCD is active or inactive. The results indicate that the coupling of the TLMCD does not deteriorate the predictive capability of the simulation model.

**Table 4.5:** RMSE between the simulated and the experimental results.

LC	TLMCD	surge [m]	heave [m]	pitch [rad]	rot-spd [rad/s]	fair-ten <sub>2</sub> [kN]	free-surf <sub>1</sub> [m]
1	inactive	1.95	1.15	0.03	0.11	269.20	-
	active	1.24	1.20	0.03	0.11	248.52	0.56
2	inactive	1.20	0.66	0.02	0.06	235.42	-
	active	1.00	0.72	0.02	0.06	250.54	0.51

Another notable difference is the rotor speed, which is visibly reduced at lower



**Table 4.6:** Parameter tuning for the TLMCD model based on physical tests.

	decay(lab)	driven-oscillation	decay(IHC)	wave-only	wind&wave
$\mu$	0.32	0.32	0	0	0
$b_1$	0.0145	0.0145	0.0145	0.0145	0.0145
$\eta$	0.6985	0.6985	2.8	3	3

frequencies when the TLMCD is activated. The reason for this is that the TLMCD provides additional damping, which can partially compensate for the negative aerodynamic effect and increase the bandwidth of the blade pitch controller. By adapting the blade pitch controller, which is the case discussed here, a better control performance can be achieved. This improvement in control performance aided by TLMCD has been demonstrated in [40] and will be further elaborated in Chapter 5.

As a summary, Table 4.6 has listed the final tuning results of the TLMCD related parameters based on experimental tests. Since no further experiments have been carried out, it remains unknown what are the sources of the differences regarding the damping coefficient. For the application studies in the following chapters, the values obtained from the wave tank tests are adopted.



# 5 Synergism between the TLMCD and the Blade Pitch Controller

Unlike a ship, which is mainly excited by waves, the motions and loads of a FOWT are more complex due to the large aerodynamic loads. It has been found that it is important for the blade pitch controller to work in synergy with the TLMCD, so that a better system performance can be achieved. In this chapter, a control design procedure is developed for the widely used SISO controller for floating wind turbines. Since the TLMCD introduces additional damping into the system, the performance of the blade pitch controller, which is limited by the negative aerodynamic damping, is improved. Therefore, a better control performance can be achieved. The described methodology provides clear, easy implementable and automated design criteria for the blade pitch controller. More importantly, it takes into account both stability and performance of the FOWTs and does not add new sensors. This allows for similar dynamic step response behavior, i.e., overshoot, rise time and settling time across the operating points. At the same time, the stability of the control system is ensured. This control design method originates from the paper [63] and is further optimized in this chapter. The developed design criteria are important for system engineering or control co-design, where the controller is adapted during the FOWT design, which will be discussed in Chapter 6. The chapter begins with the current challenges of using the state-of-the-art blade pitch controller for FOWTs. This is followed by the considerations for the control design in this thesis, including the benefit of adding a TLMCD. After that, the design procedure of the controller is detailed, utilizing the established linearized coupled SLOW model and specifically adapted for a TLMCD-stabilized FOWT. Finally, the performance assessment is conducted on two different 10 MW FOWTs, employing the nonlinear explicitly coupled SLOW model.

## 5.1 Engineering Design Solutions

Section 2.4 has already discussed the non-minimum phase behavior of a FOWT. Poor design of the blade pitch controller can lead to unstable behavior in the control system. As a result, implementing a SISO controller requires a time-consuming tuning procedure that is dependent on both the turbine and floater. The work presented in [43, 64] has reduced the closed loop natural frequency below the floater pitch natural frequency, so that the stability margins meet the requirements. However, the control performance is significantly degraded. The trade-off between the control performance and the system stability margins has been carried out based on graphical analysis, as well as coupled simulation in [21]. Therefore, finding a compromise between control performance and stability margins becomes essential for control design.

In [65], an improved stability-oriented gain scheduling method was introduced. Instead of simply reducing the control bandwidth, a constant sensitivity margin of the open loop transfer function across the operating points is used to achieve a better compromise between stability and control performance. With the study case of the DTU 10MW reference turbine [51], it is found that the stability issue is no longer a critical factor above a wind speed of 19 m/s. Hence, the authors use the time constant of the closed loop control system as a design indicator at higher wind speeds. This approach addresses both of the stability and performance criteria for the first time. However, the time constant, which indicates the performance criterion, results from a brute-force search based on time simulations. At higher wind speeds, the drive-train rotation mode of the FOWT is highly overdamped, making it difficult to characterize the control performance using only the time constant  $\tau$ . Even with a constant  $\tau$ , the step response to wind excitation may vary, depending on the operating wind speed.

Therefore, it is necessary to develop general design criteria for the blade pitch control of FOWTs, which are independent of turbine and floater characteristics. In particular, when a FOWT is installed with a TLMCD, additional damping will improve the plant dynamic characteristics and reduce the control design challenge. This implies that a re-tuning procedure is necessary to improve the overall system responses. Furthermore, due to the strong coupling effect between the controller

and the floater, integrating the controller design into the substructures optimization becomes more important. Given these requirements, all of the above mentioned state-of-the-art approaches may be inadequate.

## 5.2 Quantification of Design Criteria

With the additional damping contributed by the TLMCD, the performance of the blade pitch controller, which is limited by the negative aerodynamic damping, can be improved. How to qualify the stability margin and the step response performance during the design procedure is discussed in this section. The benefits of the TLMCD and well as how this improvement can be incorporated into the controller of the FOWT are demonstrated.

### 5.2.1 Closed loop SISO control system

A simple control loop of wind turbines consists of a plant (dynamic system), which can be represented by a transfer function in the complex  $s$ -plane, and a SISO feedback controller. As is shown in Figure 5.1,  $G$  and  $K$  are notations for the plant and the controller, respectively.

The classical layout of the original controller is a standard PI controller using the generator speed error as input and the blade pitch as output [9]. The transfer function of the controller is written as

$$K(s) = k_p + \frac{k_i}{s}, \quad (5.1)$$

where  $s$  is the Laplace variable,  $k_p$  and  $k_i$  are the proportional and integral gains of the PI controller respectively. Instead of calculating the demanded generator torque to maintain a constant power, the generator torque in this work is kept constant [43] for above rated wind speeds. This strategy differs from the one used for most onshore turbines where the control objective of which is constant power. This is due to the fact that the instantaneous rotor speed required by the constant power has a negative impact on the fore-aft dynamics. The gains are scheduled for each operating point, characterized by the proportional gain  $k_p$  and the integral gain  $k_i$

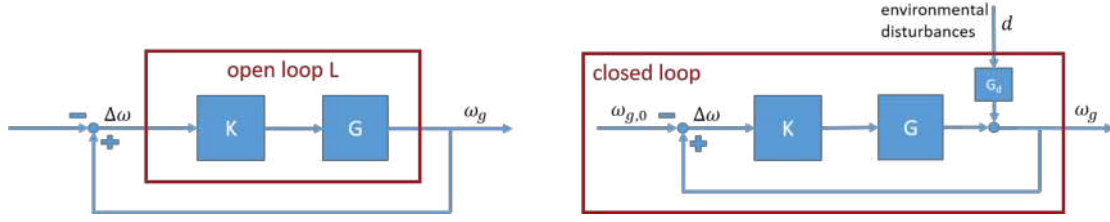


**Figure 5.1:** The open loop (left) used for stability analysis and the closed loop (right) used for performance quantification. Be aware that the control parameters here should be negative. Alternatively positive feedback can be used.

as functions of the blade pitch angle  $\theta$ .

When the control loop of the dynamic plant is closed, as shown in Figure 5.1, the output  $Y(s)$  in the frequency domain is determined by

$$Y(s) = \underbrace{\frac{G(s)K(s)}{1 + G(s)K(s)}}_T R(s) + \underbrace{\frac{1}{1 + G(s)K(s)}}_S G_d(s)D(s), \quad (5.2)$$

where  $G(s)$  and  $K(s)$  are the plant and the controller respectively. The reference generator speed  $\omega_{g,0}$  is denoted by  $R(s)$ . While  $D(s)$  represents the environmental disturbances such as wind and waves. In addition, the transfer function  $G_d$  determines the variation of the generator speed caused by external disturbances. The sensitivity, denoted by  $S$ , describes how sensitive the output is to the disturbances. While the complementary sensitivity  $T$  represents how well the system can track the defined reference value, i.e. the target generator speed for wind turbines. Since the sum of  $S$  and  $T$  is one, it is clear that the reference tracking is in conflict with the disturbance rejection.

### 5.2.2 Quantification of stability

The stability of the blade pitch control loop is crucial to the overall performance and safety of the FOWT system. Due to the strong coupling between the platform pitch motion and the aerodynamics, a poorly designed blade pitch controller can excite platform motion response and increase the structural loads, ultimately leading to system failure in the presence of instability. Furthermore, to account for uncertainties in the engineering model, a certain level of robustness is required

in the control loop of a FOWT system. For instance, the hydrodynamic damping, which is a sensitive factor for control loop stability according to [21], varies across different sea states and is difficult to determine accurately. Given this challenge, a sufficient stability margin is then necessary to ensure the system stability.

Industrial specifications provide several rules of thumb for quantifying the closed loop stability. The Nyquist stability criterion is one of the widely used methods, which is based on the frequency response of the open loop transfer function  $L(s)$ :

$$L(s) = G(s)K(s). \quad (5.3)$$

Looking at Equation 5.2, it is clear that the output  $Y(s)$  becomes infinite when  $L(s) = -1$ , which means  $(-1, 0)$  is an unstable point. According to the Nyquist criterion, a system without poles at the RHP becomes unstable, when the contour line of the open loop system  $L(s)$  encircles the critical point  $(-1, 0)$  in the complex plane. To ensure the closed loop stability, the  $L(s)$  contour should not only exclude  $(-1, 0)$ , but also maintain a certain distance from  $(-1, 0)$  that allows for a sufficient robustness. To quantify how far the nominal loop is located from the instability, it is common to use the nominal sensitivity peak  $M_s$ , with  $1/M_s$  describing the closest distance from the nominal open loop frequency response to the critical stability point  $(-1, 0)$ . Therefore, the larger  $M_s$ , the closer the closed loop is to the instability point. According to [65], the distance  $1/M_s$  decreases as  $k_p$  increases, indicating the decreasing robustness of the closed loop system. The threshold criterion of  $1/M_s = 0.4$  is selected in [65]. The same threshold is used here. However, instead of aiming for a constant sensitivity margin, it is only used as a constraint to ensure a certain robustness, i.e.  $1/M_s \geq 0.4$ .

An example of how sensitivity changes with control gains is presented in Figure 5.2. The case shown uses the OO-Star 10MW FOWT design, operating at a mean wind speed of 16 m/s. The integral time constant  $T_i$  is kept constant, while different proportional gains are selected. The distance to the point  $(-1, 0)$  are given in red text. The subplots compare the two systems with and without a TLMCD, i.e. a reference system without TLMCD on the left and a TLMCD stabilized system on the right. According to the reference system,  $1/M_s$  decreases with increasing  $k_p$ , indicating the decreasing robustness of the closed loop system. Considering the

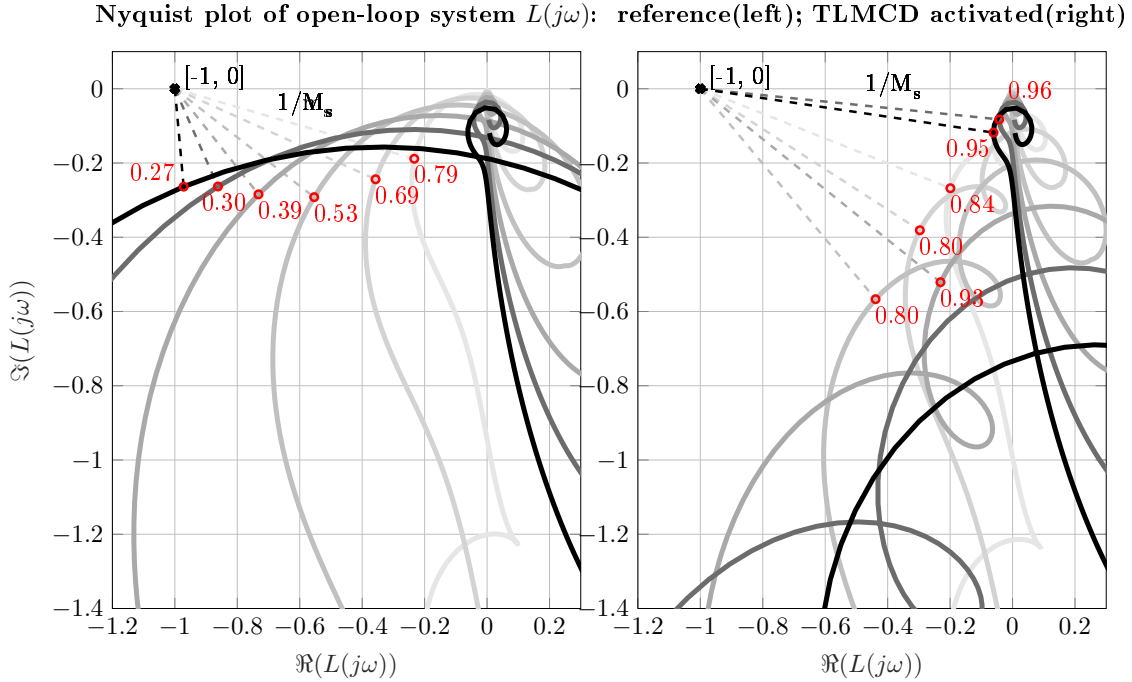


**Figure 5.2:** Nyquist plot of open loop transfer function  $L(s)$ : OO-star design with constant  $T_i$  ( $T_i=8$ s) and varying  $k_p$  (value increases when the darkness increases) at wind speed 16 m/s, with indication of the stability measure  $1/M_s$  in red.

criterion  $1/M_s \geq 0.4$ , some of the higher gains do not meet the stability margin requirements. When the FOWT is installed with a TLMCD, the values of  $1/M_s$  are significantly increased for the same control gains, so that  $1/M_s \geq 0.4$  is no longer a control limitation. This proves that the TLMCD can improve the dynamic behavior of the system by increasing the stability margin.

### 5.2.3 Quantification of control performance

The stability criterion only ensures a stable system behavior, which means the output of the control loop will always converge under variable disturbances. However, it does not quantify the control performance, i.e. how long does it take for the system to converge to a steady state, how large the oscillation amplitude is during the transient period. These are important factors that determine the system responses to environmental disturbances. To quantify the disturbance rejection capability, the



closed loop system is subject to a unit step wind, and its response is then analyzed. The required numerical model for onshore wind turbines typically includes only one DOF, i.e the drive-train rotation. In this case, the transfer function from wind disturbance to the generator speed, i.e., the output signal, is a second order system. Given the natural frequency  $\omega_0$  and damping  $\zeta$  characteristics of this second order system, the system dynamic step responses at different operating wind speeds are similar. This is called loop shaping and is generally a common design procedure for onshore turbines.

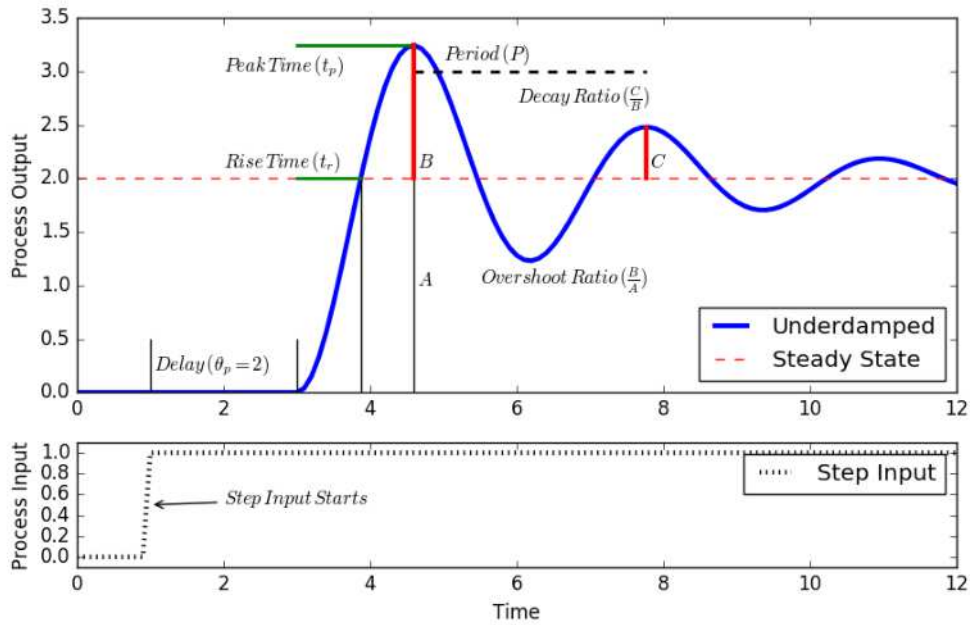


**Figure 5.3:** Different performance indicators are shown for a typical step response of a second order system with complex poles<sup>†</sup>.

The standard form of the transfer function of a second order system with infinite zero is

$$G(s) = K \frac{\omega_0^2}{s^2 + 2\zeta\omega_0 s + \omega_0^2}. \quad (5.4)$$

When the system is subjected to a step disturbance, it will eventually reach a steady state. To quantify the system responses, several indicators can be used

<sup>†</sup><https://apmonitor.com/pdc/index.php/Main/SecondOrderGraphical>. Accessed on 05.Nov.2022.

to characterize the dynamic behavior, as shown in Figure 5.3. These include the overshoot  $M_{pt}$ , the rise time  $T_r$ , the peak time  $T_p$  and the settling time  $T_s$  sec.

Depending on the roots of the characteristic equation  $s^2 + 2\zeta\omega_n s + \omega_n^2 = 0$ , there are three different cases, i.e. an underdamped system when  $\zeta < 1$ , a critically damped system when  $\zeta = 1$ , and an overdamped system when  $\zeta > 1$ .

In the case of an underdamped system, the settling time  $T_s$  (assuming 2% of the settled steady response), rise time  $T_r$ , peak value  $M_{pt}$  and the corresponding overshoot ratio can be determined by:

$$\begin{aligned} T_s &= \frac{4}{\zeta\omega_0}, \\ T_r &= \frac{\pi - \tan^{-1}(\sqrt{1 - \zeta^2}/\zeta)}{\omega_0\sqrt{1 - \zeta^2}}, \\ M_{pt} &= 1 + \exp(-\zeta\pi/\sqrt{1 - \zeta^2}), \\ \text{overshoot } \% &= (M_{pt} - 1) \cdot 100 \end{aligned} \quad (5.5)$$

As can be seen, these performance criteria are all functions of  $\omega_0$  and  $\zeta$ . This also explains the reason for designing a scheduled onshore blade pitch controller by defining  $\omega_0$  and  $\zeta$  for the above rated operating range. This ensures a similar step response for different operating wind speeds. Assuming that  $\omega_0 = 0.1$  rad/s and  $\zeta = 0.7$ , which are common design parameters for onshore turbines, the corresponding  $T_r$  and  $T_s$  are 32.9 s and 57 s, respectively.

In the case of an overdamped system, the step response does not oscillate with a certain frequency, the settling time  $T_s$  (within 2% of the steady response) is calculated by solving the equation:

$$0.02 = \frac{s_2}{s_2 - s_1} e^{s_1 T_s} + \frac{s_1}{s_1 - s_2} e^{s_2 T_s}, \quad (5.6)$$

where  $s_1 = -\zeta\omega_0 + \omega_0\sqrt{\zeta^2 - 1}$ ,  $s_2 = -\zeta\omega_0 - \omega_0\sqrt{\zeta^2 - 1}$  are the roots of the characteristic equation.

How step responses change with control gains is presented in Figure 5.4. As shown, when  $T_i$  is constant, a relatively large  $k_p$  improves the ability of disturbance rejection, shown by smaller overshoot, shorter rise time, and shorter peak time. However, the settling time is increased. It takes longer for the system to reach

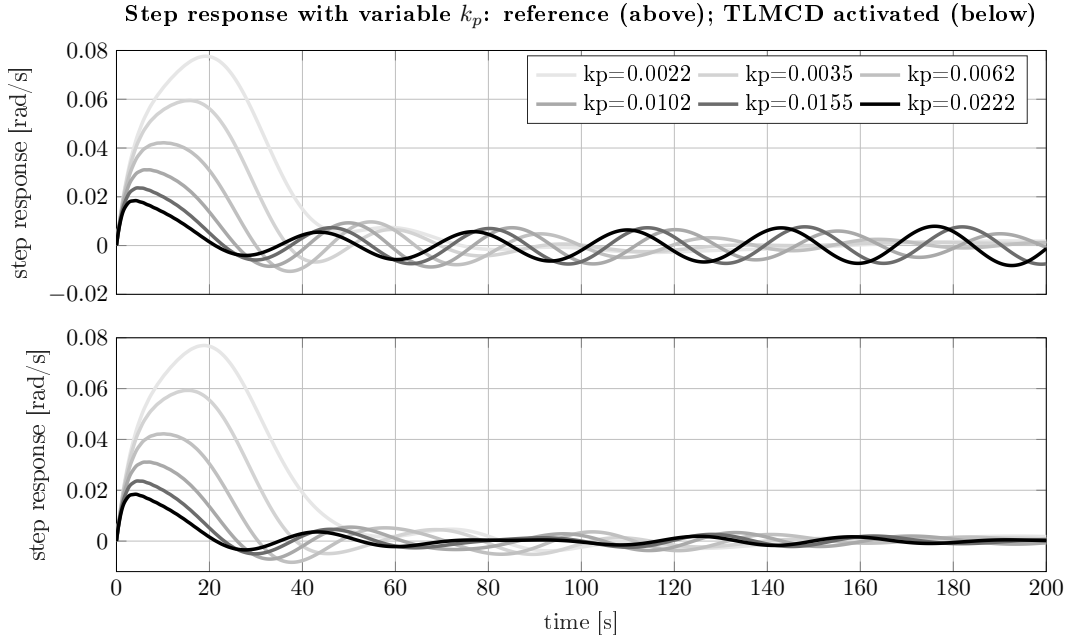


**Figure 5.4:** Step response of generator speed to unit step wind with different control gains at 14 m/s,  $k_p$  increases with the color darkness increases.

the steady state after a step disturbance, which is equivalent to the situation when a system has insufficient damping. Combining the observations on the sensitivity margin in Figure 5.2, it can be concluded that an improvement in generator speed control can be achieved at the expense of stability. This is also reported in [21] as a trade-off between the generator speed regulation and platform pitch motion, which is found by studying a 5 MW FOWT. By comparing the above and below subplots of Figure 5.4, the impact of the TLMCD can be inferred. First of all, the TLMCD does not change the response to the step wind within around 40 s. This is mainly dominated by the aerodynamics, since the turbine and control parameters are the same, one can expect the same rise time and overshoot. After this period, the platform motion continues to oscillate due to the coupled dynamics, resulting in a longer settling time than onshore turbines. When the TLMCD is activated, the low damping caused by the higher  $k_p$  is partially compensated, so that the coupled dynamics of the platform motions are better damped.

Although the previously introduced control performances can be described analytically with a second order system, it may not be sufficient to capture the coupled dynamics of a FOWT. This is due to the fact that the FOWT system modes are highly coupled so that additional DOFs must be considered, which results in a higher order system with more poles and zeros (i.e. additional modes) in the transfer function. Among these DOFs, the platform pitch motion is particularly important as it is strongly coupled with the rotor aerodynamics. At lower wind speeds, the platform pitch motion can affect stability due to the negative aerodynamic damping, while at higher wind speeds, this becomes less critical because of the increased aerodynamic damping. Furthermore, the drivetrain rotation mode is overdamped due to the slow motions of the platform. These unique characteristics distinguish a controller for FOWTs from that of onshore turbines. Depending on the mooring design, the surge motion may also be important and should be considered in controller design. Section B provides a detailed study of the influence of additional DOFs on the dynamic responses, as well as the impact of the model fidelity choice on control design. It can be concluded that the inclusion of more DOFs can improve the accuracy of performance quantification, but it can also result in a very complex transfer function, making it challenging to formulate an analytical solution.

In this work, a linear model with seven DOFs is selected for the control design. In the case of adding a TLMCD with three columns, two additional DOFs must be added. As a result, the control performance cannot be determined analytically. Therefore, direct time simulations under unit wind disturbance are performed to obtain these performance indicators, including overshoot, settling time, and peak time, which are determined for each control parameter. In addition to the step response from wind to generator speed, the response from wind to platform pitch is also considered as a performance indicator. For this, the settling time threshold is increased to 10%. Since the more DOFs there are, the more oscillations there are due to the coupling effect, the slower the system settles. There are always small oscillations that are not primarily caused by the controller but by the coupled dynamics of the FOWT. If a threshold of 2% is used, the settling time reaches several hundred seconds, especially when the surge DOF of a centenary moored FOWT is activated, whose natural period is often over 100 s. In such cases, comparing the settling time does not reflect the performance of the blade pitch controller.

## 5.3 Control Design Procedure

Combining both criteria, the stability and step response behavior criteria, requires the consideration of multiple indicators. This is similar to an optimization problem with multiple objects and constraints, which can be complex and chaotic without good prioritization and workflow. How to integrate and coordinate between these criteria to find the most suitable controller for the FOWT system becomes essential. Figure 5.5 shows the design procedure used in this work. In general, it can be divided into two stages, i.e., a pre-processing stage where a database of performance quantifications is created by changing the control parameters. In the second stage, a workflow applies these criteria and searches for the suitable control parameters with predefined constraints and objectives.

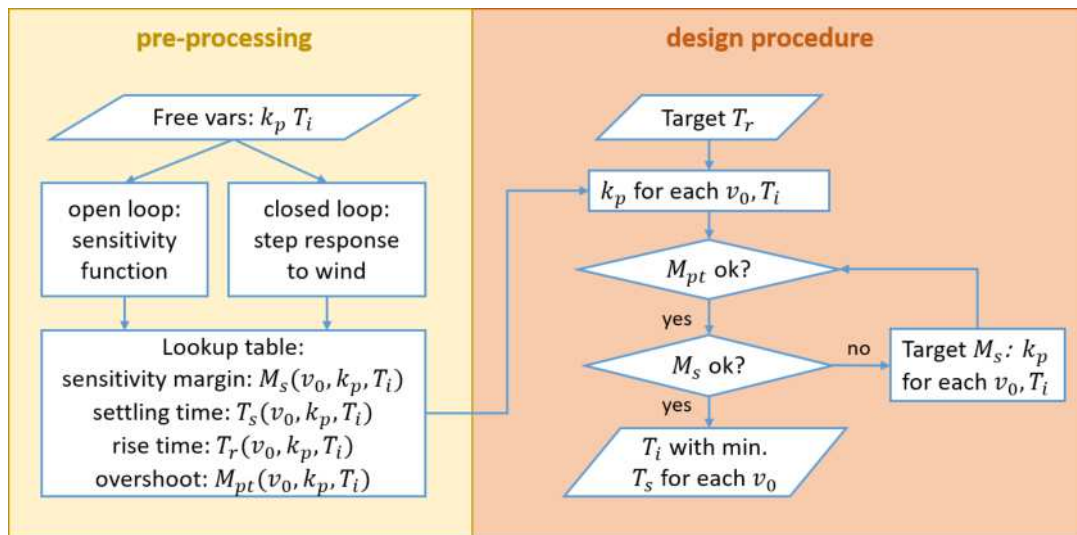


**Figure 5.5:** Workflow of the controller design.

For the database, the first step is to define a design space of control parameters  $k_p$  and  $T_i$ . Then the corresponding controllers, described by transfer functions, can be generated. After connecting to the linear models at different operating points of the FOWT, open loop and closed loop systems can be prepared for further analysis. By analyzing both the open loop and closed loop system, a 2D lookup table is established, which stores the indicators for each combination of control gains  $k_p$  and  $T_i$ . For evaluating stability, the sensitivity margin  $M_s$ , introduced in Section 5.2.2,

is the only indicator. While for step response performance, the rise time  $T_r$ , settling time  $T_s$  and overshoot  $M_{pt}$ , introduced in Section 5.2.3 are used for the design evaluation.

The workflow begins by determining the proportional gain  $k_p$  for each mean wind speed  $v_0$  and integral time constant  $T_i$  that allows a constant desired rise time  $T_r$ . This step yields a subset of combinations of  $k_p$  and  $T_i$  for each mean wind speed. The overshoot is set as a constraint, which should be kept below 15%, i.e.  $M_{pt} \leq 1.15$ . The same with the sensitivity margin,  $M_s \geq 0.4$  should be fulfilled for this subset of control parameters. For those combinations within the subset, which meet the overshoot requirement but not the stability requirement, the proportional gain  $k_p$  is chosen primarily to satisfy the stability requirement. If neither  $M_{pt}$  nor  $M_s$  meets the requirement, the current  $T_i$  is eliminated. At this stage, for each operating point  $v_0$ , there may still be multiple combinations of  $k_p$  and  $T_i$  that satisfy all of the predefined design constraints. To determine a unique combination of control gains for each  $v_0$ , the minimum settling time  $T_s$  is targeted. Finally,  $k_p$  and  $T_i$  are found for each wind speed.

## 5.4 Evaluation of the Control Design Method

In this section, two TLMCDs will be designed and simulated on two of the state-of-the-art 10 MW FOWTs with two different floaters. The automated control adaptation, developed in this chapter, is then evaluated. The numerical tool used here is the explicitly coupled TLMCD and SLOW model, introduced in Section 3.6.

### 5.4.1 System Parameters and Load cases

The 10 MW FOWTs use the OO-Star floater design and the Nautilus-10 floater design, the definitions and essential parameters of which are given in Section 2.6. The TLMCDs are designed to fit into the vertical columns and connecting pontoons, as illustrated in Figure 5.6. As can be seen, for the Nautilus-10, the horizontal arms of the TLMCD are not fitted inside the platform, but are attached to the FOWT as additional pontoons. This is due to the limitations of the numerical tool developed. As the focus of this chapter is on the controller, simpler design criteria

are used, as listed below:

- The geometry of the TLMCD fits into the OO-Star substructure, with the horizontal arms merged into the Y-shaped pontoons.
- The natural frequency of the TLMCD is identical to the FOWT pitch natural frequency.
- The fluid mass inside the TLMCD is below 5% of the total mass of the FOWT.
- The resulting metacentric height considering the influence of free surface of the TLMCD is above 0.8 m.

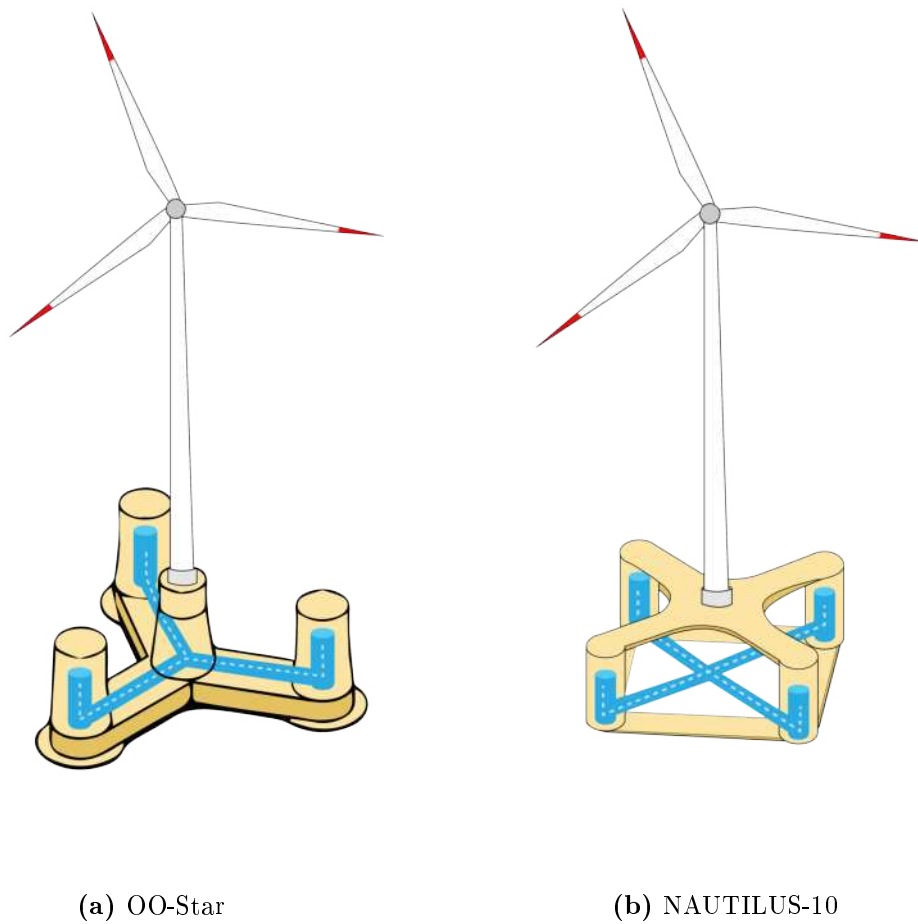


**Figure 5.6:** Design and installation of the TLMCDs for the two state-of-the-art FOWTs.

The load cases selected for the evaluation are based on the site condition from

the project LIFES50+ [66]. The key environmental parameters, mean wind speed, significant wave height, as well as wave peak period are listed in Table 5.1. Since the focus of the control redesign lies on the blade pitch controller, only wind speeds above rated are used.

**Table 5.1:** Environmental conditions for operational load cases.

Mean wind speed $\bar{u}$ [m/s]	12	14	16	18	20	22	24
Significant wave height $H_s$ [m]	2.6	3.1	3.7	4.3	5.2	6.2	7.6
Wave peak period $T_p$ [s]	8.7	9.5	9.8	10.1	11.3	12.4	12.2

As the established design criteria are relatively straightforward, multiple TLMCD designs align with these criteria. The implemented TLMCD is chosen from the design space that fulfills all criteria and is characterized by its geometric parameters listed in Table 5.2.

**Table 5.2:** Parameters of the TLMCD used for the 10MW FOWTs.

Parameter	OO-Star	Nautilus-10
Vertical column height $L_v$ [m]	20	15
Vertical column diameter $D_v$ [m]	3.15	2.54
Horizontal arm diameter $D_h$ [m]	1.25	1.10
Horizontal arm length $L_h/2$ [m]	37	38.89
Head loss coefficient $\eta$ [-]	3	4.5
Natural period [s]	32	30
Total fluid mass [t]	618.90	463.16
Mass ratio [%]	2.94	5
Vertical location of the streamline origin $e$ [m]	-32	-17.36

#### 5.4.2 Brute force optimization of control design criteria

Although the workflow to determine the control gains is established, it is still an open question which  $T_r$  will result in improved system response. In [63], the authors define  $T_r$  slightly below the platform pitch natural period, which is based on a qualitative assessment of several simulations. Hence,  $T_r$  is kept constant over all the



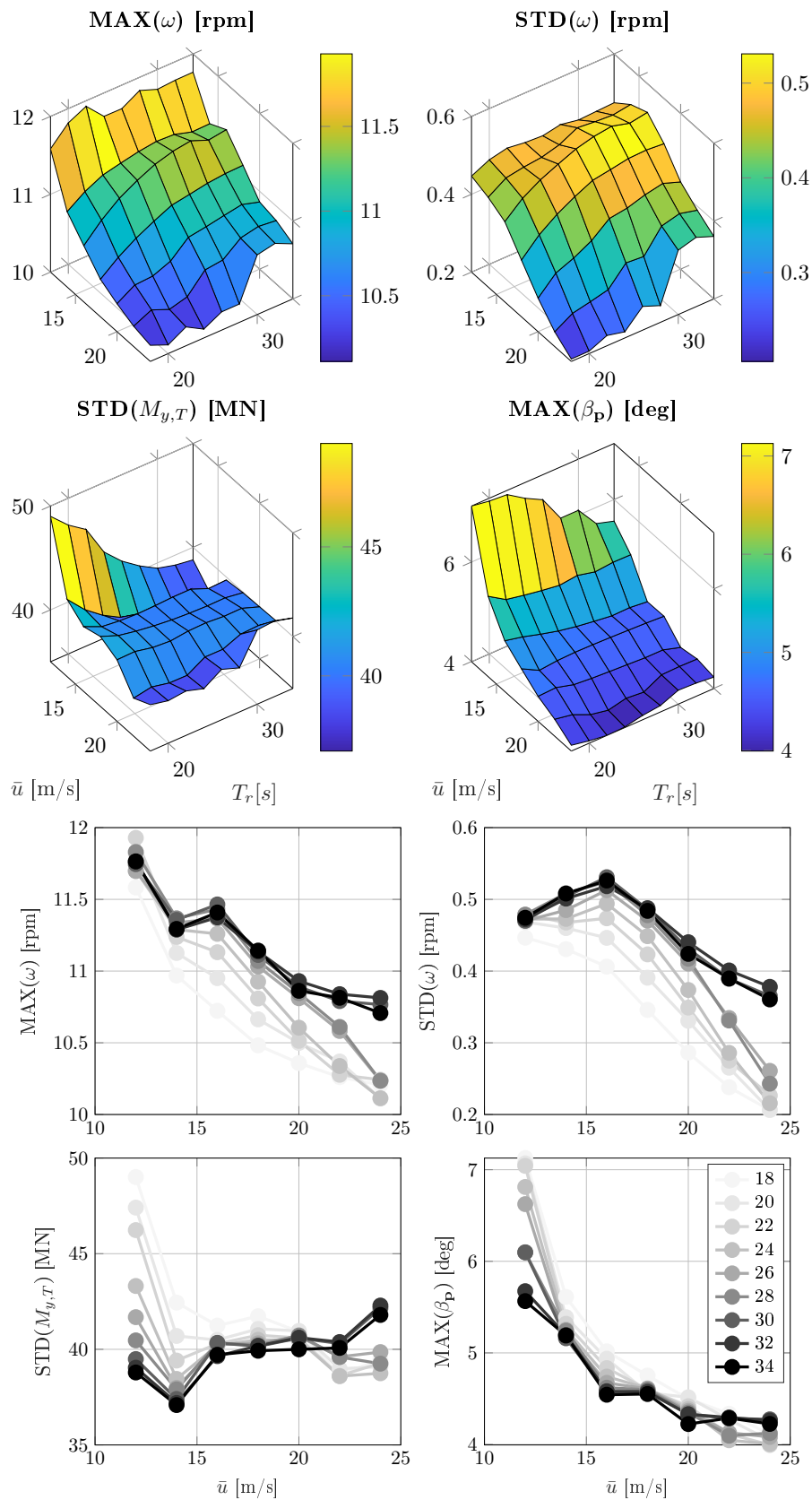


**Figure 5.7:** System statistical responses of the OO-Star FOWT with TLMCD stabilization change over mean wind speed  $\bar{u} = 12 \dots 24$  m/s and design parameters  $T_r = 18 \dots 34$  s ( $T_r$  is constant for all wind speeds).

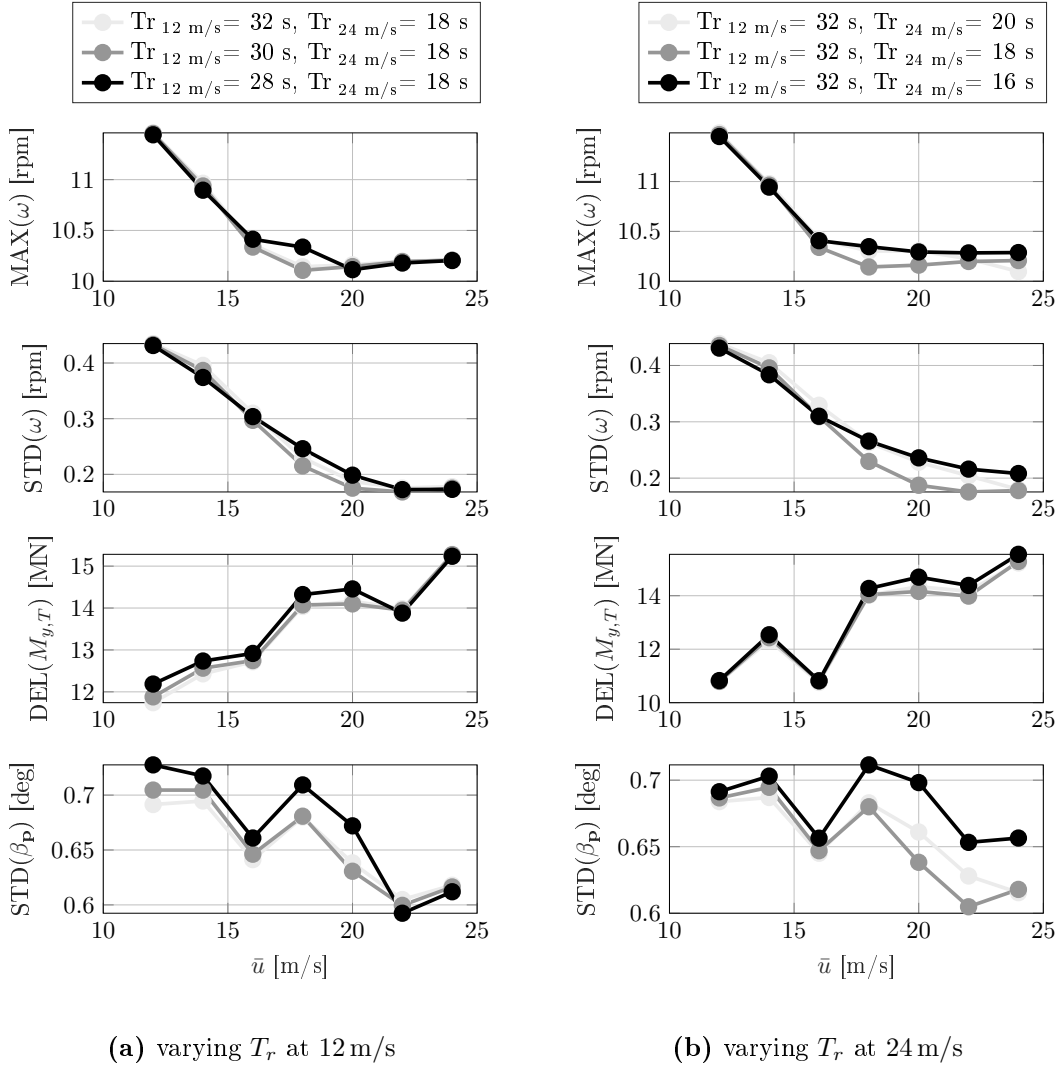
wind speeds. With this design criterion, there is no significant benefit in terms of the overall system response compared to the stability oriented controller in [65]. It is still worth investigating how to improve the control performance by optimizing  $T_r$ , which is carried out in this section. For this purpose, the OO-Star FOWT is used, and the resulting criteria are later applied unchanged to the Nautilus-10 FOWT.

Figure 5.7 provides an explanation how the design parameter  $T_r$  affects the system response. It illustrates how the dynamic response of the OO-Star FOWT changes over the design parameter  $T_r$ . As can be seen, four indicators are considered here and plotted in sub-figures, which are important parameters that affect the loads and platform motions. These are the maximum and the STD of the rotor speed  $\omega$ , which reflect the quality of the power production (as mentioned before, the generator torque is kept constant); the maximum platform pitch  $\beta_p$  and the Damage Equivalent Load (DEL) of the tower base bending moment in the fore-aft direction  $M_{y,T}$ .

Looking at the figures, several conclusions can be drawn. First, a smaller  $T_r$  always contributes to a more stable power production, shown by the smaller overshoot and STD. This stable behavior is more visible at higher wind speeds. At rated wind speed, where two controllers (blade pitch and torque) interfere with each other, this effect is almost invisible. Second, a smaller  $T_r$  will excite the motions and increase the loads. Again, this effect is only significant at lower wind speeds. When the wind speed is above 20 m/s, a smaller  $T_r$  is also beneficial for  $M_{y,T}$  and  $\beta_p$ . Finally, at the wind speeds in-between, the conflicting control objectives between the power production and platform motions becomes visible. One has to make a compromise between these two conflicting aspects.

Based on the above mentioned observations, a qualitative assessment can already be made. For the wind speeds close to the rated wind speed, a relatively large  $T_r$  should be selected, while for high wind speeds,  $T_r$  should be kept as low as possible. It should be mentioned that the range of  $T_r$  is not arbitrary. The design criteria and constraints in Figure 5.5 limit the choice of  $T_r$  for a particular FOWT design. As an example, [18 s, 34 s] is the permissible range, where one can find  $k_p$  and  $T_i$  for all wind speeds. Given these facts, the most straightforward solution is to optimize  $T_r$  for each operating wind speed by multiple simulations. This can be done if the controller design is only applied to a particular FOWT design. However, if the controller design is within an optimization framework where multiple FOWT designs

need to be evaluated, it will be very computationally expensive. Therefore, a more simplified approach is used here. Instead of optimizing the design criterion  $T_r$  for all operating points, only two operating points are considered in the optimization process, i.e. at 12 m/s and at 24 m/s). For the operating points in-between,  $1/T_r$  is assumed to increase linearly, which also allows a smooth transition between different operating points.



**Figure 5.8:** System response statistics change over mean wind speed  $\bar{u} = 12 \dots 24$  m/s with variable design parameters  $T_r$  ( $1/T_r$  increases linearly from 12 m/s to 24 m/s).

Following the simplified design criteria, a fine tuning of  $T_r$  at 12 m/s and 24 m/s)

are performed, which is based on multiple simulations results. Figure 5.8 shows the impact of choosing different  $T_r$  at 12 m/s (Figure 5.8a) and 24 m/s (Figure 5.8b). It becomes evident that varying the choice of  $T_r$  at 12 m/s has a large impact on the platform pitch motion response between 12 m/s and 20 m/s. It also influences the tower base bending moment. However, these impacts are invisible at higher wind speeds above 20 m/s. On the contrary, changing the value of  $T_r$  at 24 m/s mainly affects the dynamic response at higher wind speeds, in particular above 16 m/s. In summary, optimizing  $T_r$  can result in favorable system responses. However, considering the focus of this chapter, which is mainly on the design procedure itself, a detailed optimization of  $T_r$  has not been carried out for the particular floater design. Instead,  $T_{r,12m/s} = 32$  s and  $T_{r,24m/s} = 18$  s are selected for the numerical simulations in the following section. And the actual optimization of  $T_r$  will be carried out in the next chapter.

### 5.4.3 The resulting control design

Following the design workflow in Figure 5.5, the baseline blade pitch controller is designed for the public OO-Star 10MW FOWT design. The resulting control gains are plotted in Figure 5.9, including the reference controller marked with gray color, which is the stability oriented robust controller presented in [65].

As can be seen, the performance oriented control design has further reduced the control gains at lower wind speeds, while the gains at higher wind speeds are increased. This phenomenon is quite different from the onshore design, where the control gains decrease over wind speeds to ensure a constant overshoot  $M_{pt}$  and rise time  $T_r$ . This trend is very similar to the results in [63]. However,  $T_r$  was chosen according to the best practice in [63], i.e.  $T_r$  should be slightly below the natural period of the platform pitch, and  $T_r = 32$  s was used for all wind speeds. By optimizing  $T_r$ , control gains are further increased at higher wind speeds.

Figure 5.10 shows more details of the performance oriented controller, as well as the comparison to the stability oriented controller (will be referred as reference controller in the following discussion) and the case when the TLMCD is active. The discussion will first focus on the cases where the TLMCD is inactive. For the performance oriented controller, although the sensitivity margin  $M_s > 0.4$  is set as

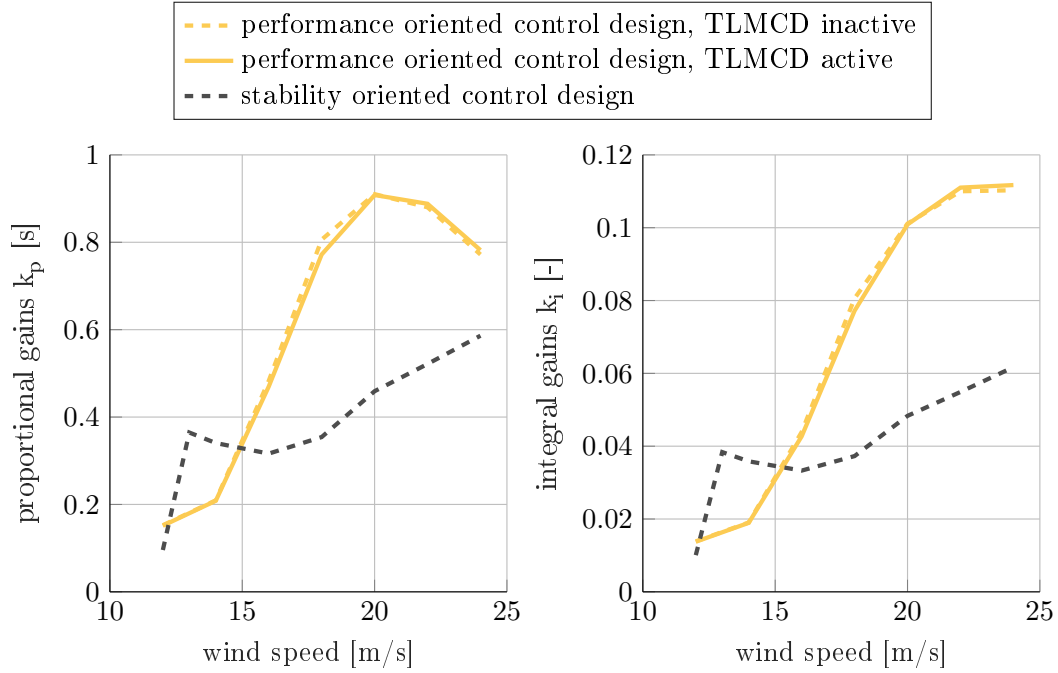


**Figure 5.9:** Proportional gains (left) and integral gains (right) at different wind speeds.

constraint,  $M_s$  is higher in most of the cases than that of the reference, indicating a higher robustness of the controller. Meanwhile, the settling time  $T_s$  is significantly decreased, which means that for the same unit disturbance, the performance oriented controller requires less time to reach a steady state. The only drawback is related to the overshoot, which is only slightly increased between 12.5 m/s and 15 m/s.

To understand better the impact of the TLMCD, a comparison is made between cases with and without TLMCD. In both cases, the reference controller remains the same, but the performance-oriented controller follows the previously described design procedure. The additional damping provided by the TLMCD results in slightly higher control gains as shown in Figure 5.10. The comparison of solid and dashed lines indicates that the TLMCD increases the sensitivity margin and reduces the settling time. Furthermore, the negative effect of the TLMCD on the overshoot, observed in the linear analysis in Figure 5.10, is not apparent in the coupled time simulations. Overall, these findings suggest that the TLMCD improves system performance by increasing stability margins and reducing settling time, without signif-

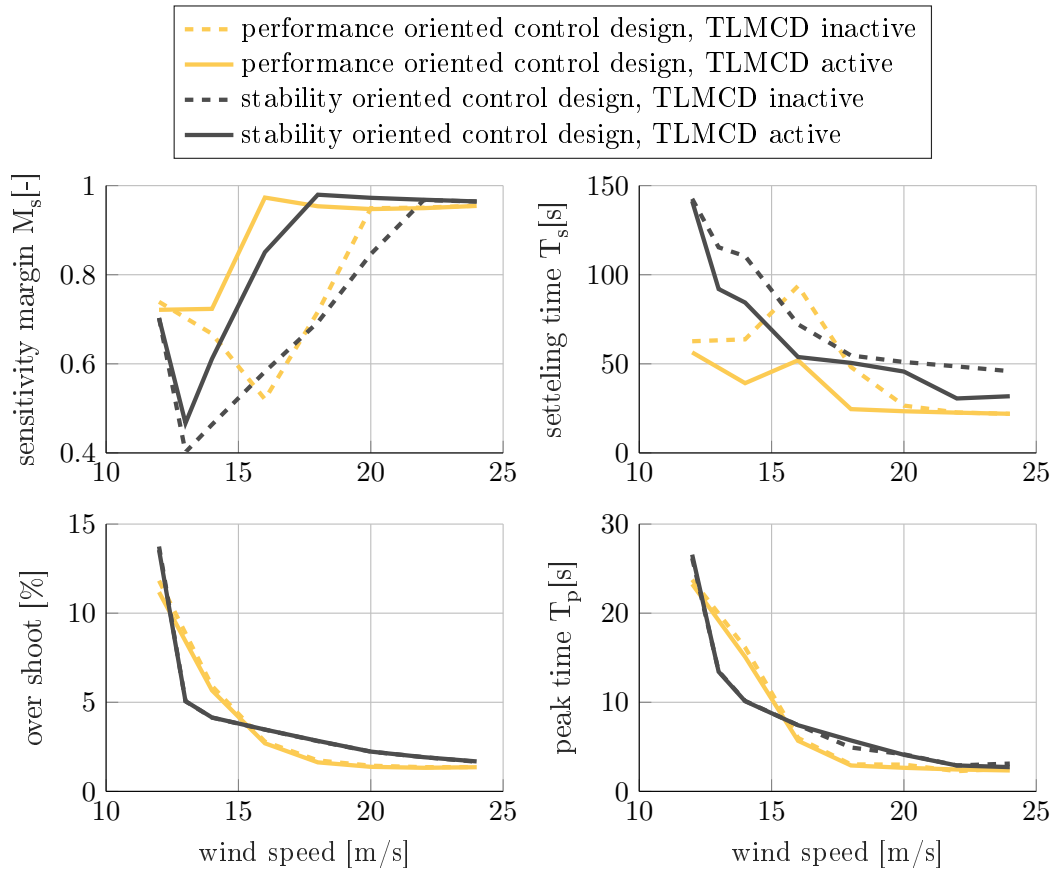


**Figure 5.10:** Control proportional gains (left) and integral gains (right) of the OO-Star FOWT for different wind speeds.

icantly impacting overshoot.

#### 5.4.4 Simulation results of design load cases

Like its linear counterpart used in the controller design, the nonlinear SLOW model employed for evaluation incorporates seven DOFs: platform surge, sway, heave, roll, pitch, tower top displacement, rotor speed. First order wave forces using potential flow theory and second order wave forces approximated by the Newman approximation are used. In addition, linear damping coefficients are used to ensure the same physical assumption between the models used for control design and evaluation. A quasi-static model is used to represent the behavior of the mooring lines. The load

cases used are listed in Table 5.1. The controller developed in Section 5.4.3 is applied to the FOWT, whose gains are plotted in Figure 5.9. A comparison between the cases with the TLMCD inactive and active is also given, which shows the impact of the TLMCD with different controllers.

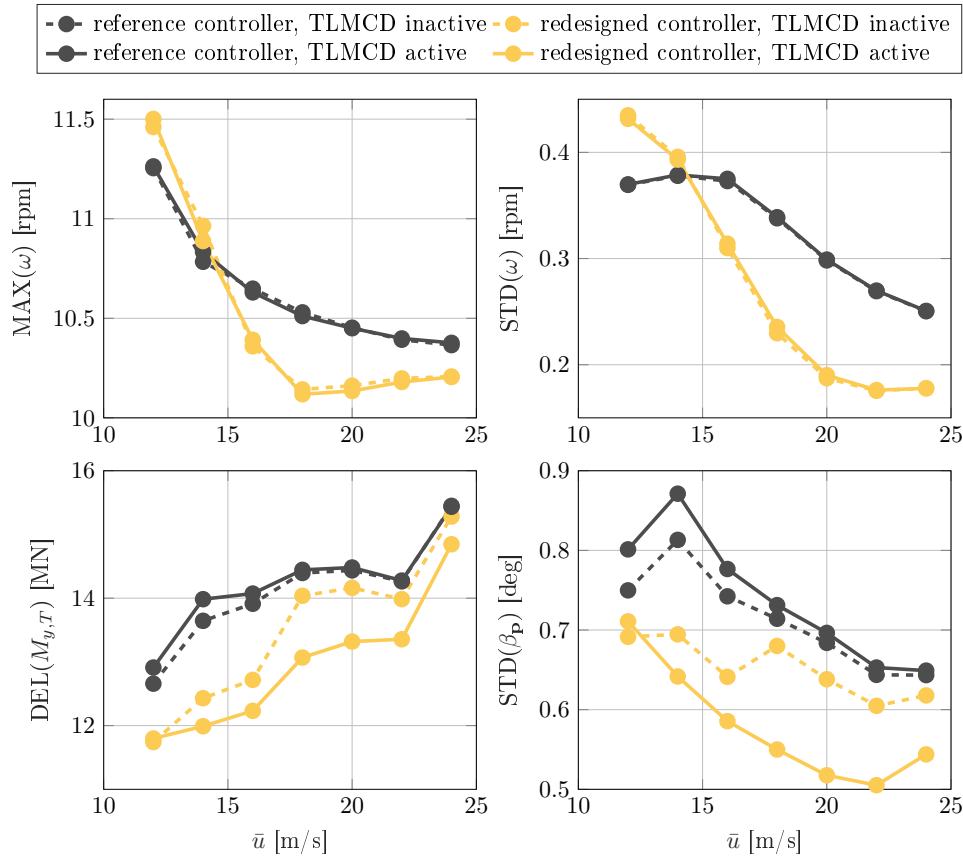


**Figure 5.11:** System statistical responses of the OO-Star DTU10MW FOWT with different controller and TLMCD setups at the above rated operation range.

The simulation results are presented in Figure 5.11 and Figure 5.12, where Figure 5.11 shows the absolute values of the system statistical responses and Figure 5.12 gives the normalized comparison. The reference here is the responses with the reference controller and deactivated TLMCD under stochastic wind and wave excitations. The details of this reference controller can be found in [65], including the simulation results and the comparison with other control strategies. In general, this reference controller already achieve a good balance between performance and

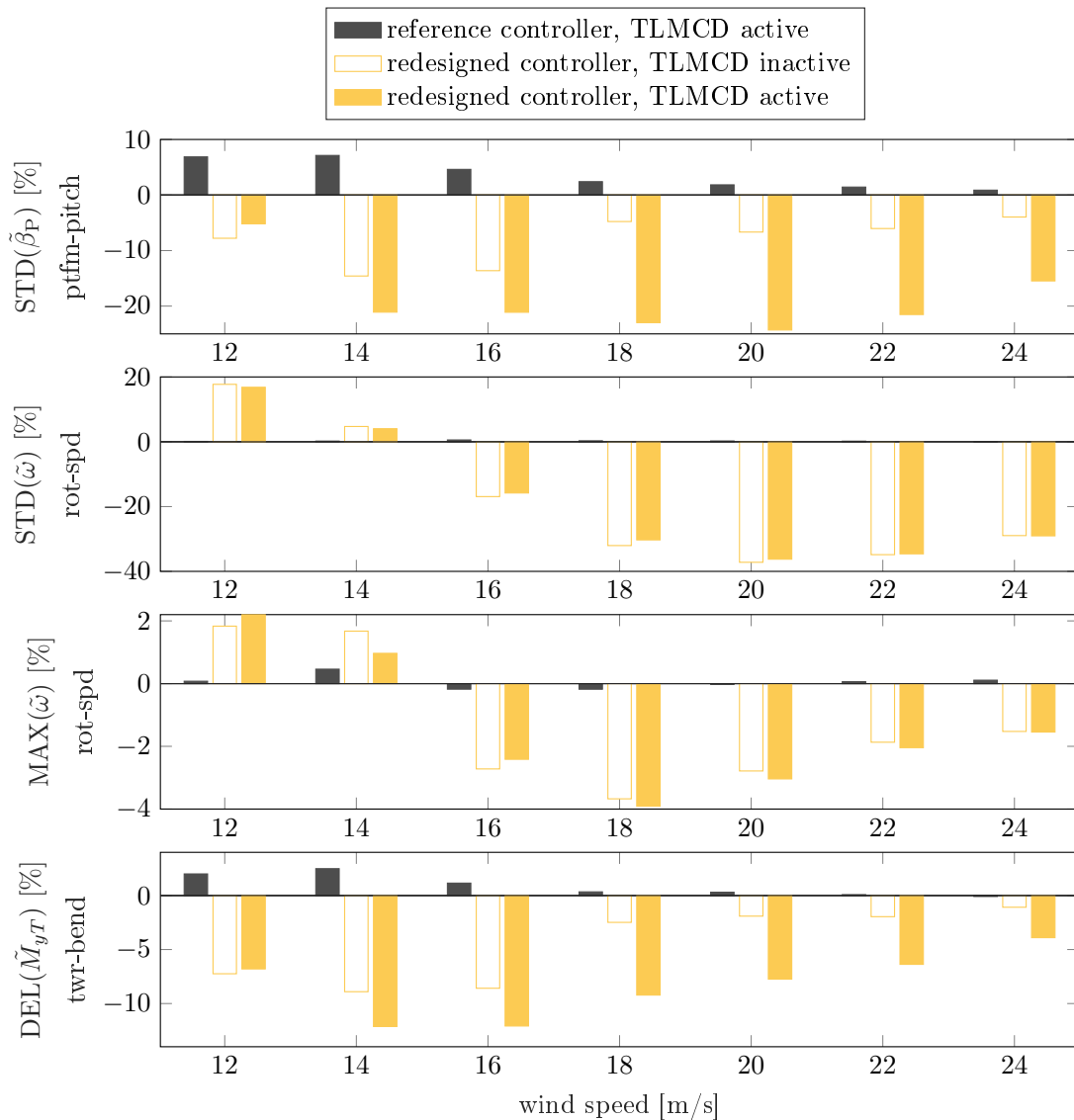


**Figure 5.12:** Comparison of relative system statistical responses of the OO-Star DTU10MW FOWT w.r.t. the case with a reference controller and without a TLMCD.

robustness. The response indicators include the maximum (MAX) rotor speed, the STD of rotor speed and platform pitch motion, and the DEL of the tower fore-aft base bending moment. Again, since the generator torque is constant for above rated operation, the rotor speed is a direct reflection of the power production quality.

Looking at the results, the first clear message is that system response is not always improved by simply adding a TLMCD. It was found in [40] that adding a



TLCD without adapting the blade pitch controller can only improve the platform pitch motion to a limited extent, about 4% in [40] for the TripleSpar [67]. As for the OO-Star FOWT analyzed here, instead of a limited improvement, the platform pitch motion and tower base bending moment even increased. This is clearly visible in the black bars in Figure 5.14, which represent the simulation results when the TLMCD is active but the controller remains unchanged. However, at the wind speeds close to the rated, the rotor speed is almost identical to the reference case.

As for the cases with the performance oriented controller, which is denoted as "redesigned controller" and marked in yellow in the plot, the power production quality is significantly improved at wind speeds higher than 15 m/s, up to ca. 40% reduction in STD, i.e. power fluctuation, but this is due to the controller redesign. The platform pitch motion and tower base bending are reduced as well. Here, a TLMCD can contribute to further motion and load reduction, especially at higher wind speeds.

At the rated wind speed, where the stability is critical, the performance oriented controller tends to stabilize the platform at the expense of the rotor speed regulation. Although the platform pitch motion and the tower base bending are reduced, the STD of the rotor speed is about 17% higher than that of the reference controller, while the overshoot is only slightly increased, i.e. by 2%. This trade-off phenomenon has been discussed in [21]. The responses can be improved by optimizing the controller parameters locally around 12 m/s. However, since the SISO PI controller is used, which does not fundamentally change this trade-off, any local optimization will only shift between the motion and speed control, rather than provide an overall better control design. Thus, as long as the overshoot limit is not exceeded, the control design can be accepted.

## 5.5 Influence of the FOWT Substructure Design

So far, we have introduced an automated control design procedure which shapes the step response for different operation points and for different system characteristics. It is shown that the synergy of the TLMCD and the blade pitch controller has a large impact on the system responses. If the controller is not carefully tuned, adding additional structural damping can lead to higher motion and structural loads, rather

than reducing them. These conclusions are drawn from the simulation results of the OO-Star design, which is relatively heavy and massive because of the concrete material used. However, one question remains: how does a TLMCD perform on a lighter steel floater? To answer this question, the same simulation study as in Section 5.4.4 is applied to the NAUTILUS-DTU10MW FOWT.

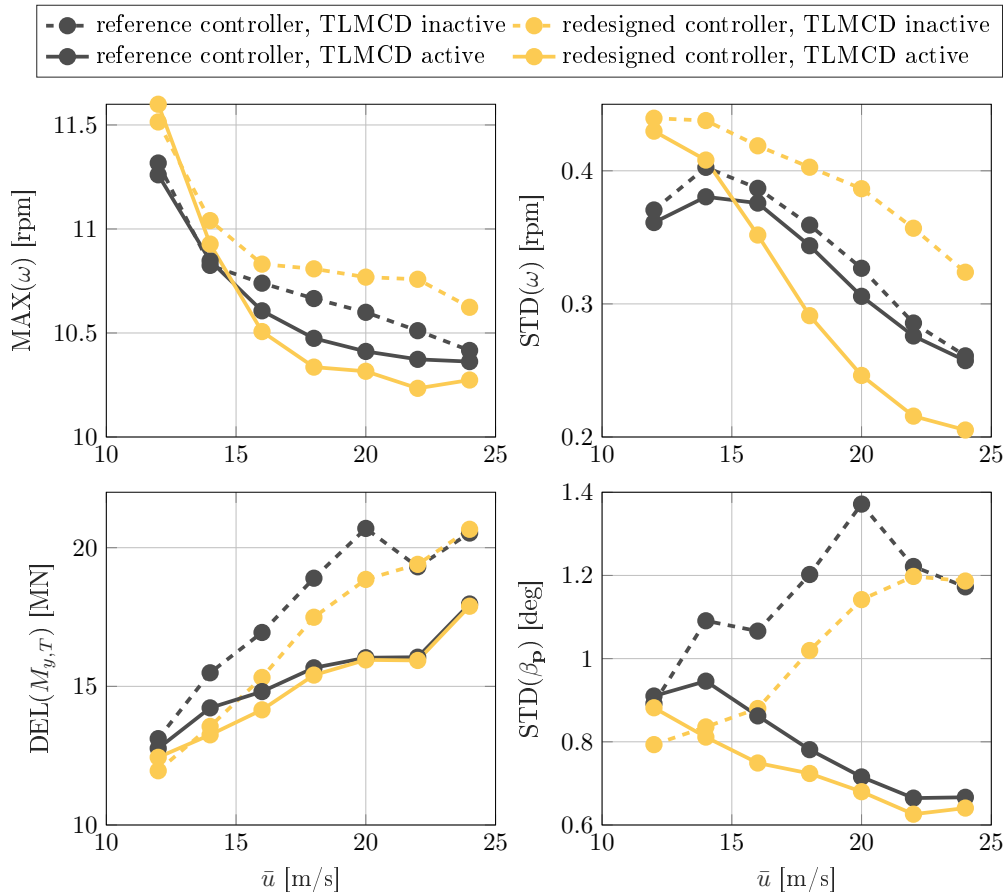


**Figure 5.13:** System statistical responses of the NAUTILUS-DTU10MW FOWT with different controller and TLMCD setups at the above rated operation range.

The installation sketch is shown in Figure 5.6 and the simulation results are presented in Figure 5.13. More details about the performance of the TLMCD and the controller can be found in Figure 5.14. Looking at the comparison of the statistical results, the overall conclusion is that the impact of a TLMCD on a lighter floater is more significant than that on the OO-Star design. This can be reasonably explained

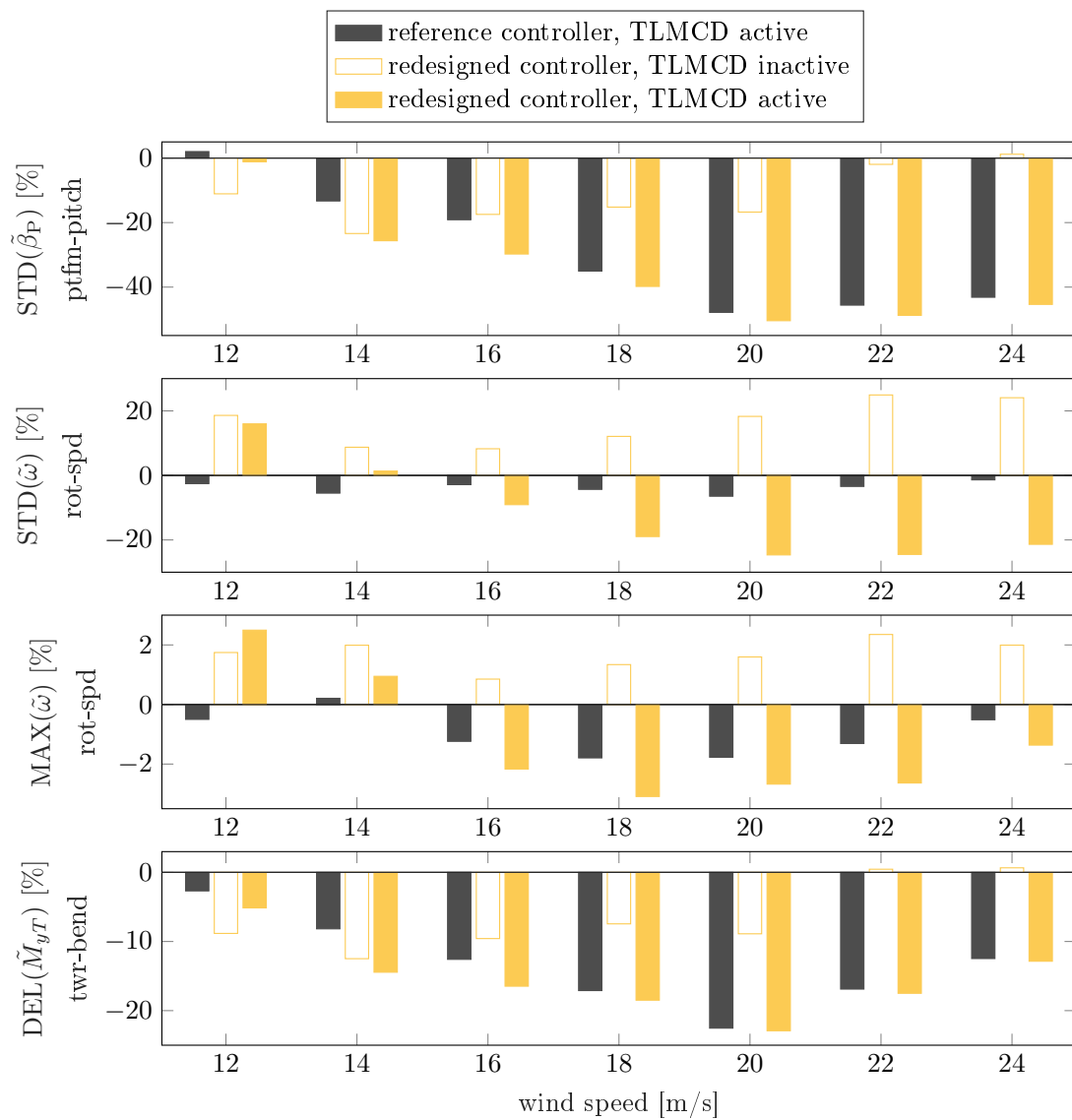


**Figure 5.14:** Comparison of relative system statistical responses of the NAUTILUS-DTU10MW FOWT w.r.t. the case with a reference controller and without a TLMCD.

by the size of the platform. Since the NAUTILUS-10 design uses mainly steel, it results in a much lighter platform that has relatively larger motions under the same environmental condition. It should be emphasized here that the total displaced water volume of the NAUTILUS-10 design is less than 9 tons, while FOWTs with concrete semi-submersible platforms for 10MW wind turbines can have a total displaced

water volume around or even higher than 20 tons<sup>†</sup>.

The primary object is to understand the impact of the TLMCD. In both cases, i.e. with the reference controller and with the redesigned controller, the TLMCD can, in both cases, damp the pitch motion and reduce the tower base bending moment, especially at higher wind speeds. This is different from the results with the OO-Star design, where the TLMCD is not able to improve the power production quality. Next, the focus is on the synergistic performance of the blade pitch controller while the TLMCD is active. Although adapting the controller can slightly improve the system response, as can be seen by comparing the yellow and black solid lines, this is however not as important as for the OO-Star design.

To summarize, the performance of the TLMCD and its interaction with the blade pitch controller can vary significantly, depending on the floating substructure. Even with identical design considerations, the resulting system response can differ substantially, as can be seen by comparing the TLMCD performance on the OO-Star FOWT and the Nautilus-10 FOWT. Therefore, adding structural damping to an actively controlled system can be highly complex. This realization leads us to the next chapter, where integrated optimization is employed to maximize the synergy between the coupled subsystems. This involves considering the effects of the substructure design, the added damping and the active control system, to ensure a favorable overall system performance and response.

---

<sup>†</sup>The statement about the weight and motion responses here is qualitative and general, it does not imply which platform material is superior to the other.

# 6 TLMCD-aided Control Co-Design Optimization

Previous work has demonstrated that a TLMCD has the potential to decrease the motions and loads of a FOWT. However, the effectiveness of this technology depends on its synergy with the blade pitch controller and its interaction with the substructure dynamics. This chapter investigates the limits of the TLMCD's contribution to the reduction of motions and loads of the FOWT system by framing it as an optimization problem. The ideas presented in this chapter are based on [68]. To achieve the best possible outcomes, an optimization framework that incorporates Control Co-Design (CCD) is devised to optimize the substructure's design, the TLMCD, and the blade pitch controller. By coordinating the function of these subsystems, the framework aims to achieve the best possible compromise to meet the objectives.

## 6.1 Optimizer, Design Space and Cost Model

This section outlines the preparation phase for developing an optimization framework, which involves defining the design space and constraints, setting up a cost model, and configuring the optimizer. These steps are critical for ensuring that the optimization process is well-defined, and that the all subsystems can be optimized to meet the desired objectives while staying within the constraints.

### 6.1.1 Design space

Optimizing the FOWT system involves multiple subsystems, including the substructure, blade pitch controller, and TLMCD. In order to reduce computational complexity, the number of free variables for each subsystem must be limited. For the

substructure platform, the design space was adopted from [69], with the free design variables consisting of column spacing to the center line  $d$  and draft of the platform. These variables were chosen based on a sensitivity study conducted in the LIFES50+ project [70], which demonstrated their significant impact on dynamic responses. While the column diameter was also found to be an influential variable in the floater dynamics [71], due to limited computational resources, only two design variables were selected for the optimization. These variables are depicted in orange in Figure 6.1, while the remaining dimensional parameters remain the same as in the original NAUTILUS-10 design [52].

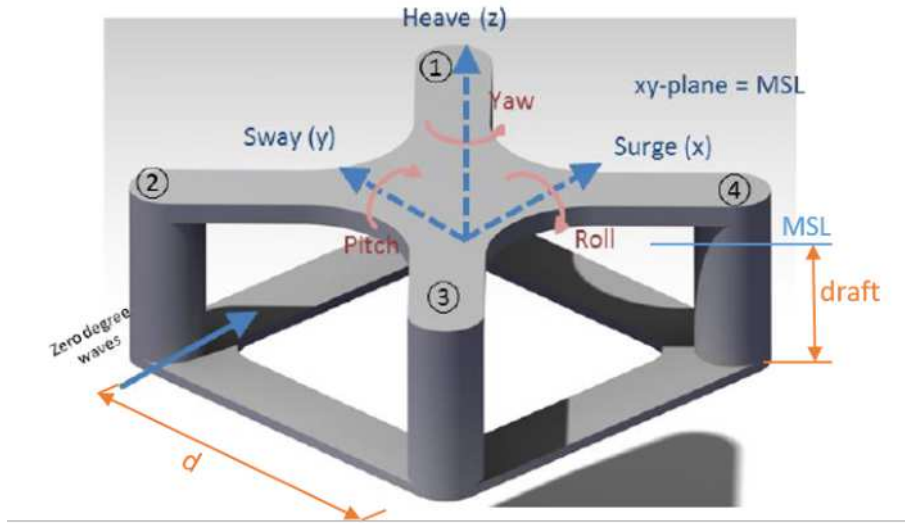


**Figure 6.1:** Illustration of the design variables of the substructure used for the optimization [52][69].

Because the fairleads of the mooring system are fixed to the outer walls of the four vertical columns, their coordinates in the moving body frame of the floater are influenced by the column spacing  $d$ . As a result, the radius of the fairleads can be expressed as a function of  $d$ :

$$r_{\text{fairlead}} = r_{\text{col}} + \frac{\sqrt{2}}{2}d \quad (6.1)$$

$$r_{\text{col}} = 5.25 \text{ m}$$

where  $r_{\text{col}}$  is the original radius of the pontoon taken from [52].

As demonstrated in Chapter 5, specifically in Figure 5.7 and Figure 5.8b, the rise time  $T_r$  of the closed control loop significantly affects the dynamic responses. As the linear model varies with the operating mean wind speeds, it would be ideal to optimize  $T_r$  for the entire wind speed range. However, this results in a very large design space. Thus, only two free variables are chosen, corresponding to the rise time at the operating wind speeds of 12 m/s and 24 m/s. For other operating points, it is assumed that  $1/T_r$  increases linearly over the wind speeds to enable a smooth transition between different operating points. Once the values of  $T_r$  are selected, the control parameters  $k_p$  and  $T_i$  can be determined, as illustrated in Figure 5.5. Notably, the choice of  $T_r$  is influenced by the natural frequency of the platform pitch, and thus the values of  $T_r$  are expressed as relative values with respect to the natural frequency of the platform pitch motion, meaning as a percentage of the natural frequency of the platform pitch.

The TLMCD's horizontal arm must have a length of  $d$  to accommodate the vertical columns of the TLMCD in the floater's vertical pontoons. The head loss  $\eta$  is an important factor for the floater dynamics and is, therefore, defined as a free design variable. Additionally,  $\eta$  can be adjusted by adding baffles inside the TLMCD, another reason for its inclusion as a free variable.

**Table 6.1:** Free variables for the optimization.

Property	Unit	Range	Minimum scale
Column spacing $d$	m	[35, 70]	2
Platform draft	m	[10, 64]	2
TLMCD head loss $\eta$	-	[4, 9]	1
Relative rise time at 12 m/s $T_{r,12}$	%	[80, 110]	5
Relative rise time at 24 m/s $T_{r,24}$	%	[25, 60 ]	5

All the five free variables are summarized in Table 6.1. To speed up the optimization, minimum steps are set for these variables, which means that the design space is discretized instead of being continuous.

### 6.1.2 Cost model

The cost model is an essential part of the optimization framework that can significantly influence the optimization results. While minimal LCOE is generally accepted as a good objective function in the wind industry, it is derived from a wide range of factors, some of which are not relevant to the subsystems under investigation, such as policy, market, or supply chain-related issues. Moreover, certain components of the LCOE may vary in different markets or change with suppliers, making it less informative and potentially unable to reveal the influence of the design parameters. As a result, indicators that not only reflect the LCOE but also have physical meanings and strong correlations with the design variables are used for optimization purposes.

Three indicators are selected for the optimization: a motion indicator, a load indicator, and a cost indicator. The motion indicator will be measured using sensors for the platform pitch and nacelle fore-aft acceleration, while the load indicator will be determined by measuring the tower base bending moment and mooring fairlead tension. Instead of calculating the actual cost for materials, manufacturing, transportation, and so on, the total displaced tonnage (i.e., the weight of water displaced by the FOWT in normal operation) is used as the cost indicator. Although the term "tonnage" can have different meanings in the shipping industry, depending on the loading condition of the vessel, the displaced tonnage is an important measure that can provide a qualitative indication of manufacturing, operation, and maintenance costs. Unlike direct cost calculation, which has many uncertainties and can vary over time and markets, displaced tonnage is a physical value that can be accurately calculated from the structural model. Therefore, it is the only measure used here to indirectly represent all costs associated with material, manufacture, transportation, and installation.

To account for the different units and magnitudes of the selected indicators, they are normalized by comparison to the original LIFE50+ public design NAUTILUS-10. Denoting the displacement, the DEL of the tower base bending and the mooring fairlead tension, the STD of the platform pitch motion and the tower top acceleration as  $V_{\text{disp},0}$ ,  $\text{DEL}_{\text{MyT},0}$ ,  $\text{DEL}_{\text{moor},0}$ ,  $\text{STD}_{\beta,0}$ ,  $\text{STD}_{\text{TT},0}$ , respectively, the objective functions at each wind speed  $\bar{u}_i$  can be expressed as:



$$\begin{aligned}
J_1 &= \frac{V_{\text{disp, child}} - V_{\text{disp,0}}}{V_{\text{disp,0}}} \\
J_2(\bar{u}_i) &= \frac{\text{DEL}_{\text{MyT, child}} - \text{DEL}_{\text{MyT,0}}}{2 \cdot \text{DEL}_{\text{MyT,0}}} + \frac{\text{DEL}_{\text{moor, child}} - \text{DEL}_{\text{moor,0}}}{2 \cdot \text{DEL}_{\text{moor,0}}} \\
J_3(\bar{u}_i) &= \frac{\text{STD}_{\beta, \text{child}} - \text{STD}_{\beta,0}}{2 \cdot \text{STD}_{\beta,0}} + \frac{\text{STD}_{\text{TT, child}} - \text{STD}_{\text{TT,0}}}{2 \cdot \text{STD}_{\text{TT,0}}}.
\end{aligned} \tag{6.2}$$

As can be seen, both  $J_2$  and  $J_3$  show variations over different wind speeds. In commercial applications, it is ideal to weigh these objectives according to the probabilistic distribution of wind speeds. However, the resulting conclusion will inevitably depend on the chosen wind distribution. Since this study focuses on the general methodology rather than deriving an optimal industrial design, the objective functions for each mean wind speed are simply averaged, resulting in a final cost function with multiple objectives:

$$\begin{aligned}
J &= [\bar{J}_1, \bar{J}_2(\cdot), \bar{J}_3(\cdot)] \\
\bar{J}_i(\cdot) &= \text{mean}(J_i(\bar{u}_1), \dots, J_i(\bar{u}_n)), \quad i = 2, 3.
\end{aligned} \tag{6.3}$$

### 6.1.3 Constraints

In order to accelerate the optimization process, a set of design constraints have been defined to eliminate unfeasible designs. These constraints can be classified into two type: static and dynamic. The Static constraints are applied at the beginning of the optimization process and immediately reject any designs that fail to meet the requirements, thus reducing the number of designs to be simulated. The dynamic constraints are applied during the simulation and take into account the behavior of the designs under various load conditions.

The static constraints are checked before any computationally intensive time simulation is conducted. If an individual design fails to satisfy the constraint criteria, it will be excluded from further evaluation. The algorithm will continue to search for potential candidates in order to maintain the size of the design candidates to be evaluated. The constraints on the natural frequencies of the floater are primarily intended to avoid the wave frequency range. These static constraints are defined as follows:

- The displaced tonnage should not be more than twice as much as that of the NAUTILUS-10 design, i.e.  $J_1 \leq 1$ .
- The maximum static pitch angle should be smaller than 10 deg.
- The heave natural period should be greater than 15 s.
- The pitch natural period should be greater than 18 s.

To further refine the optimization process, dynamic constraints are defined based on statistical analysis of dynamic simulations. If a design exceeds these constraints, the algorithm sets high values to the cost model  $J$ , redirecting the optimization towards alternative designs. The dynamic constraints consider various scenarios, including:

- The generator overshoot should be less than 30 %.
- The maximum dynamic pitch should not exceed 12 deg.
- The nacelle acceleration should be smaller than  $0.3g$ , where  $g$  is the gravitational acceleration.

It is worth noting that the selection of constraints relies on both experience and established rules of thumb derived from previous research projects. This approach not only guarantees timely convergence but also enables exploration of a wider range of potential solutions within the design space. However, it is important to emphasize that these chosen values may be conservative and may not necessarily align with commercial standards.

#### 6.1.4 Multi-objective optimizer

As discussed previously, three indicators are selected for the cost model, which evaluate the goodness of the FOWT designs. One can combine these indicators into one overall objective function by using weight coefficients to find the optimum. However, the determination of such weight coefficients is very difficult, especially in the case of academic research without input of industrial parties on the realistic weighting factors. On the other hand, the weight coefficients can significantly influence the optimization path and the final result. Therefore, it is decided to use a multi-objective optimizer. It can provide the designers with a subset of favorable designs in different scenarios, rather than a unique optimum.

NSGA-II is a widely-used multi-objective genetic algorithm. Inspired by Darwin's

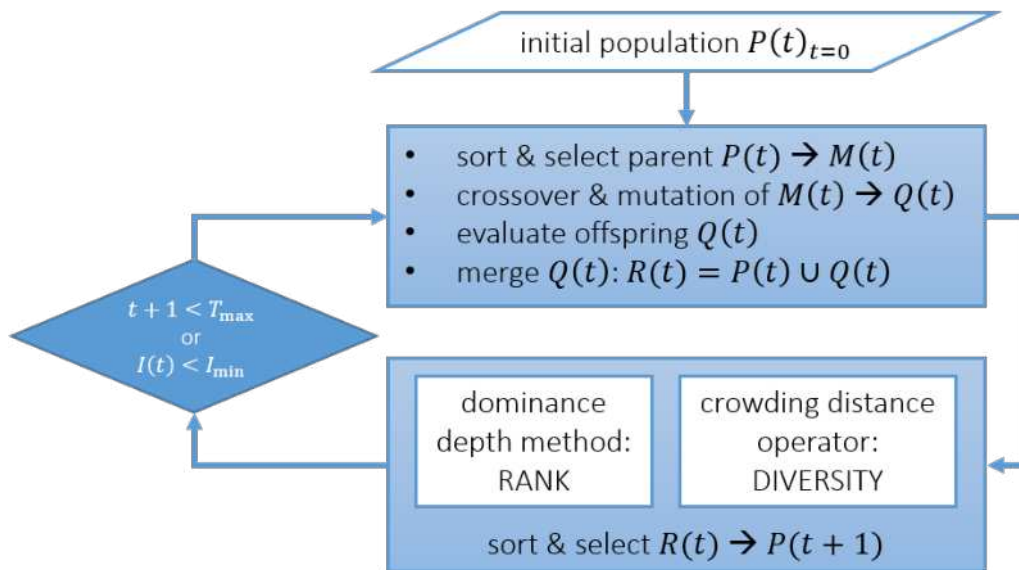


Figure 6.2: Flowchart of NSGA-II.

theory of evolution, NSGA-II simulates the reproduction, competition, and selection process of creatures and aims to find the survival populations throughout the evolution. In the case of this work, the survival populations are the combination of substructure designs that provide the best motion, load, and cost performance, as defined in the previous section.

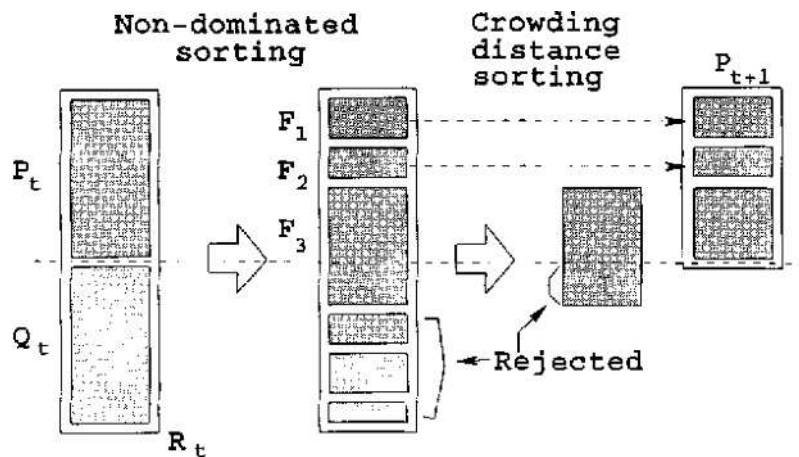


Figure 6.3: Sorting and selection mechanism of NSGA-II [72].

A comprehensive explanation of NSGA-II can be found in [72]. Here, only the

crucial elements will be highlighted. Figure 6.2 illustrates the flowchart of the optimization process with NSGA-II, starting with an initial population  $\mathbf{P}(t)_{t=0}$  consisting of randomly selected individuals from the design space, consisting of different combinations of subsystem designs. The performance of each individual is evaluated through simulations, and those with better performance are selected as parents  $\mathbf{M}(t)$ , carrying better genes. Using crossover and mutation,  $\mathbf{M}(t)$  generates offspring  $\mathbf{Q}(t)$ , which are then merged into the initial population  $\mathbf{P}(t)$  to form a larger population  $\mathbf{R}(t)$ . However, due to resource limitations, only a subset of the individuals within  $\mathbf{R}(t)$  is selected to survive based on the performance criteria defined by the objective functions. The new generation  $\mathbf{P}(t+1)$  is created through the selection process, and the loop continues until the stopping criteria are met. Two stopping criteria are implemented, namely the maximum allowed number of generations and the Mutual Domination Rate (MDR), which is used to quantify the improvement of every generation [73].

Figure 6.3 depicts the selection principles by which individuals can survive. The  $t_{th}$  generation initially contains both the parent population  $\mathbf{P}_t$  and the offspring  $\mathbf{Q}_t$ . After evaluating the performance of each individual in this generation, all individuals are ranked and categorized into different fronts  $F_1, F_2, F_3 \dots$ , where  $F_1$  represents the best-performing category. Categories with ranks  $F_1$  and  $F_2$  are directly added to the next generation, while  $F_3$  is partially selected based on the crowding distance between the selected individuals. The goal is to maintain diversity in the new generation as much as possible.

## 6.2 Workflow for Objective Evaluation

After knowing how the optimization framework searches for favorable designs, it becomes clear that the most essential and computationally expensive step is the performance evaluation based on the objective functions. This evaluation process includes designing and modeling the subsystems, performing coupled simulations in the time domain, as well as post-processing the simulation data to compute the objective functions.

The evaluation of the generated offspring  $\mathbf{Q}(t)$  in each generation requires a number of interconnected processes, as illustrated in Figure 6.4. These simulation pro-

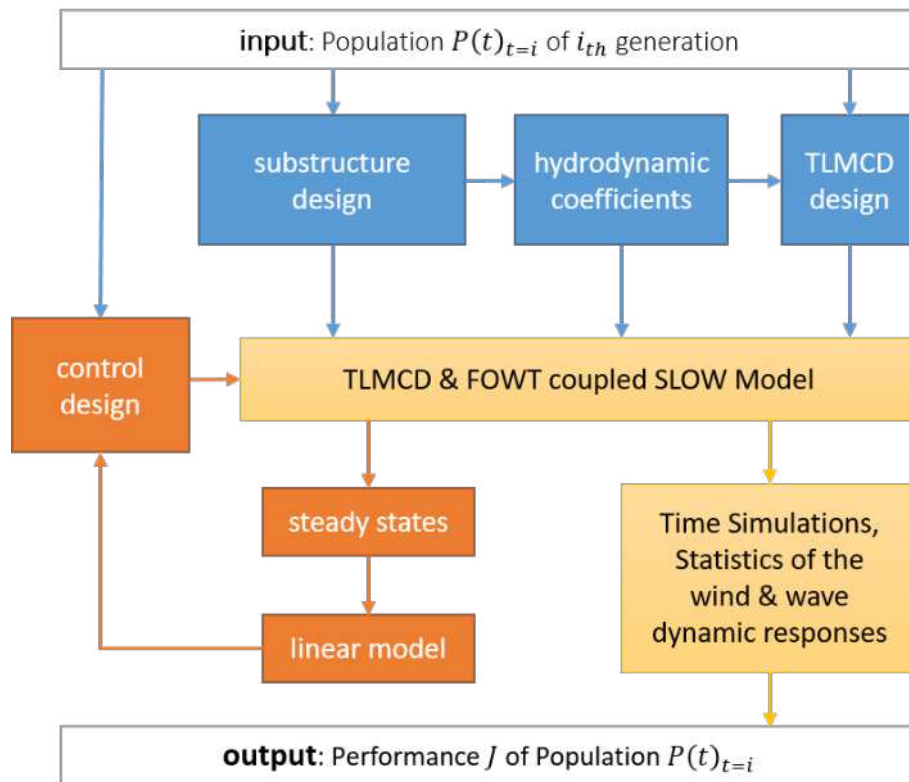


Figure 6.4: Workflow of evaluating offspring of the  $i_{th}$  population.

cesses can be roughly divided into three parts: the preparation of the dynamic model inputs (in blue), model linearization and controller design (in orange), and coupled design load case simulation (in yellow).

### 6.2.1 Inputs preparation of the dynamic model

The substructure design module is the first step in the optimization process. It takes the design variables of each offspring as input and calculates the inertial properties of the FOWT based on its geometrical variables. At the same time, the module generates a mesh for the wet surface of the substructure and associated panel coordinates. The data produced here are then passed on to the hydrodynamic module. The main function of this module is to generate the hydrodynamic coefficients using the panel code ANSYS-AQWA. In addition, the module calculates the RAOs and natural frequency of the platform pitch motion, which serve as input data for

the TLMCD design module. Both of these design modules are described in more detail in [22] and [69]. The TLMCD design module uses the same method as that presented in [40]. The main objective is to ensure that the TLMCD has the same natural frequency as the platform pitch, while also keeping the total fluid mass within the TLMCD constant at 3% of the total FOWT mass.

### 6.2.2 Model linearization and controller design

After all inputs for the dynamic plant are set up, steady states for various operating wind speeds can be simulated and calculated. These steady states are then used for the model linearization. The linear models are established using the linearization procedure outlined in Section 3.5.2, while the control design process is detailed in Chapter 5.

### 6.2.3 Coupled design load case simulation and cost evaluation

Once the dynamic plant and controller are set up, the next step is to perform coupled time domain simulations using a subset of design load cases recommended in the LIFE50+ project [66]. These load cases are listed in Table 6.2 and are used to evaluate the performance indicators for the objective functions.

**Table 6.2:** Design load cases used for optimization.

Significant wave height $H_s$ [m]	1.38	1.67	2.2	3.04	4.29	6.2	8.31
Wave peak period $T_p$ [s]	7	8	8	9.5	10	12.5	12
Mean wind speed $\bar{u}$ [m/s]	5	7.1	10.3	13.9	17.9	22.1	25

## 6.3 Optimization Result

To find the optimal designs, two rounds of optimization are carried out. In the first round, a simple geometrical optimization is conducted using only two design variables, namely the column spacing  $d$  and the substructure draft. In the second round, all five variables listed in Table 6.1 are used in the optimization process that

involves all submodules. The results obtained from both rounds are discussed in this section.

### 6.3.1 Initialization and convergence

The initial population size is determined based on a general rule of thumb [74], which suggests a population size of approximately 10 times the number of design variables. For the first round of optimization, where only the substructure is optimized, a population size of 20 is used. For the second round, which involves the TLMCD and blade pitch controller in the optimization loop, the population size is increased to 50. The maximum number of generations allowed for the first and second rounds is 50 and 100, respectively. The MDR threshold is set to 0.05.

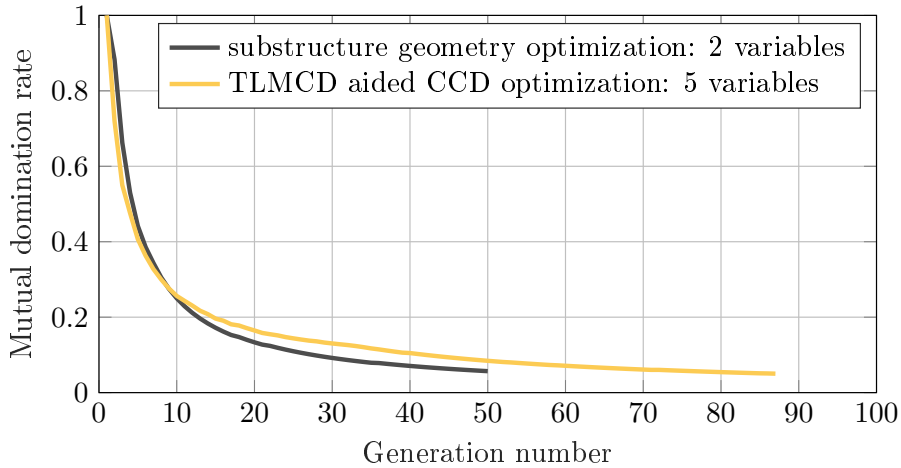


**Figure 6.5:** Mutual domination rate of the optimization process.

Convergence is a crucial aspect in demonstrating the validity of the optimal solutions found by the optimizer, and therefore it is important to check for convergence when using genetic algorithms. Figure 6.5 shows the convergence progress of both optimization loops, illustrating the development of the two stopping criteria defined previously. For the substructure-only optimization, the MDR reaches 0.06 after 50 generations. As for the TLMCD-assisted CCD optimization, the optimization process stops before the 90th generation, as the MDR reaches the stopping threshold of 0.05, instead of reaching the maximum allowed 100 generations. This result

indicates that the two stopping criteria are suitable to ensure convergence in the optimization process.

### 6.3.2 Optimized objective space

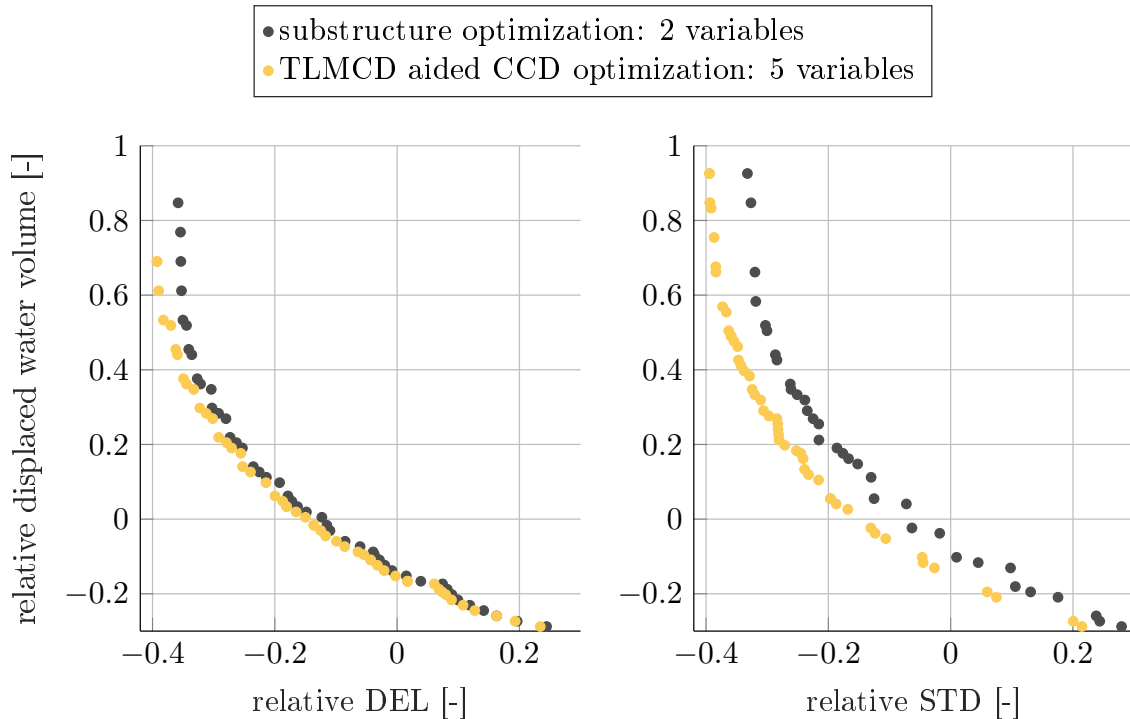
#### Two-objective optimization

Figure 6.6 gives the result of a two-objective optimization, showing the change of the Pareto front when additional optimization variables are added. On the left, the objectives are the non-dimensional displacement (relative displaced volume compared to the original NAUTILUS-10 design) and the relative DEL. On the right, the objective is switched to the relative STD. As defined in Equation 6.2, DEL includes both tower base fore-aft bending moment and fairlead tension, STD includes the platform pitch motion and tower top acceleration. For simplicity, the following discussion refers to them as DEL-cost and STD-cost.

Observing the black points where only two variables related to the substructure geometry are used for the optimization, two conclusions can be drawn. The first conclusion is about the relation between the objectives. Both DEL-cost and STD-cost are inversely correlated with the relative displaced water volume (displacement). This inverse correlation is almost linear and is evident between approximately 20% above and below zero displacement. As the relative displacement increases further to 0.5 (equivalent to 50% more displacement than the NAUTILUS-10), the DEL-cost and STD-cost are only marginally reduced. Conversely, decreasing the displacement may result in a reduction in the total material, construction, transportation, and installation costs. However, this reduction comes at the cost of higher DEL and STD.

The second conclusion is that the point  $(0,0)$ , representing the same cost as the original NAUTILUS-10, lies almost on the Pareto front when both displacement and STD-cost are optimized. This implies that the NAUTILUS-10 design is one of the optimal choices from the STD-cost perspective. However, this is not the case with respect to the DEL-cost. In the left plot, which shows the relationship between DEL-cost and displacement, it can be observed that the point  $(0,0)$  is on the right hand side of the Pareto front, indicating that better solutions are found through optimization. It is worth noting that all the optimal solutions with similar





**Figure 6.6:** Pareto fronts resulting from the 2-variable substructure optimization, showing the trade-off between the relative displaced water volume and the relative costs. Left: relative displaced water volume versus relative DEL-cost; Right: relative displaced water volume versus relative STD-cost.

displacement have a column space  $d$  larger than 60 m, while the original design has a  $d = 54.75$  m. A larger column space is generally beneficial for the tower base bending moment, but it can also lead to a structural problem due to the heave plates and deck connecting all the vertical columns, which are relatively thin. This structural issue is however not analyzed in this work.

When the TLMCD and the blade pitch controller are included and optimized simultaneously, it causes a change in the Pareto fronts, which highlights the impact of these subsystems on the substructure geometry optimization. First of all, the shape of the Pareto front is very similar to the one obtained from the pure substructure geometry optimization. Therefore, all the conclusions made previously still apply to this case as well. However, a significant improvement in the platform pitch motion can be observed. For the same displacement, the STD-cost can be reduced by 5 to 10%. In terms of the DEL-cost, the contributions of the TLMCD and the blade

pitch controller are limited when the displacement is relatively small, referring to the design space with compact geometry designs that have higher tolerance for surge and pitch motions and tower loading. These designs are generally lighter and have lower natural frequencies, making them more susceptible to wave-induced excitation. Even when additional damping is applied, this phenomenon is not fundamentally changed. However, the mass of the TLMCD plays an important role in this case. Since the fluid mass inside the TLMCD remains relatively constant, i.e. 3% of the FOWT weight, a smaller substructure will have a TLMCD with less fluid mass. This means that its ability to compensate for motion induced by aerodynamics is limited because the TLMCD is relatively small, and the wind turbine does not change. Consequently, designs with larger displacement can achieve a greater improvement by including the TLMCD.

### Three-objective optimization

The Pareto front resulting from a two-objective optimization demonstrates only the best solutions for each optimization case. As a result, the decision space for the two cases, as shown in Figure 6.6, may differ, which means a design that minimizes STD-cost may not necessarily minimize DEL-cost simultaneously. To address this issue, it becomes necessary to optimize all three objectives. Figure 6.7 depicts the Pareto surfaces from two different viewpoints, allowing the identification of the impact of additional optimization variables.

The general conclusions drawn from the two-objective optimization remain applicable. To achieve the same DEL- and STD-cost, the required displacement is less when equipping the floater with a TLMCD. This results in a lower total cost of the substructure. Comparing the surfaces from the two viewpoints, it is found that the displacement reduction is more evident when the STD-cost is relatively low. However, when the STD-cost is extremely high, i.e., more than 20% higher than the original NAUTILUS design, which represents a design with a highly dynamic system and is strongly excited by wind and waves, the effect of the TLMCD is almost negligible.

To gain a better understanding of the displacement reduction contributed by the TLMCD, the contour lines of the displacement reduction over the STD-cost and

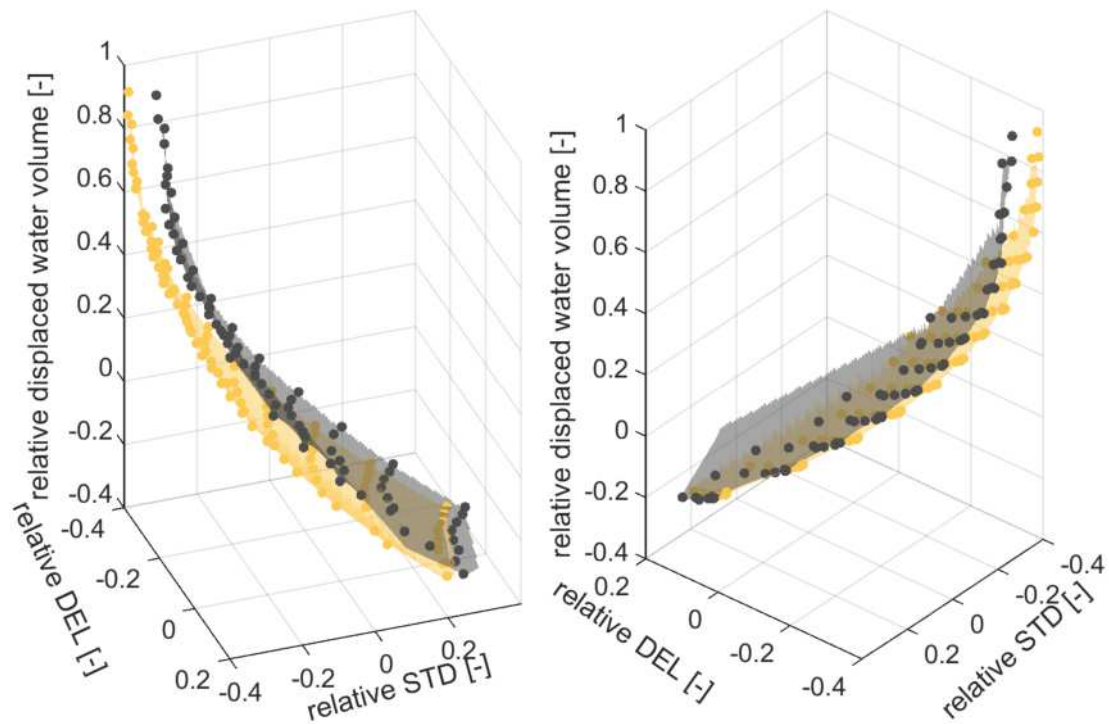


**Figure 6.7:** Comparison of Pareto optimal surfaces between the two-variable geometric optimization (in black) and the five-variable TLMCD aided CCD optimization (in yellow).

DEL-cost are presented in Figure 6.8. Here, the displacement reduction refers to the difference in the relative displaced water volume on the Pareto surfaces for the same DEL and STD in Figure 6.7. A negative value indicates that the design with TLMCD requires less displacement to achieve the same DEL-cost and STD-cost, allowing for a cost reduction (indirectly reflected by the reduced displacement) without compromising on the loads and motions. Overall, the FOWT displacement can be reduced by up to 20% by equipping the floater with a well-designed TLMCD, along with a tailored blade pitch controller. If the DEL-cost and STD-cost of the original NAUTILUS-10 are the targets, then the displacement reduction ranges approximately from 5% to 10%.

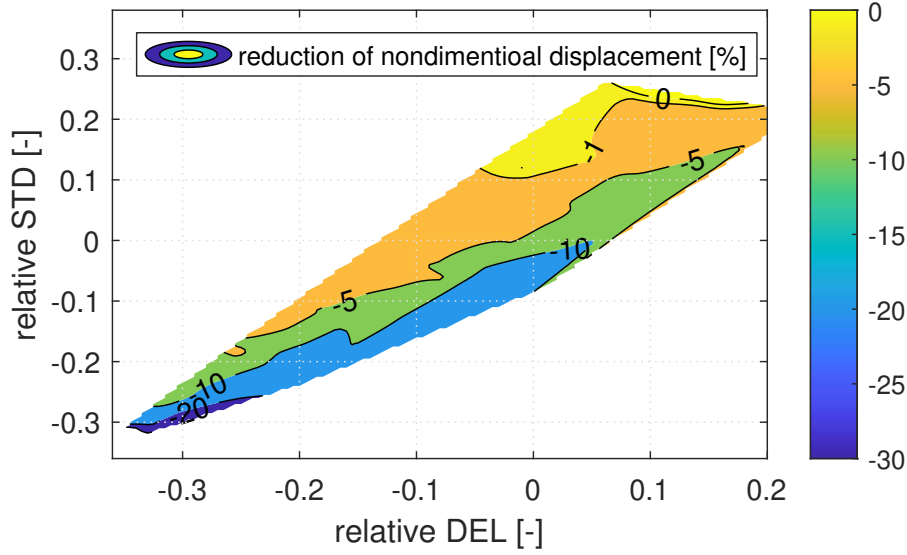
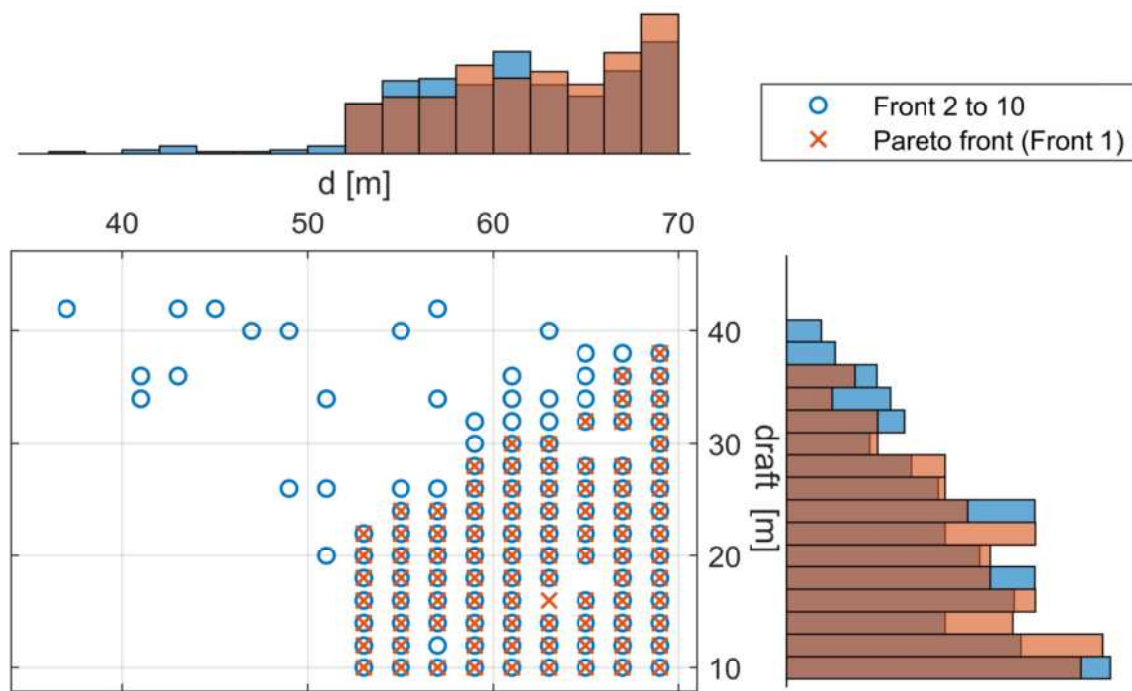


**Figure 6.8:** Relative reduction in displacement contributed by the TLMCD aided CCD optimization.

### 6.3.3 Optimized decision space

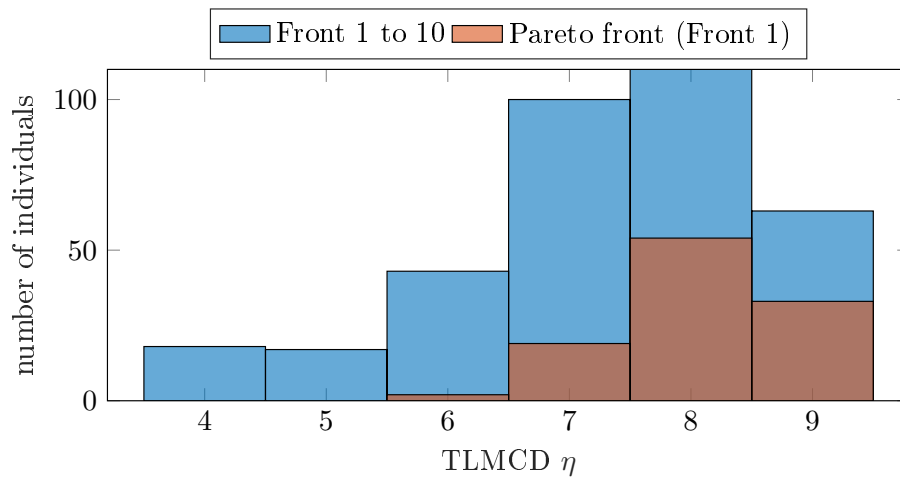
So far, the focus has been on the optimal objectives. For system designers, the space of design choices that ensures good performance is also of interest. In the following, the decision space is discussed, and the optimal subsystem designs, chosen by the optimizer, are presented.

Figure 6.9 shows the optimal geometric design space of the substructure and its corresponding histograms. The data indicates that the optimal designs tend to have larger column spacing  $d$ , and no solutions are found for  $d < 50$  m. Designs with column spacing within the range of  $d \in [66 \text{ m}, 69 \text{ m}]$  account for the highest percentage of designs on the Pareto front. This trend can be explained by the increased second-order moment of inertia of the water plane area due to the larger column spacing  $d$ . With the same mass and displacement, a substructure with a larger column spacing can generate a higher restoring moment in roll and pitch directions, resulting in reduced pitch and roll motions. However, it is important to note that the structural integrity of the deck and heave plate, which connects the four vertical columns, is not included in the optimization process. As a result, the distribution of optimal designs may differ if this factor is taken into account.



**Figure 6.9:** Geometric decision space on the Pareto surface.

Additionally, it is interesting to observe that many optimal solutions are found slightly below 60 m, despite the relatively smaller column spacing in this range.



**Figure 6.10:** Optimal head loss  $\eta$  of the TLMCD for the decision space.

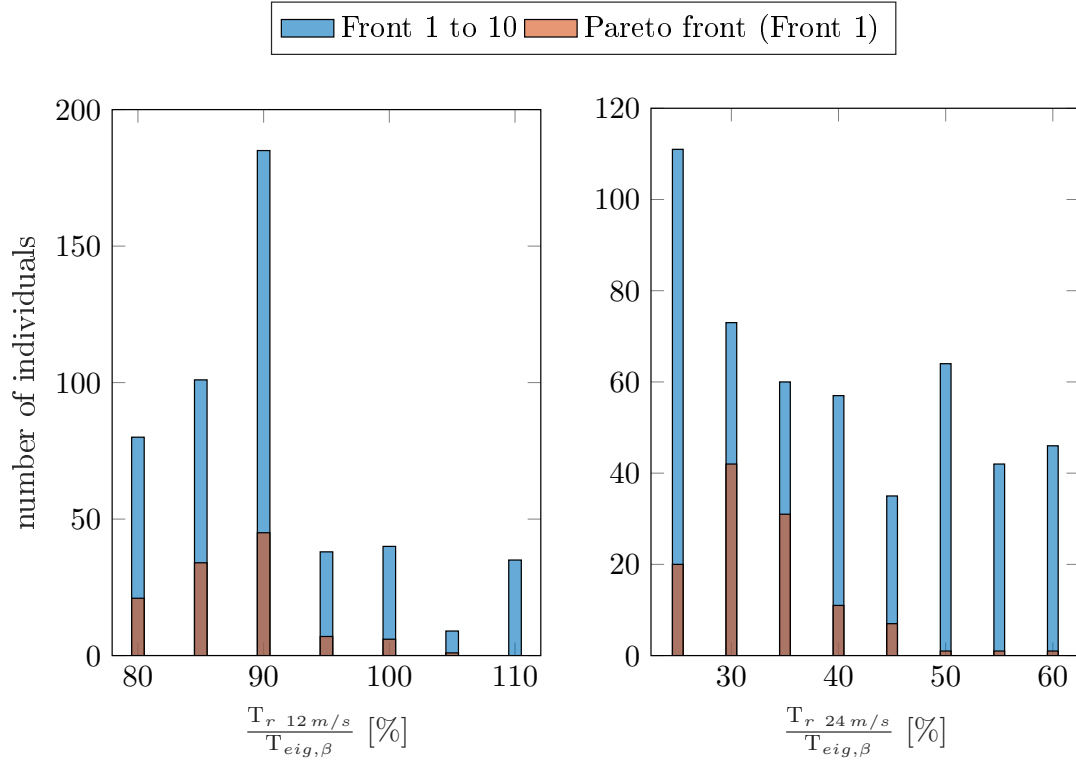


**Figure 6.11:** Controller decision space on the Pareto surface.

The only design variable for the TLMCD is the head loss  $\eta$ . The histogram of the optimal designs reveals that most solutions have  $\eta$  values in the range of 7 to 9, with  $\eta = 8$  being the most frequently chosen value. However, it is important to keep in mind that this optimal value of  $\eta$  is only applicable to this particular concept, which has several pre-defined design requirements that can limit the range of the design variable.

The last two design variables are associated with the blade pitch controller, namely the rise time  $T_r$  of the closed control loop at wind speeds of 12 m/s and 24 m/s, respectively. In Chapter 5, it is concluded that  $T_r$  at 12 m/s should be slightly smaller than the platform pitch natural period. This conclusion is confirmed quantitatively by the distribution of the optimal  $T_{r, 12 m/s}$ , which shows that 90% of the platform pitch natural period is the best choice. A slightly smaller value of  $T_r$  (i.e. 85% of the platform pitch natural period) can still provide satisfactory performance. With regard to the optimal  $T_r$  at 24 m/s, the histogram indicates that a value of 30% or

slightly higher (i.e. 35%) yields the best performance.

## 6.4 Comparison of Dynamic Responses

The results of the TLMCD aided CCD optimization demonstrate the potential to reduce the displaced tonnage of a FOWT by up to 20%. While the optimizer only considers the predefined cost model, it is still meaningful to examine the dynamic responses of the optimal designs. Therefore, two designs on the Pareto surface are selected, which have similar DEL-costs and STD-costs to the original NAUTILUS-10 design. The values of all design variables for these designs are listed in Table 6.3.

Design-1 has a column spacing that is similar to the original design but a draft that is four meters shorter. As a result, the displaced tonnage of Design-1 is reduced by 11.6%. In comparison, Design-2 has a larger column spacing and a lower draft. However, the DEL-cost of both designs is less than 1% different from the original NAUTILUS-10 design. In addition, Design-1 has an even lower STD-cost, while Design-2 has a lower displacement at the expense of 7.1% increase in STD-cost.

**Table 6.3:** Properties and costs of the two selected designs on the optimal Pareto surface.

	$d$ [m]	draft [m]	$\eta$ [-]	$T_{r,12}$ [%]	$T_{r,24}$ [%]	$J_1$ [%]	$J_2$ [%]	$J_3$ [%]
Deign-1	55	14	8	90	30	-11.6	-0.73	-4.5
Deign-2	61	12	9	105	35	-15.2	-0.26	7.1

Figure 6.12 shows the statistical analysis of all sensors used in the cost model. The DELs of the tower base bending moment and the fairlead tension are quite similar between the optimal design and the original NAUTILUS-10 design, with slightly lower fairlead tension for the former in the wind speed range of 11 m/s to 20 m/s. However, the nacelle acceleration of the optimal design is higher across all operating wind speeds, mainly due to the reduced draft. This reduction results in a higher overall center of gravity and thus lower pitch stiffness, leading to a slightly larger mean platform pitch angle for the optimal design. Below rated wind speeds, the platform pitch of both designs is similar, as the blade pitch is not yet activated. However, at higher wind speeds, the redesigned blade pitch controller

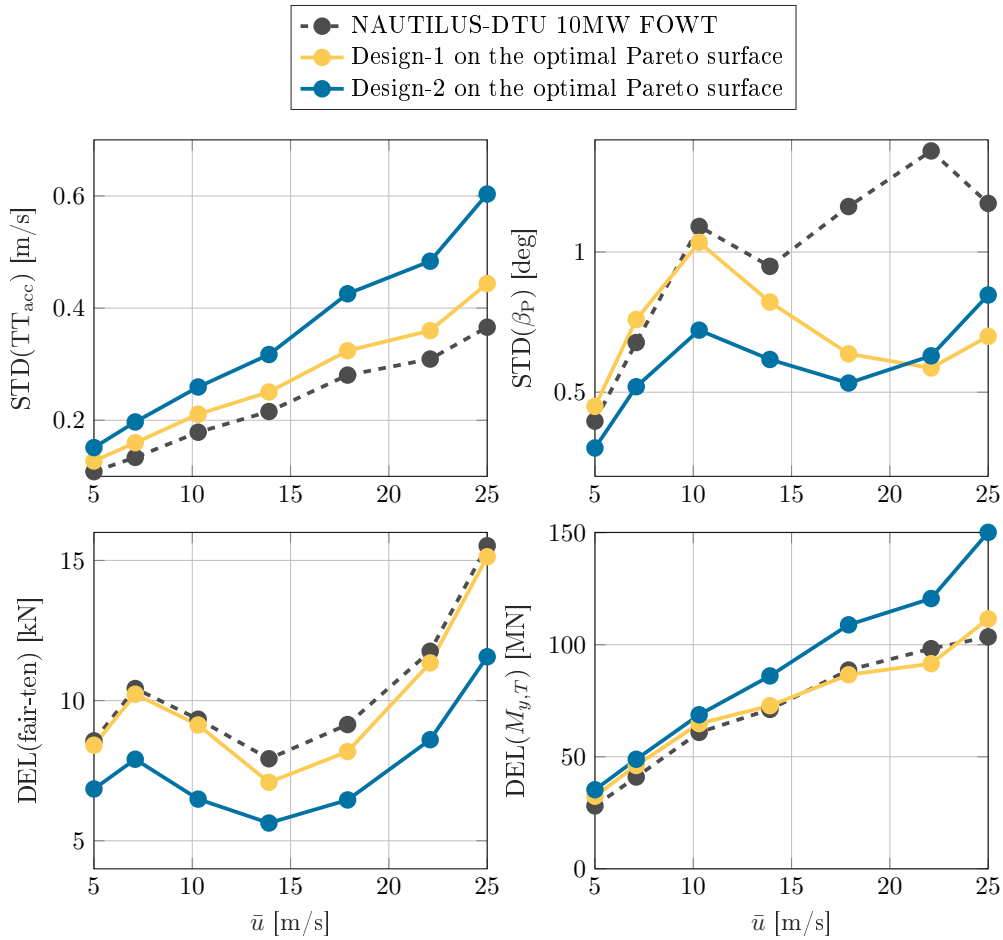


**Figure 6.12:** Comparison of statistical responses between the original NAUTILUS-10 design and two selected designs with similar STD-cost and DEL-cost on the optimal Pareto surface.

and the positive contribution from the TLMCD significantly reduce the motions. Nonetheless, since the cost model considers tower top acceleration and platform pitch motion equally in the cost calculation, the final STD-cost of the optimal design is comparable to that of the original NAUTILUS-10 design.

Figure 6.13 presents a comparison of the PSDs response at a wind speed of 13.9 m/s. Due to the significant differences in the PSD amplitudes across the frequency range, the plots are divided into two parts for clarity. The left plot shows



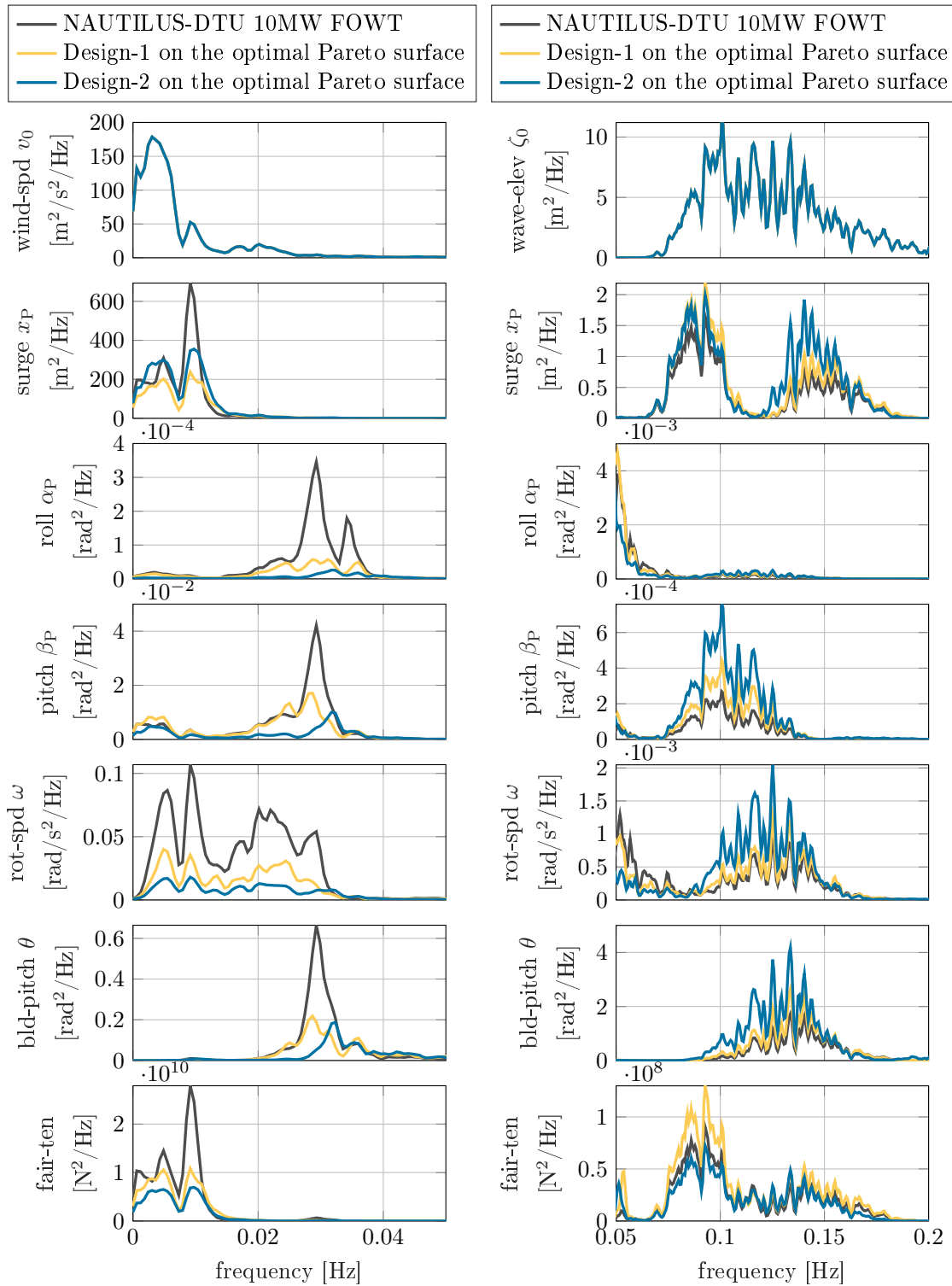


**Figure 6.13:** Comparison of frequency responses between the original NAUTILUS-10 design and two selected designs with similar STD-cost and DEL-cost on the optimal Pareto surface at wind speed 13.9 m/s.

the frequency range from 0 Hz to 0.05 Hz, while the right plot shows the frequency range from 0.05 Hz to 0.2 Hz.

The lower frequency range of the PSDs is significantly dominated by wind excitation. In addition, resonances due to the natural frequencies of the platform motions are also present in this region. Notably, Design-1 and Design-2 have significantly lower roll and pitch response amplitudes near 0.03 Hz, indicating a significant contribution from the TLMCD. This reduction in response amplitudes leads to a decrease in the relative wind speed caused by platform motions, thereby reducing the blade pitch activity. As a result, the oscillation of rotor speed is visibly reduced, as shown by the decreased amplitude in the PSDs.

The higher frequency range is primarily excited by the waves. One key observation is that the amplitudes of the PSDs are generally much smaller in this region, as seen from the scale of the vertical axis. In contrast to their behavior at lower frequencies, both Design-1 and Design-2 show higher roll and pitch motions in this range. The main reason for this is the substructure geometry, which has reduced displacement and therefore has a negative impact on the dynamic responses in waves. This affects also the blade pitch and rotor speed. Nevertheless, the roll and pitch motions of both designs are slightly lower than those of the NAUTILUS-10 when considering the response across the entire frequency range.

# 7 Conclusions and Outlook

This chapter provides an overview of the key conclusions derived from the research conducted in this dissertation. It includes a short summary of the methodologies and tools developed, the significant knowledge and findings gained through the research, as well as recommendations for future research.

## 7.1 Main Contributions

The primary objective of this thesis is to explore systematically the effectiveness of tuned liquid dampers in reducing the cost of FOWTs. In pursuing this goal, four major contributions have been made in terms of modeling, control, and optimization:

- **Numerical model development**

In Chapter 3, a numerical tool is developed to model the TLMCD and FOWT coupled system. To achieve the goal, the 2D SLOW, developed in [2], is extended by adding extra DOFs to the floater to account for 3D motions. The TLMCD, proposed by [3], is then adapted to be integrated into the MBS framework of SLOW. A simplified formulation for TLMCDs with uniform cross sections for vertical columns and connecting arms is derived, enabling easier and more efficient implementation of the model. In addition, the developed coupled model is linearized, which is essential for controller design. Finally, the model is verified through code-to-code comparison against the state-of-the-art engineering tool OpenFAST.

- **Validation of the model through experiments**

In order to evaluate the performance of the developed coupled model, two campaigns of scaled model tests are carried out. The tests and associated validation are detailed in Chapter 4, demonstrating that the developed model

is capable of reproducing accurately the dynamic behavior of the coupled system. Although only reduced DOFs are enabled, the model is well-suited for conceptual design, controller design and system-level optimization of TLMCD stabilized FOWT systems.

- **Control adaption**

An automated blade pitch control design methodology, which takes into consideration both stability and performance criteria, is developed in Chapter 5. The design procedure improves upon the method presented in [65] by incorporating closed loop shaping into the design procedure. The presence of the TLMCD changes the characteristics of the FOWT dynamic plant, more specifically, the negative aerodynamic damping is partially compensated by the TLMCD, allowing the bandwidth of the blade pitch controller to be increased. The developed control design procedure can adapt easily the blade pitch controller for different TLMCD stabilized FOWT systems, being the basis for the integrated CCD optimization of FOWTs.

- **TLMCD-aided CCD optimization**

A multi-objective CCD optimization framework is developed in Chapter 6, which allows to optimize the floater, the TLMCD and the blade pitch controller simultaneously. Prior work has shown the close connection between these subsystems due to the strong coupling between the aerodynamics, hydrodynamics and the controller. Subsequently, the framework searches for the optimal design space in which these subsystems achieve good synergism, ensuring a better compromised production cost and response performance. The optimization results demonstrate the potential of reducing the displaced tonnage of a FOWT by installing a TLMCD into FOWT.

## 7.2 Findings and Lessons Learned

During the development, knowledge and best practices have been gained, and some lessons been learned. These findings and lessons are discussed in the following.

When modeling a MBS, the use of generalized coordinates simplifies the derivation of equations of motion for complex systems by combining the Lagrangian mechanics

and Newton-Euler equations. In this work, the equations of motion of the TLMCD are derived using the Lagrangian mechanics, while those for the FOWT are based on the Newton-Euler equations. This combines the advantages of both methods, resulting in a more flexible formulation. Despite the different mechanical formulations, both methods result in equivalent descriptions of the system dynamics. Such combined methods are useful when additional subsystems such as dampers or actuators are introduced into the FOWT systems.

The head loss coefficient  $\eta$  is the design parameter of the TLMCD that presents the greatest uncertainty. This parameter is crucial for the performance of the coupled system and also affects the design of the blade pitch controller. Hence, selecting an appropriate value of  $\eta$  during the design phase is important. However, since  $\eta$  is dependent on the geometric characteristics of the TLMCD, determining its value poses a significant challenge that requires CFD simulations or experiments. Nonetheless, adjusting  $\eta$  by adding additional orifices inside the TLMCD can be done to achieve the desired performance.

In general, simply adding a TLMCD to a FOWT system does not necessarily improve the overall performance. In fact, it may sometimes lead to even worse responses. Unlike anti-roll tanks in the ship industry, where TLCDs are designed to minimize the motions, the capability in motion reduction of a TLMCD for FOWTs is more limited due to the additional aerodynamics and control iterations. Attempting to minimize motion can lead to designs with lower performance, especially if the blade pitch is not adapted to the TLMCD. The main contribution of a TLMCD to a FOWT is that it can partially compensate for the negative aerodynamic damping. Therefore, it is essential to redesign the controller together with a TLMCD to maximize the benefits of motion and load reduction.

The presented CCD optimization faces significant barriers to delivering economically meaningful results, with the cost model being one of the most prominent obstacles. The cost model is highly sensitive and can yield very different results and conclusions, making it crucial to accurately quantify economic considerations in the model. Another obstacle is the need to limit the number of objectives due to constraints on optimizer and computational resources. For example, NSGA-II only optimizes efficiently for two to three objectives. If more objectives need to be added, a many-objective optimizer is required. Regardless of the optimizer, increas-

ing the number of objectives will generally slow down the convergence time significantly. Additionally, the large number of free design variables required to evaluate an individual in the design space requires large computational resources. This is particularly challenging for FOWTs, which involve highly coupled subsystems from multiple disciplines, making it difficult to narrow down free design variables and converge to an optimal design within a reasonable time frame. To address this issue, it is advantageous to keep the free design variables of the optimization discrete. Multiple rounds of optimization can be executed to progressively narrow down the design variables and step size in each subsequent optimization round.

### 7.3 Recommendations for Future Work

Due to the limited time, simplifications have been made, and some of physical aspects have been neglected. Therefore, improvements can be made to further advance the TLMCD for industrial application, the possibilities are listed below:

- The free surface of the TLMCD reduces the metacentric height of the FOWT and thus the static stability. In this work, only a limit on the metacentric height loss is set. How this loss influences the dynamic behavior of the system should be studied with more details.
- The head loss of the TLMCD has a large influence on the damping effect. However, it varies with its geometrical properties. The determination of the head loss based on experimental tests is not cost effective. Thus, establishing reliable estimation by CFD will improve the design of a TLMCD.
- The substructure design in the optimization has only two variables, which has narrowed down the design choices. For industrial applications, optimization with additional geometric variables may be necessary.
- The mode shapes of the tower can change as the floating substructure varies. Since tower top acceleration is an important cost indicator, it is advisable to include the tower structure and design in the optimization loop.
- Structural integrity check is necessary for the optimization of some substructure concepts. For instance, the influence of the heave plate of the NAUTILUS-10 design, without the consideration of the heave plate, the optimal design space tends to have larger column spacing.

- 
- As the controller has an big impact on the TLMCD performance, more advanced control strategies, which takes the benefit of additional sensors and actuators, may provide better response performance.
  - By controlling the fluid flow through propellers or air valves, the TLMCD can be adapted into an active system, which has been done in the ship industry. Such a damper works in a variable frequency range, including the wave frequencies. This can improve the overall performance, especially in extreme wave conditions.





# A Damping coefficients from experiments

A second order harmonic oscillating system with both linear and quadratic damping can be written as:

$$\ddot{x} + b_1\dot{x} + b_2|\dot{x}|\dot{x} + \omega_0^2x = 0 \quad (\text{A.1})$$

where  $b_1$  and  $b_2$  are the linear and quadratic damping coefficients. By using an equivalent linearization, Equation A.1 can be simplified as:

$$\begin{aligned} \ddot{x} + b\dot{x} + \omega_0^2x &= 0 \\ b &= b_1 + \frac{16}{3}X_i f_d b_2 \end{aligned} \quad (\text{A.2})$$

with  $X_i$  representing the amplitude each half cycle and  $f_d$  the damped frequency. For a linear system, the damping coefficient  $b$  can be written as:

$$b = \frac{4\pi f_0}{\sqrt{1 + (\frac{\pi}{\delta})^2}} = 2\omega_0\zeta \quad (\text{A.3})$$

where  $\delta$  is the logarithmic decrement calculated by  $\delta = \ln \frac{X_i}{X_{i+1}}$ ,  $\zeta$  is the dimensionless damping ratio.  $f_d$  can be obtained by direct fast Fourier transformation of the experimental time signal,  $f_0$  equals then  $\frac{f_d}{\sqrt{1-\zeta^2}}$ . By using linear fitting, one can plot the line of  $b$  over  $\frac{16X_i f_d}{3}$ , it is able to get  $b_1$ ,  $b_2$ .



# B Influences of model fidelity on control design

As discussed in Section 5.2.3, it is convenient to analyze the closed-loop system response analytically, which is feasible for onshore wind turbines. However, for FOWTs, the platform motion has a significant impact on the coupled response, and therefore the dominant modes of motion must be included into the transfer function used for control design. This results in additional poles and zeros, requiring a higher-order system for loop shaping. However, a more complex transfer function makes it more challenging to characterize the response analytically. Therefore, it is preferable to use a model that captures the most significant physical effects, making it necessary to investigate the minimum fidelity required for the control-oriented linear model. To answer this question, simulations and linear analysis using the OO-Star DTU 10MW FOWT are conducted.

Figure B.1 shows the step response simulated by models with various DOFs. The DOFs considered here are the rigid body rotation of the rotor which is simply represented as the drivetrain rotation (DrTr), platform pitch (PtfmPitch), tower top fore-aft motion (TwrFA), as well as platform surge (PtfmSurge). According to the step response, it is essential to add the platform pitch motion to get a realistic dynamic response. The locations of the extra poles of different DOFs are plotted in figure B.2. By comparing to figure B.1, the most significant impact is introduced by the platform pitch motion. For the one DOF model, an overdamped system is indicated by the poles located on the real axis, as well as a non-oscillating step response. When extra poles of platform pitch motion are introduced to the transfer function, additional dynamics are observed in the step response. The poles of the drivetrain mode are lying on the real axis which indicates an over damped behaviour, the oscillating response shows the dominance of the platform pitch motion. Poles of

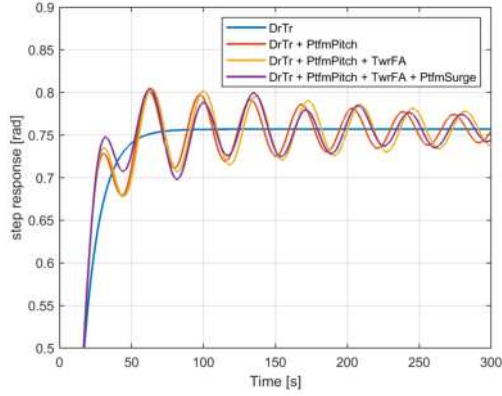


**Figure B.1:** Comparison of the step responses from wind to generator speed with different DOFs included ( $V_0 = 14$  m/s,  $k_p = 0.3$  s,  $T_i = 9$  s).

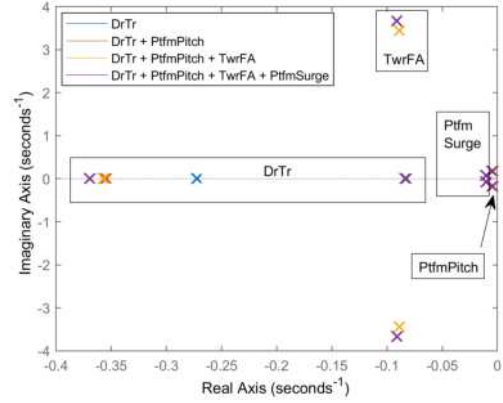


**Figure B.2:** Poles of the closed loop transfer function with different DOFs included ( $V_0 = 14$  m/s,  $k_p = 0.3$  s,  $T_i = 9$  s).

other DOFs do not have an obvious impact on the step response.

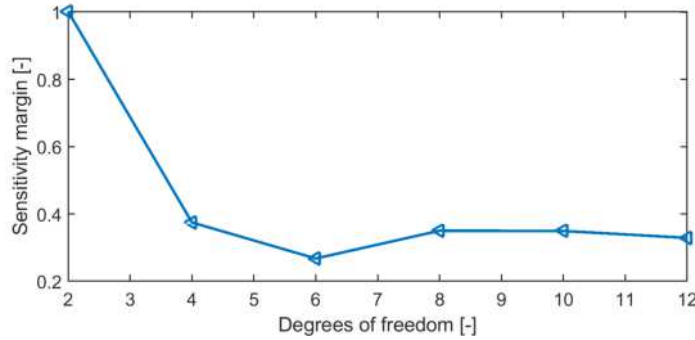


**Figure B.3:** Comparison of the sensitivity margin with different DOFs included ( $V_0 = 14$  m/s,  $k_p = 0.3$  s,  $T_i = 9$  s).

Although only two DOFs are of significant importance to shape the close loop behaviour of the FOWT, the robustness of stability shows different requirements, see figure B.3. The sensitivity margin of the open loop transfer function changes over included DOFs of the transfer function. The sensitivity margin becomes stable only after including four DOFs, i.e. drivetrain, platform pitch, platform surge, tower top fore-aft motion. Nevertheless, depending on the purpose of the control design, it is also possible to get reasonable result only using a model with two DOFs. The advantage is that the approach does not require a complex linear model, neither

the detailed system properties, which can be beneficial for data exchange within industrial partners. An example of building up a 2DOF model can be found in [64].

In summary of the analysis presented in this section, it is evident that a linear model with at least two DOFs is required to characterize the system's step response, meaning a minimum requirement for the transfer function is a fourth order. However, for a reliable stability analysis, at least four DOFs are needed.



# Bibliography

- [1] P. Fleming, I. Pineda, M. Rossetti, A. Wright, and D. Arora, “Evaluating methods for control of an offshore floating turbine,” *Proceedings of the ASME 33rd International Conference on Ocean, Offshore and Arctic Engineering*, 2014.
- [2] F. Lemmer, “Low-Order Modeling , Controller Design and Optimization of Floating Offshore Wind Turbines,” Ph.D. dissertation, University of Stuttgart, 2018.
- [3] C. Coudurier, O. Lepreux, and N. Petit, “Modelling of a tuned liquid multi-column damper. Application to floating wind turbine for improved robustness against wave incidence,” *Ocean Engineering*, vol. 165, pp. 277–292, 2018. [Online]. Available: <https://doi.org/10.1016/j.oceaneng.2018.03.033>
- [4] B. Siciliano and O. Khatib, *Springer handbook of robotics*, 2nd ed. Springer, 2016.
- [5] T. I. Fossen, *Handbook of Marine Craft Hydrodynamics and Motion Control*. John Wiley & Sons, Ltd, 2011.
- [6] R. R. CRAIG and M. C. C. BAMPTON, “Coupling of substructures for dynamic analyses.” *AIAA Journal*, vol. 6, no. 7, pp. 1313–1319, 1968. [Online]. Available: <https://doi.org/10.2514/3.4741>
- [7] R. Damiani, H. Song, A. Robertson, and J. Jonkman, “Assessing the importance of nonlinearities in the development of a substructure model for the wind turbine cae tool fast,” in *32nd International Conference on Ocean, Offshore and Arctic Engineering*, 06 2013.
- [8] J. F. Manwell, J. G. McGowan, and A. L. Rogers, *Wind Energy Explained: Theory, Design and Application*. John Wiley & Sons, Ltd, 2010.
- [9] T. Burton and D. Sharpe, *Wind energy handbook*. John Wiley & Sons, Ltd, 2011, vol. 49, no. 04.
- [10] D. Matha, S.-A. Fischer, S. Hauptmann, P. W. Cheng, D. Bekiropoulos,

- T. Lutz, T. Duarte, and K. Boorsma, "Variations in ultimate load predictions for floating offshore wind turbine extreme pitching motions applying different aerodynamic methodologies," ser. International Ocean and Polar Engineering Conference, 06 2013.
- [11] A. Suzuki and A. Hansen, "Generalized dynamic wake model for yawdyn," in *37th Aerospace Sciences Meeting and Exhibit*, pp. 186–191. [Online]. Available: <https://arc.aiaa.org/doi/abs/10.2514/6.1999-41>
- [12] J. Jonkman and W. Musial, "Offshore Code Comparison Collaboration (OC3) for IEA Task 23 Offshore Wind Technology and Deployment," NREL/TP-5000-48191, Tech. Rep., December 2010. [Online]. Available: <https://www.nrel.gov/docs/fy11osti/48191.pdf>
- [13] A. Cordle and J. Jonkman, "State of the art in floating wind turbine design tools," ser. International Ocean and Polar Engineering Conference, 06 2011. [Online]. Available: <https://www.nrel.gov/docs/fy12osti/50543.pdf>
- [14] L. Roald, J. Jonkman, A. Robertson, and N. Chokani, "The effect of second-order hydrodynamics on floating offshore wind turbines," *Energy Procedia*, vol. 35, pp. 253–264, 2013.
- [15] *Offshore Code Comparison Collaboration Continuation Within IEA Wind Task 30: Phase II Results Regarding a Floating Semisubmersible Wind System*, ser. International Conference on Offshore Mechanics and Arctic Engineering, vol. Volume 9B: Ocean Renewable Energy, 06 2014, v09BT09A012. [Online]. Available: <https://www.nrel.gov/docs/fy14osti/61154.pdf>
- [16] M. Y. Mahfouz, R. Faerron-Guzmán, K. Müller, F. Lemmer, and P. W. Cheng, "Validation of drift motions for a semi-submersible floating wind turbine and associated challenges," *Journal of Physics: Conference Series*, vol. 1669, no. 1, p. 012011, oct 2020. [Online]. Available: <https://dx.doi.org/10.1088/1742-6596/1669/1/012011>
- [17] J. Newman, "Second-Order, Slowly-Varying Forces on Vessels in Irregular Waves." in *Marine Vehicles*, 1974, pp. 182–186.
- [18] J. A. Pinkster, "Low frequency second order wave exciting forces on floating structures," p. 220, 1980.
- [19] J. M. Jonkman and M. L. Buhl, "FAST User's Guide," National Renewable Energy Laboratory (NREL), Golden, CO, USA, Tech. Rep., 2005. [Online].



- Available: <https://www.nrel.gov/docs/fy06osti/38230.pdf>
- [20] F. Lemmer, W. Yu, P. W. Cheng, A. Pegalajar-jurado, M. Borg, R. F. Mikkelsen, and H. Bredmose, “The TripleSpar campaign: validation of a reduced-order simulation model for floating wind turbines,” in *Proceedings of ASME 2018 37th International Conference on Ocean, Offshore and Arctic Engineering*, Madrid, Spain, 2018.
- [21] W. Yu, F. Lemmer, D. Schlipf, P. W. Cheng, B. Visser, H. Links, N. Gupta, S. Dankemann, B. Couñago, and J. Serna, “Evaluation of control methods for floating offshore wind turbines,” in *Journal of Physics: Conference Series*, vol. 1104, no. 1, 2018, p. 012033.
- [22] F. Lemmer, K. Müller, W. Yu, D. Schlipf, and P. W. Cheng, “Optimization of Floating Offshore Wind Turbine Platforms With a Self-Tuning Controller,” in *ASME 2017 36th International Conference on Ocean, Offshore and Arctic Engineering*, 2017, p. V010T09A080. [Online]. Available: <http://proceedings.asmedigitalcollection.asme.org/proceeding.aspx?doi=10.1115/OMAE2017-62038>
- [23] F. Lemmer, D. Schlipf, and P. W. Cheng, “Control design methods for floating wind turbines for optimal disturbance rejection,” *Journal of Physics: Conference Series*, vol. 573, no. 9, p. 092006, 2016. [Online]. Available: <http://stacks.iop.org/1742-6596/753/i=9/a=092006>
- [24] F. Lemmer, W. Yu, and P. W. Cheng, “Iterative frequency-domain response of floating wind turbines with parametric drag,” *Journal of Marine Science and Engineering*, vol. 6, no. 4, 2018. [Online]. Available: <http://www.mdpi.com/2077-1312/6/4/118>
- [25] H. Frahm, “Results of trials of the anti-rolling tanks at sea,” *Journal of the American Society for Naval Engineers*, vol. 23, no. 2, pp. 571–597, 1911. [Online]. Available: <https://onlinelibrary.wiley.com/doi/abs/10.1111/j.1559-3584.1911.tb04595.x>
- [26] R. Moaleji and A. R. Greig, “On the development of ship anti-roll tanks,” *Ocean Engineering*, vol. 34, no. 1, pp. 103–121, 2007.
- [27] C. Stigter, “The performance of U-tanks as a passive anti-rolling device,” *International Shipbuilding Progress*, vol. 13, no. 144, pp. 249–275, 1966.
- [28] A.R.J.M.Lloyd, *Seakeeping: Ship Behaviour in Rough Weather*. ARJMLloyd,

- 1998.
- [29] K. Shyu and H. Kuo, “Dynamic behaviour of a U-type tuned liquid damper,” in *International Shipbuilding Progress*, vol. 43, 1996, pp. 331–345.
- [30] C. Holden and T. I. Fossen, “A nonlinear 7-DOF model for U-tanks of arbitrary shape,” *Ocean Engineering*, vol. 45, pp. 22–37, 2012. [Online]. Available: <http://dx.doi.org/10.1016/j.oceaneng.2012.02.002>
- [31] A. F. Gawad, S. A. Ragab, A. H. Nayfeh, and D. T. Mook, “Roll stabilization by anti-roll passive tanks,” *Ocean Engineering*, vol. 28, no. 5, pp. 457–469, 2001.
- [32] S. Park, M. Glade, and M. Lackner, “Multi-objective optimization of orthogonal tlcds for reducing fatigue and extreme loads of a floating offshore wind turbine,” *Engineering Structures*, vol. 209, p. 110260, 04 2020.
- [33] Z. Zhong, M. Falzarano, and R. M. Fithen, “A Numerical Study of U-Tube Passive Anti-Rolling Tanks,” in *The Eighth International Offshore and Polar Engineering Conference*. Montreal, Canada: International Society of Offshore and Polar Engineers, 1998.
- [34] G. Popov, S. Sankar, and T. S. Sanker, “Dynamics of Liquid Sloshing in Horizontal Cylindrical Road Containers,” *Journal of Fluids Structure*, vol. 7, no. 7, pp. 803–821, 1993.
- [35] M. S. Celebi and H. Akyildiz, “Nonlinear modeling of liquid sloshing in a moving rectangular tank,” *Ocean Engineering*, vol. 29, no. 12, pp. 1527–1553, 2002.
- [36] W. Yu and P. W. Cheng, “Verification of a Passive Tuned Liquid Multi-Column Damper for Floating Wind Turbine,” in *The 30th International Ocean and Polar Engineering Conference*. International Society of Offshore and Polar Engineers, 2020.
- [37] S. Bennett, “Ship Stabilization: History,” in *Concise Encyclopedia of Traffic and Transportation Systems (Markos Papageorgiou, Ed.)*. New York: Pergamon Press, 1991, pp. 454–459.
- [38] M. Borg, E. U. Ortigado, M. Collu, and F. P. Brennan, “Passive damping systems for floating vertical axis wind turbines analysis,” in *EWEA2013*, 2013.
- [39] C. Coudurier, O. Lepreux, and N. Petit, “Passive and semi-active control of an offshore floating wind turbine using a tuned liquid column damper,” *IFAC-PapersOnLine*, vol. 48, no. 16, pp. 241–247, 2015. [Online]. Available: <http://dx.doi.org/10.1016/j.ifacol.2015.10.287>

- [40] W. Yu, F. Lemmer, and P. W. Cheng, "Performance of a passive tuned liquid column damper for floating wind turbines," in *Proceedings of the ASME 38th International Conference on Ocean, Offshore and Arctic Engineering*, 2019.
- [41] E. A. Bossanyi, "The Design of closed loop controllers for wind turbines," *Wind Energy*, vol. 3, no. 3, pp. 149–163, 2000. [Online]. Available: <http://doi.wiley.com/10.1002/we.34>
- [42] L. Pao and K. E. Johnson, "A tutorial on the dynamics and control of wind turbines and wind farms," in *2009 American Control Conference*, 2009, pp. 2076–2089. [Online]. Available: <http://ieeexplore.ieee.org/document/5160195/>
- [43] T. J. Larsen and T. D. Hanson, "A method to avoid negative damped low frequent tower vibrations for a floating, pitch controlled wind turbine," in *Journal of Physics: Conference Series*, vol. 75, 2007, p. 012073.
- [44] D. Schlipf, E. Simley, F. Lemmer, L. Pao, and P. W. Cheng, "Collective Pitch Feedforward Control of Floating Wind Turbines Using Lidar," *Journal of Ocean and Wind Energy*, vol. 2, no. 4, pp. 223–230, 2015. [Online]. Available: <http://www.isope.org/publications/jowe/jowe-02-4/joweNov15.htm>
- [45] B. Fischer, "Reducing rotor speed variations of floating wind turbines by compensation of non-minimum phase zeros," *IET Renewable Power Generation*, vol. 7, no. 4, pp. 413–419, 2013. [Online]. Available: <http://digital-library.theiet.org/content/journals/10.1049/iet-rpg.2012.0263>
- [46] H. Namik and K. A. Stol, "Control methods for Reducing Pitching Motions of Floating Wind Turbines," The University of Auckland, Auckland, New Zealand, Tech. Rep., 2009.
- [47] A. D. de Corcuera, A. Pujana-Arrese, J. M. Ezquerro, E. Seguro, and J. Landaluze, "H-infinity based control for load mitigation in wind turbines," *Energies*, vol. 5, no. 4, pp. 938–967, 2012.
- [48] S. Raach, D. Schlipf, F. Sandner, D. Matha, and P. W. Cheng, "Nonlinear Model Predictive Control of Floating Wind Turbines with Individual Pitch Control," *American Control Conference*, pp. 4434–4439, 2014.
- [49] H. Namik and K. Stol, "Individual blade pitch control of floating offshore wind turbines," *Wind Energy*, vol. 13, no. 1, pp. 74–85, 2010.
- [50] M. Garcia-Sanz, "Control co-design of floating offshore wind turbines," in *Presented at the 5th Wind Energy Systems Engineering Workshop, Pamplona*,

- Spain*, 10 2019. [Online]. Available: <https://www.nrel.gov/wind/assets/pdfs/systems-engineering-workshop-2019-control-co-design-offshore.pdf>
- [51] C. Bak, F. Zahle, R. Bitsche, A. Yde, L. C. Henriksen, A. Nata, and M. H. Hansen, “Description of the DTU 10 MW Reference Wind Turbine,” *DTU Wind Energy Report-I-0092*, no. July, pp. 1–138, 2013. [Online]. Available: <https://dtu-10mw-rwt.vindenergi.dtu.dk>
- [52] W. Yu, K. Müller, F. Lemmer, D. Schlipf, H. Bredmose, M. Borg, T. Landbø, and H. Andersen, “LIFES50+ Deliverable D4.2 Public Definition of the Two 10MW Floater Concepts,” University of Stuttgart, Tech. Rep., 2018. [Online]. Available: [https://lifes50plus.eu/wp-content/uploads/2018/04/GA\\_640741\\_LIFES50\\_D4.2.pdf](https://lifes50plus.eu/wp-content/uploads/2018/04/GA_640741_LIFES50_D4.2.pdf)
- [53] W. Yu, F. Lemmer, and P. W. Cheng, “Modeling and validation of a tuned liquid multi-column damper stabilized floating offshore wind turbine coupled system,” *Ocean Engineering*, vol. 280, p. 114442, 2023. [Online]. Available: <https://www.sciencedirect.com/science/article/pii/S0029801823008260>
- [54] B. U. Taskar, D. Dasgupta, V. Nagarajan, S. Chakraborty, A. Chatterjee, and O. P. Sha, “CFD aided modelling of anti-rolling tanks towards more accurate ship dynamics,” *Ocean Engineering*, vol. 92, pp. 296–303, 2014. [Online]. Available: <http://dx.doi.org/10.1016/j.oceaneng.2014.09.035>
- [55] C. Holden, T. Perez, and T. I. Fossen, “A Lagrangian approach to nonlinear modeling of anti-roll tanks,” *Ocean Engineering*, vol. 38, no. 2-3, pp. 341–359, 2011. [Online]. Available: <http://dx.doi.org/10.1016/j.oceaneng.2010.11.012>
- [56] W. Yu, P. W. Cheng, F. Lemmer, K. Lehmann, S. Guzman, J. Moreu, and T. Battistella, “Model test and validation of the CROWN floating offshore wind turbine,” in *Proceedings of the ASME 41st International Conference & on Ocean, Offshore Arctic Engineering OMAE 2022*, 2022.
- [57] M. Wigger, “Model validation of a tuned liquid multi-column damper for floating offshore wind turbines,” 2020, master thesis, University of Stuttgart.
- [58] S. de Guzmán, D. Marón, P. Bueno, M. Taboada, and M. Moreu, “A Reduced Draft Spar Concept for Large Offshore Wind Turbines,” ser. International Conference on Offshore Mechanics and Arctic Engineering, vol. Volume 10: Ocean Renewable Energy, 06 2018, v010T09A077. [Online]. Available: <https://doi.org/10.1115/OMAEE2018-77787>

- [59] O.M.Faltinsen, *Sea loads on ships and offshore structures*. Cambridge University Press, 1990.
- [60] B. J. Koo, M. H. Kim, and R. E. Randall, “Mathieu instability of a spar platform with mooring and risers,” *Ocean Engineering*, vol. 31, no. 17-18, pp. 2175–2208, 2004.
- [61] S. Nallayarasu and T. P. Mathai, “Effect of Mathieu instability on motion response of Spar hull with heave damping plate,” *Ships and Offshore Structures*, vol. 11, no. 8, pp. 833–846, 2016.
- [62] H. Mao and H. Yang, “Parametric pitch instability investigation of Deep Draft Semi-submersible platform in irregular waves,” *International Journal of Naval Architecture and Ocean Engineering*, vol. 8, no. 1, pp. 13–21, 2016. [Online]. Available: <http://dx.doi.org/10.1016/j.ijnaoe.2015.09.001>
- [63] W. Yu, F. Lemmer, D. Schlipf, and P. W. Cheng, “Loop shaping based robust control for floating offshore wind turbines,” *Journal of Physics: Conference Series*, vol. 1618, p. 022066, 2020.
- [64] J. Jonkman, “Influence of Control on the Pitch Damping of a Floating Wind Turbine,” in *46th AIAA Aerospace Sciences Meeting and Exhibit*, no. March, 2008. [Online]. Available: <http://arc.aiaa.org/doi/10.2514/6.2008-1306>
- [65] F. Lemmer (né Sandner), W. Yu, D. Schlipf, and P. W. Cheng, “Robust gain scheduling baseline controller for floating offshore wind turbines,” *Wind Energy*, 2019.
- [66] A. Krieger, G. K. V. Ramachandran, L. Vita, P. Gómez Alonso, J. Berque, and G. Aguirre-Suso, “LIFES50+ D7.2 Design basis,” DNVGL, Tech. Rep., 2015. [Online]. Available: [https://lifes50plus.eu/wp-content/uploads/2015/11/D72\\_Design\\_Basis\\_Retyped-v1.1.pdf](https://lifes50plus.eu/wp-content/uploads/2015/11/D72_Design_Basis_Retyped-v1.1.pdf)
- [67] F. Lemmer, F. Amann, S. Raach, and D. Schlipf, “Definition of the SWE-TripleSpar Floating Platform for the DTU 10MW Reference Wind Turbine,” University of Stuttgart, Stuttgart, Tech. Rep., 2016.
- [68] W. Yu, S. T. Zhou, F. Lemmer, and P. W. Cheng, “Control co-design optimization of floating offshore wind turbines with tuned liquid multi-column dampers,” *Wind Energy Science Discussions*, vol. 2023, pp. 1–25, 2023. [Online]. Available: <https://wes.copernicus.org/preprints/wes-2023-131/>
- [69] S. Zhou, C. Li, Y. Xiao, F. Lemmer, W. Yu, and P. W. Cheng, “IOWTC2019-

- 7553,” in *Proceedings of the ASME 2019 2nd International Offshore Wind Technical Conference*, 2019, pp. 1–10.
- [70] F. Lemmer, K. Müller, W. Yu, R. Faerron-Guzmán, and M. Kretschmer, “LIFES50+ Deliverable D4.3 Optimization framework and methodology for optimized floater design,” University of Stuttgart, Tech. Rep., 2017. [Online]. Available: [https://lifes50plus.eu/wp-content/uploads/2017/01/GA\\_640741\\_LIFES50\\_D4.3-web\\_Updated.pdf](https://lifes50plus.eu/wp-content/uploads/2017/01/GA_640741_LIFES50_D4.3-web_Updated.pdf)
- [71] S. Zhou, K. Müller, C. Li, Y. Xiao, and P. W. Cheng, “Global sensitivity study on the semisubmersible substructure of a floating wind turbine: Manufacturing cost, structural properties and hydrodynamics,” *Ocean Engineering*, vol. 221, p. 108585, 2021. [Online]. Available: <https://www.sciencedirect.com/science/article/pii/S0029801821000202>
- [72] K. Deb, A. Pratap, S. Agarwal, and T. Meyarivan, “A fast and elitist multiobjective genetic algorithm: NSGA-II,” *IEEE Transactions on Evolutionary Computation*, vol. 6, no. 2, pp. 182–197, 2002.
- [73] L. MartÁ, J. GarcÁa, A. Berlanga, and J. M. Molina, “A stopping criterion for multi-objective optimization evolutionary algorithms,” *Information Sciences*, vol. 367-368, pp. 700–718, 2016. [Online]. Available: <https://www.sciencedirect.com/science/article/pii/S0020025516305072>
- [74] R. Storn, “On the usage of differential evolution for function optimization,” in *Proceedings of North American Fuzzy Information Processing*, 1996, pp. 519–523.

# Curriculum Vitae

Wei (Viola) Yu was born on June 21st, 1988 in Zhejiang, China, and spent her childhood in a small town of Tongxiang until she completed her high school education.

She pursued her undergraduate studies in Naval Architecture and Ocean Engineering at Harbin Engineering University between 2007 and 2011, with a focus on fluid dynamics and structural mechanics. At the end of 2011, she moved to Germany to continue her studies, which started with learning German in Cologne. During this time, she developed a keen interest in renewable energy and subsequently shifted her focus to Energy Engineering for her master's degree between 2013 and 2016, specializing in wind energy and power grids. Her primary projects and internships were in the field of wind energy, including her internship at MesH Engineering GmbH and Fraunhofer IWES, as well as several student projects at Stuttgart Wind Energy (SWE). This led her to pursue a PhD in the same field.

Since the end of 2016, she has been working as a research associate at SWE. In this role, she supervised lectures and student theses, applied and managed projects, and conducted research work within various national and international projects. Her research mainly focused on floating offshore wind turbines, but also on floating lidar systems, including reduced-order modeling, integrated optimization, control design, and tuned liquid dampers. As a result of her research work, she has presented at about ten international conferences and workshops and has co-authored more than 20 publications.